Applications of 2DIR on Solution Dynamics and Reaction Chemistry

by

Robert W. McCanne

A dissertation submitted in partial fulfillment
of the requirements for the degree of
Doctor of Philosophy
(Chemistry)
in the University of Michigan
2011

Doctoral Committee:

Assistant Professor Kevin J. Kubarych, Chair
Professor Eitan Geva
Professor Roseanne J. Sension
Assistant Professor Jennifer P. Ogilvie

Table of Contents

List of Figures

List of Tables

Chapter 1

Introduction

1.1: Dynamics

1.1.1 Timescales and motions

Nearly all reaction chemistry occurs in solution.[1-6] Particulate interaction simply occurs much more readily and frequently in condensed phases as compared to the gas phase, and liquids in particular provide sufficient freedom of motion allowing diffusion and collision as compared to the rigidity of solids.[6] The solution itself also plays a stabilizing role for intermediates necessary for reactions to occur.[7] This makes the solution phase ideal for both the initial approach and eventual collision resulting in a chemical reaction.[5] Thus understanding solvation dynamics across a range of timescales is vital in understanding and controlling reactions and reactivity.[8] These microscopic interactions govern the energetics and the timescales of solution chemistry, and must be probed from both the solute and solvent perspective.[9]

The processes that underlie chemical and reaction dynamics include motional and energetic fluctuations of both the solvent and solute as the two components adjust to being in solution.[10,11] Equilibrium flucutations[1] lead to processes ranging from simple energy level fluctuations in both the solute and solvent on a sub-picosecond timescale, to more complicated equilibrium spectral diffusion and isomerization on a few picosecond timescale, to very complex non-equilibrium reactions propagation along a diverging energy coordinate on a hundreds of picoseconds timescale.[8] These fast motions then lead to complex reaction on

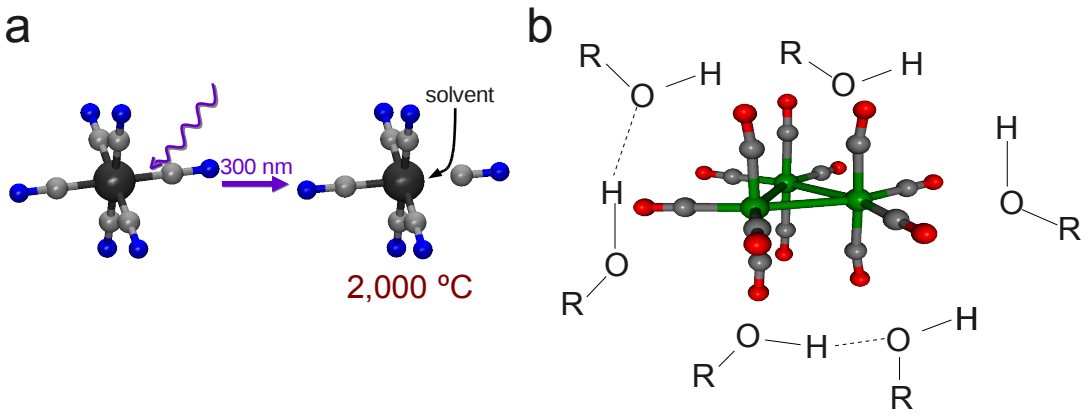

Figure 1: (a) Non-equilibrium, (b) equilibrium dynamics of solvated metal carbonyls.

microsecond to many second timescales.[12] We have considered some aspects of solvation and reaction dynamics by studying in detail metal carbonyl system $W(CO)_6$ and $Ru_3(CO)_{12}$ that allow tractable treatment both experimentally and using simple models. While important in catalytic and CO reaction chemistry, these systems also provide an important step towards fully characterizing complex ultrafast dynamics.[13,14]

1.1.2 Non-equilibrium motion

Energy harnessing and transport depends on a host of properties.[15-20] Not only does the equilibrium structure play an important role in the efficiency and speed of charge transfer, but in many energy applications propagation of the electron from absorption to conduction causes non-equilibrium distortions, resulting in stress to the well ordered solid structure.[21] Such distortions occur rapidly very locally but are dispersed temporally along the path traveled by the electron, requiring monitoring and analysis on a range of timescales.[22] These stresses are one of the primary factors in lithium-ion battery breakdown over repeated charge and discharge cycles.[23] A clear understanding of the intermolecular interactions, both electronic and vibrational, may lead to methods to better suppress such destructive motions.[23] This in turn would produce more stable long term energy capture and storage materials.[23]

The Born-Oppenheimer approximation is highly successful due to the large separation of masses between the electrons and the nuclei, and neatly divides chemical calculations into two regimes that can be computed dependently but separately.[24-26] Clearly, however, when non-equilibrium conditions are excited, as in a photoreaction, electronic changes will induce atomic motions due to the same separation.[27] In this way, the approximation can break down, and coupled vibronic states must be considered.[24,27] Though the analogy used here involves induced vibrational movements after a reaction, indeed any time two electronic states are separated by energies similar to the separation of vibrational energies, electronic and vibrational coordinates will mix and vibronic coupling becomes important.[24] Mixing was demonstrated experimentally as early as the 1930s with an excited π-state of CO_2.[28] Shortly thereafter calculations predicted the benzene spectrum and indicated the prevalence of vibronically mixed states.[29] Both understanding and exploiting the coupling of motions continues to be an active area of research.[30,31]

Often, rearrangements and reactions are driven along specific coordinates that couple strongly to faster timescale motions, in opposition to the electronically driven vibrations presented above.[30,32] In the case of azobenzene, two isomeric states exist, *cis* and *trans*, the reaction between which occurs via excitation with near-UV energy.[33] Previous work has focused on specific internal motions, such as the out of plane rocking motion of the benzene rings, and their relationship to this isomerization.[34] It has been suggested that sufficient vibrational energy deposited into this motion via the infrared could couple to the otherwise higher UV-energy isomerization transition, exciting the *trans* to *cis* movement vibrationally instead of electronically.[33] Experiments have hinted at this coupling, though it remains difficult to fully map on a multidimensional vibrational landscape.[34] Isomerization is often reduced to single coordinate "isomerization angle" where many degrees of freedom are collected into a single experimental parameter, here the out of plane rocking motion.[35] In contrast, other theories have suggested an in plane inversion occurs wherein one nitrogen undergoes an umbrella-like inversion in the symmetry plane.[36]

The energy landscape is not a simplified one dimensional with a single energy

barrier, but a multidimensional surface with many-dimensional hills.[37] Traversing the hill corresponds to excitation over the barrier to the product, but there are additional paths that instead skirt around the barrier, using the additional degrees of freedom to bypass traditional transition states.[37] These may be the paths taken in the absence of artificial excitation, relying instead on probabilistic absorption of available k_BT energy.[37] The in-plane inversion of azobenzene is one possible path that bypasses isomerization via twisting. Understanding vibronic coupling in larger systems require new methods of spectroscopy to fully monitor motions that occur during reaction, including a method of mapping reactants to products.[38]

1.1.3 Adapting to the ultrafast

Reactants evolve on ultrafast timescales, in the picosecond and even femtosecond regime, where initial electron redistribution drives nuclear motions.[25] While NMR has developed many tools and complex pulsing methods to access additional dynamics, it is nevertheless ultimately limited.[39] Because NMR uses radio frequencies the temporal resolution is limited to timescales on the order of the period, or around 1 ns.[5] Electromagnetic radiation cannot be used to effectively probe events smaller than a single cycle of the wavelength without encountering uncertainty limitations.[39] New techniques and shorter wavelengths are necessary to access faster dynamics.[40]

Infrared spectra report on the vibrational state of an ensemble of weakly coupled parts of an entire molecule, which can result in many groups of peaks.[41] Though this is rich in information content, it leads to congested areas where many vibrations, or even local inhomogeneities, cause peaks to overlap.[42] Visible spectra, on the other hand, probe the total electronic response of a system, often a single or few transitions between a limited set of electronic states.[43] These whole molecule responses can be difficult to map to nuclear movements, requiring calculation of the entire molecular electron density at any given time point.[44] Applying the multidimensional techniques adapted from NMR to the infrared allows the molecular response to be teased apart, providing sufficient resolution for analysis.[45]

1.2: Linear spectroscopy limitations

Because linear spectroscopy provides time averaged information, any processes faster than the scan length appear as averaged in the resulting spectra.[8] Peaks are broadened by multiple factors mixed together into a single observable: linewidth.[39] The lifetime of the states in question provides a starting point for linewidths, where the inverse of the lifetime gives the spectral width of an otherwise isolated transition.[8] In solution, however, the linewidth and lifetime are generally uncoupled.[43] In the infrared, narrow linewidths are achieved in cooled gas phase experiments, where the only additional consideration is Doppler broadening.[46] In solution this width is only approached in the most non-interacting of solvents.[43]

Particularly in the visible, overlapping transitions and broadened electronic linewidths make extracting dynamics difficult at best.[43] The extracted dynamics are also electronic in nature, not atomic, requiring modeling to characterize.[47] In contrast, infrared spectroscopy reports on molecular vibrations, which are extremely highly correlated with small geometry changes.[48] A bond 1 Å long will appreciably change frequency with only a 0.1 Å atomic movement.[8] In this way the infrared spectrum is inherently sensitive to positional information almost directly, though there remains the inevitable need to combine experiment with computation.[49]

In a linear spectrum in solution, sub-angstrom movements caused by sampling many microstates result in frequency fluctuations, producing broadening of the optical absorption line shape.[50] In some cases, this effect is small, as in isolated vibrations that do not couple to the bath, while in others the effect is much larger.[51] The OH stretch, for example, is broadened in many liquids over hundreds of wavenumbers, covering a large region around 3200 cm^{-1} and overlapping the entire CH stretching region near 3000 cm^{-1}.[52] Hydrogen bonding dynamics in general prove difficult to extract from linear spectra, as the energy involved is much greater than even other liquid dipoles.[53] Increased interaction energies between a solute and solvent mean further distortion from the isolated gas phase model for either.[54] This also increases the complexity when modeling

the system, as well.[55] Ultimately, the larger interaction between solute and solvent blurs

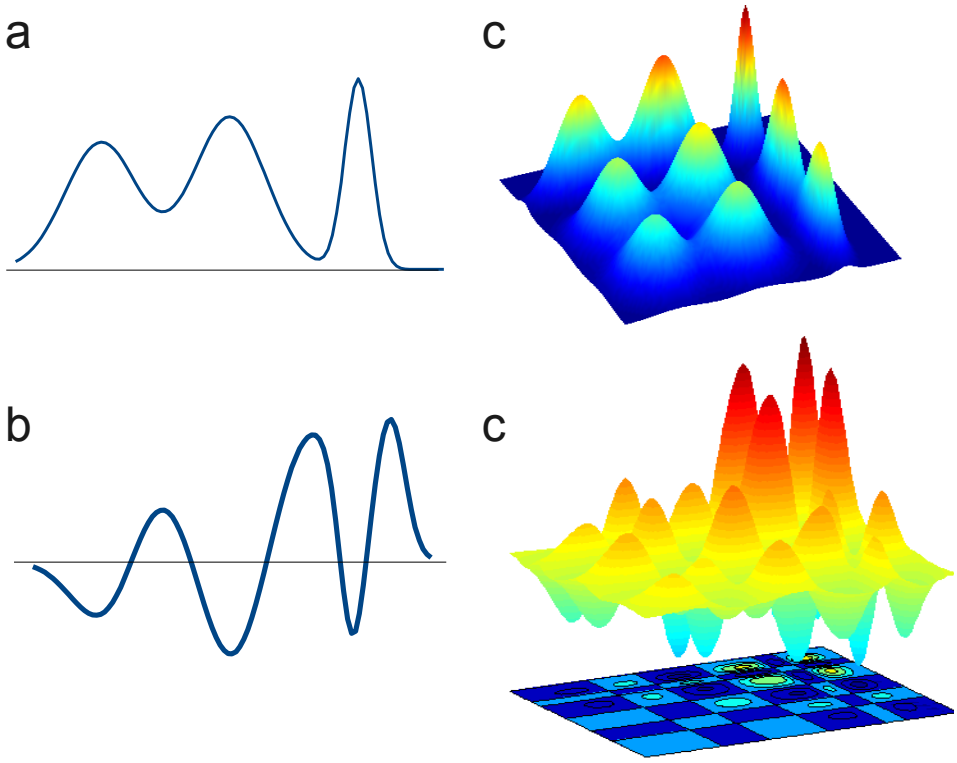

Figure 2: Progression from linear to transient multidimensional spectra. Linear spectra (a) three transitions are complicated by overlap of three transient features (b). In two dimensions (c), crosspeaks provide additional correlations and complications, which are further enhanced in 2D transient spectra (d).

the distinction between the system and surroundings.[56]

Note that in addition to inducing a large number of slightly altered local environments, highly interacting solvents may also change the overall lifetime of an excited state.[43] Thus there are two effects occurring simultaneously that prove difficult to disentangle. Indeed, in some sense the altered microscopic environment can be thought of as an alteration to the lifetime.[43] This inhomogeneity can be either static or dynamic, and in the latter case observation of the dynamic evolution of spectral inhomogeneity is tantamount to recording ultrafast snapshots of equilibrium solvation.

1.3: Non-linear spectroscopy

Though the frequency and time domain are in principle interchangeable by Fourier transformation, multiple dynamical processes hidden inside a single experimental observable such as linewidth makes sampling in the time domain preferable in some cases.[57] As such, it is necessary to define a starting point from which time dependent motions will be sampled to measure the molecular response in the time domain.[58] These non-linear experiments create a correlation map of molecular energies to elucidate fast solvation effects.[57]

1.3.1 Transient absorption spectroscopy

In transient absorption spectroscopy an initial field-matter interaction provides access to a non-equilibrium state from which evolves as a function of time. A second field-matter interaction then reports on the evolution at later times. This can be done using a pump and probe of many frequencies, including IR, UV/visible, and x-ray.[59-62] Visible pump, visible probe is employed to study ultrafast reactions through their electronic evolution.[36] Visible pump, IR probe is also used, providing a picture the vibrations following a photoreaction.[63] New advances in visible pump, x-ray probe have been reported, leading towards ultrafast transient x-ray experiments. X-ray probes produce atomic coordinates directly, but current x-ray pulse durations still lie in the hundred picosecond regime.[64] Much work has been done on creating shorter pulses for better time resolution and access to faster dynamics, and could one day give atomic coordinates with sub-femtosecond resolution.[65] Until then, ultrafast pulses in the visible and IR provide the best trade-off of atomic resolution for temporal resolution.

Given a pair of pump and probe pulses, the spectrum of a photoinduced process can be monitored with resolution dictated by the pulse temporal widths. The result is a series of spectra of the transient photoproducts as they evolve. Photoreactions can be chosen such that the transient evolution mirrors a natural process under study, such as excitation to an electronic state that lacks a barrier present in the ground electronic state,

leading to isomerization or dissociation following photolysis.[49] Probing persistent excited electronic states can be informative by mapping the energy potential landscape of a non-equilibrium potential well involved in energy transfer.[66] Vibrational excitation aids in illuminating the full vibrational potential well of a given electronic state.[67]

The same issues of congestion that obscure linear spectra are still present in transient spectra. Because transient spectra are the superposition of multiple species, often they are more congested than their linear counterparts.[68] Differences between spectra with and without excitation are often taken to highlight changes due solely to the photoexcitation. The result is a combination of both positive going (transient) peaks due to the formation of non-equilibrium species and negative going (bleach) peaks due to the loss of the equilibrium ground state species. Lineshapes are distorted by overlap with opposite sign features. In sufficiently resolved spectra characterizing transient peaks can be done by careful fitting to find peak centers and widths.[69] Additional peaks and broadening in a region can make the problem intractable.[68]

In addition, no information pertaining to the evolution through the transition state is contained in even the transient difference spectra.[38] Reactants with multiple peaks do not map directly onto corresponding product peaks; instead, product absorptions show only evolution following photoreaction.[70] Transitions states by their nature are unstable, sometimes occurring in and persisting for femtoseconds or less.[8] Probing occurs on a system already electronically perturbed from equilibrium in all but the slowest of transition state formations.[71]

1.3.2 Multidimensional spectroscopy

Building from work using NMR, multiple axes can be employed to exploit additional spectral resolution in the cases of congestion, revealing hidden dynamical information, probing the higher-order response of a system, and illuminating additional features of the molecular energy landscape.[45] Two-dimensional infrared (2DIR) and multidimensional infrared (MDIR) spectroscopy have emerged as an method of probing the nonlinear dynamics in solution on a picometer scale with sub-picosecond time

resolution.[43] Exploiting this resolution in multiple dimensions provides a sensitive method of probing many equilibrium solution dynamics, with extension to non-equilibrium processes as well.[43]

Frequency information, spread across two axis, provides a very sensitive probe of local solvation homogeneity, while time information along a third axis provides access to femtosecond and picosecond dynamics.[72] Additionally, while 2DIR probes all of these variables at equilibrium, non-equilibrium reactions can be studied by applying an additional light source and monitoring the resulting products using 2DIR.[73] This extends all of the advantages of 2DIR to both initial reactant dynamics and the resulting product formation dynamics.[74] This is of use in cases where one dimensional pump probe experiments produce overlapping features.[70] Modeling, a key tool in deconvolving congested linear spectra, is more difficult with evolving reacting species.[13] Addition of a second axis makes identifying such a case much easier.[73]

Finally, a truly unique type of non-equilibrium 2DIR experiment probes not just the reactant and product states with aforementioned sensitivity, but in fact connects these states over the reaction barrier.[73] Transition state chemistry is the heart of any reaction, and thus of singular importance in understanding reactions, solution phase or otherwise.[75] Because of the transient nature, however, the transition state is all but impossible to observe.[76] One dimensional transient spectroscopy produces a discrete before and after picture but only resolves the early product state.[41]

A 2DIR triggered exchange experiment initializes monitoring before the photoreaction, however, leading to correlation through the transition state.[38] It can be thought of as labeling the reactant with the initialization of a 2DIR experiment, then applying the photoexcitation, and finally reading out the final product state. Detection then correlates initial reactant frequency with detected product frequency. While still in the infant stage, this new spectroscopy will aid in understanding reactions in many ways. Work by Hamm et al. on the metal-to-ligand charge transfer (MLCT) in $[Re(CO)_3Cl(dmbpy)]$ (dmbpy = 4,4‘-dimethyl-2,2‘bipyridine) showed that, contrary to previous believed, the two CO vibrational modes of the product do not correlate directly to the two corresponding product modes.[38] Instead the CO modes switch frequency

ordering, with the low frequency reactant mode becoming the high frequency product mode, and vice versa. There is currently no other experimental method that provides this direct reactant to product frequency mapping. It is worth noting, however, that the technique used by Bredenbeck et al. lacks the very highest possible time resolution within the 2DIR probe due to their hybrid frequency-time domain approach. By employing a narrowband IR pump pulse, there is necessarily a loss of time resolution due to the requirement of separating the pump and probe pulses in time. This minimum time delay of between 500-1000 fs implies that rapid intramolecular vibrational redistribution can occur faster than the experiment and will diminish the ability to map product transitions to those on the reactant. Indeed, recent unpublished work in our group on the same Re complex indicates that IVR among all three vibrational modes is very rapid (<2ps), suggesting that the hybrid double-resonance-like method of Bredenbeck et al. is not well suited for such rapid reactant vibrational dynamics. In this thesis work is described that circumvents the technical limitations by demonstrating, for the first time, electronically triggered, transient Fourier-transform 2DIR spectroscopy.

References

1. Anna, J.M., Ross, M.R. & Kubarych, K.J. Dissecting Enthalpic and Entropic Barriers to Ultrafast Equilibrium Isomerization of a Flexible Molecule Using 2DIR Chemical Exchange Spectroscopy. *The Journal of Physical Chemistry A* **113**, 6544-6547 (2009).
2. Beard, M.C., Turner, G.M. & Schmuttenmaer, C.A. Measuring intramolecular charge transfer via coherent generation of THz radiation. *Journal of Physical Chemistry A* **106**, 878-883 (2002).
3. Firman, P., Xu, M., Eyring, E.M. & Petrucci, S. Thermodynamics of Dimerization of Nascn in Some Acyclic Polyethers Studied by Infrared-Spectroscopy. *Journal of Physical Chemistry* **96**, 8631-8639 (1992).
4. Fonseca, T., Kim, H.J. & Hynes, J.T. Twisted Intramolecular Charge-Transfer Dynamics in Polar-Solvents. *Journal of Photochemistry and Photobiology a-Chemistry* **82**, 67-79 (1994).
5. Hamm, P., Helbing, J. & Bredenbeck, J. Two-dimensional infrared spectroscopy of photoswitchable peptides. *ANNUAL REVIEW OF PHYSICAL CHEMISTRY* **59**, 291-317 (2008).
6. Owrutsky, J.C., Raftery, D. & Hochstrasser, R.M. Vibrational relaxation dynamics in solutions. *Annu Rev Phys Chem* **45**, 519-55 (1994).
7. Lehr, L., Zanni, M.T., Frischkorn, C., Weinkauf, R. & Neumark, D.M. Electron solvation in finite systems: femtosecond dynamics of iodide. (Water)n anion clusters. *Science* **284**, 635-8 (1999).
8. Zewail, A. Femtochemistry: Atomic-scale dynamics of the chemical bond. *JOURNAL OF PHYSICAL CHEMISTRY A* **104**, 5660-5694 (2000).
9. Baiz, C.R. & Kubarych, K.J. Ultrafast Vibrational Stark-Effect Spectroscopy: Exploring Charge-Transfer Reactions by Directly Monitoring the Solvation Shell Response. *Journal of the American Chemical Society* **132**, 12784-12785 (2010).
10. Moore, J.N., Hansen, P.A. & Hochstrasser, R.M. Iron-carbonyl bond geometries of carboxymyoglobin and carboxyhemoglobin in solution determined by picosecond time-resolved infrared spectroscopy. *Proc Natl Acad Sci U S A* **85**, 5062-6 (1988).
11. Janes, S.M., Holtom, G., Ascenzi, P., Brunori, M. & Hochstrasser, R.M. Fluorescence and energy transfer of tryptophans in Aplysia myoglobin. *Biophysical Journal* **51**, 653-60 (1987).
12. Kobayashi, T., Saito, T. & Ohtani, H. Real-time spectroscopy of transition states in bacteriorhodopsin during retinal isomerization. *Nature* **414**, 531-534 (2001).
13. Baiz, C.R., McRobbie, P.L., Anna, J.M., Geva, E. & Kubarych, K.J. Two-Dimensional Infrared Spectroscopy of Metal Carbonyls. *Accounts of Chemical Research* **42**, 1395-1404 (2009).
14. Baiz, C.R., McCanne, R. & Kubarych, K.J. Structurally selective geminate rebinding dynamics of solvent-caged radicals studied with nonequilibrium infrared echo spectroscopy. *J Am Chem Soc* **131**, 13590-1 (2009).
15. Abramavicius, D. & Mukamel, S. Quantum oscillatory exciton migration in photosynthetic reaction centers. *Journal of Chemical Physics* **133**, 9 (2010).
16. Engel, G.S. et al. Evidence for wavelike energy transfer through quantum coherence in photosynthetic systems. *Nature* **446**, 782-786 (2007).
17. Moog, R.S., Kuki, A., Fayer, M.D. & Boxer, S.G. Excitation transport and trapping in a synthetic chlorophyllide substituted hemoglobin: orientation of the chlorophyll S1 transition dipole. *Biochemistry* **23**, 1564-71 (1984).
18. Woutersen, S. & Bakker, H.J. Resonant intermolecular transfer of vibrational energy in liquid water. *NATURE* **402**, 507-509 (1999).
19. Myers, J.A. et al. Two-Dimensional Electronic Spectroscopy of the D1-D2-cyt b559

Photosystem II Reaction Center Complex. *The Journal of Physical Chemistry Letters* **1**, 2774-2780 (2010).
20. Read, E.L. et al. Visualization of Excitonic Structure in the Fenna-Matthews-Olson Photosynthetic Complex by Polarization-Dependent Two-Dimensional Electronic Spectroscopy. *Biophysical Journal* **95**, 847-856 (2008).
21. Liang, Z., Nardes, A., Wang, D., Berry, J. & Gregg, B. Defect Engineering in pi-Conjugated Polymers. *CHEMISTRY OF MATERIALS* **21**, 4914-4919 (2009).
22. Liu, J. et al. Oriented Nanostructures for Energy Conversion and Storage. *CHEMSUSCHEM* **1**, 676-697 (2008).
23. Huang, J. et al. In Situ Observation of the Electrochemical Lithiation of a Single SnO2 Nanowire Electrode. *SCIENCE* **330**, 1515-1520 (2010).
24. BURLAND, D. & ROBINSON, G. IS BREAKDOWN OF BORN-OPPENHEIMER APPROXIMATION RESPONSIBLE FOR INTERNAL CONVERSION IN LARGE MOLECULES. *PROCEEDINGS OF THE NATIONAL ACADEMY OF SCIENCES OF THE UNITED STATES OF* **66**, 257-& (1970).
25. Lin, S.H. & Eyring, H. Study of Vibronic and Born-Oppenheimer Couplings. *Proceedings of the National Academy of Sciences of the United States of America* **71**, 3415 -3417 (1974).
26. BLUDMAN, S. & DAITCH, P. VALIDITY OF THE BORN-OPPENHEIMER APPROXIMATION. *PHYSICAL REVIEW* **95**, 823-830 (1954).
27. SUCRE, M., GENY, F. & LEFEBVRE, R. INTENSITY PATTERNS IN ABSORPTION AND FLUORESCENCE SPECTRA OF MOLECULAR DIMERS - A COMPARISON BETWEEN VIBRONIC AND BORN-OPPENHEIMER APPROACH. *JOURNAL OF CHEMICAL PHYSICS* **49**, 458-& (1968).
28. Hettema, H. *Quantum chemistry: classic scientific papers*. (World Scientific: 2000).
29. Goeppert-Mayer, M. & Sklar, A. Calculations of the lower excited levels of benzene. *JOURNAL OF CHEMICAL PHYSICS* **6**, 645-652 (1938).
30. Florean, A., Cardoza, D., White, J., Sension, R. & Bucksbaum, P. Coherent Control of Retinal Isomerization in Bacteriorhodopsin in the High Intensity Regime. *ULTRAFAST PHENOMENA XVI* **92**, 430-432 (2009).
31. Tsubouchi, M., Khramov, A. & Momose, T. Rovibrational wave-packet manipulation using shaped midinfrared femtosecond pulses. *Physical Review A* **77**, - (2008).
32. Hauer, J., Buckup, T., Voll, J., de Vivie-Riedle, R. & Motzkus, M. Coherent control of matter waves passing through a conical intersection in beta-carotene. *ULTRAFAST PHENOMENA XVI* **92**, 436-438 (2009).
33. Zhang, C. et al. Coherent electron transport through an azobenzene molecule: A light-driven molecular switch. *PHYSICAL REVIEW LETTERS* **92**, (2004).
34. Hamm, P., Ohline, S.M. & Zinth, W. Vibrational cooling after ultrafast photoisomerization of azobenzene measured by femtosecond infrared spectroscopy. *Journal of Chemical Physics* **106**, 519-529 (1997).
35. Fujino, T. & Tahara, T. Picosecond time-resolved Raman study of trans-azobenzene. *Journal of Physical Chemistry A* **104**, 4203-4210 (2000).
36. Bandara, H. et al. Proof for the Concerted Inversion Mechanism in the trans(->)cis Isomerization of Azobenzene Using Hydrogen Bonding To Induce Isomer Locking. *JOURNAL OF ORGANIC CHEMISTRY* **75**, 4817-4827 (2010).
37. Frauenfelder, H., Sligar, S.G. & Wolynes, P.G. The energy landscapes and motions of proteins. *Science* **254**, 1598-603 (1991).
38. Bredenbeck, J., Helbing, J. & Hamm, P. Labeling vibrations by light: Ultrafast transient 2D-IR spectroscopy tracks vibrational modes during photoinduced charge transfer. *Journal of the American Chemical Society* **126**, 990-991 (2004).

39. Tokmakoff, A. Two-dimensional line shapes derived from coherent third-order nonlinear spectroscopy. *Journal of Physical Chemistry A* **104**, 4247-4255 (2000).
40. Zanni, M.T. & Hochstrasser, R.M. Two-dimensional infrared spectroscopy: a promising new method for the time resolution of structures. *Curr Opin Struct Biol* **11**, 516-22 (2001).
41. Banno, M., Ohta, K., Yamaguchi, S., Hirai, S. & Tominaga, K. Vibrational Dynamics of Hydrogen-Bonded Complexes in Solutions Studied with Ultrafast Infrared Pump−Probe Spectroscopy. *Accounts of Chemical Research* **42**, 1259-1269 (2009).
42. Glascoe, E., Kling, M., Shanoski, J. & Harris, C. Nature and role of bridged carbonyl intermediates in the ultrafast photoinduced rearrangement of Ru-3(CO)(12). *ORGANOMETALLICS* **25**, 775-784 (2006).
43. Ogilvie, J.P. & Kubarych, K.J. Chapter 5 Multidimensional Electronic and Vibrational Spectroscopy: An Ultrafast Probe of Molecular Relaxation and Reaction Dynamics. *Advances In Atomic, Molecular, and Optical Physics* **57**, 249-321 (2009).
44. Demirdoven, N., Khalil, M., Golonzka, O. & Tokmakoff, A. Correlation effects in the two-dimensional vibrational spectroscopy of coupled vibrations. *Journal of Physical Chemistry A* **105**, 8025-8030 (2001).
45. Zanni, M.T. & Hochstrasser, R.M. Two-dimensional infrared spectroscopy: a promising new method for the time resolution of structures. *Curr Opin Struct Biol* **11**, 516-22 (2001).
46. STONER, J. & LEAVITT, J. REDUCTION OF DOPPLER BROADENING OF SPECTRAL LINES IN FAST-BEAM SPECTROSCOPY. *APPLIED PHYSICS LETTERS* **18**, 477-& (1971).
47. Milota, F., Sperling, J., Nemeth, A., Mančal, T. & Kauffmann, H.F. Two-Dimensional Electronic Spectroscopy of Molecular Excitons. *Accounts of Chemical Research* **42**, 1364-1374 (2009).
48. Roberts, S.T., Ramasesha, K. & Tokmakoff, A. Structural Rearrangements in Water Viewed Through Two-Dimensional Infrared Spectroscopy. *Accounts of Chemical Research* **42**, 1239-1249 (2009).
49. Smith, A.W. & Tokmakoff, A. Probing Local Structural Events in beta-Hairpin Unfolding with Transient Nonlinear Infrared Spectroscopy. *Angewandte Chemie International Edition* **46**, 7984-7987 (2007).
50. Roberts, S.T., Loparo, J.J. & Tokmakoff, A. Characterization of spectral diffusion from two-dimensional line shapes. *Journal of Chemical Physics* **125**, - (2006).
51. Kwak, K., Zheng, J.R., Cang, H. & Fayer, M.D. Ultrafast two-dimensional infrared vibrational echo chemical exchange experiments and theory. *Journal of Physical Chemistry B* **110**, 19998-20013 (2006).
52. Tokmakoff, A. Shining light on the rapidly evolving structure of water. *Science* **317**, 54-55 (2007).
53. Elsaesser, T. Two-Dimensional Infrared Spectroscopy of Intermolecular Hydrogen Bonds in the Condensed Phase. *Accounts of Chemical Research* **42**, 1220-1228 (2009).
54. Bour, P. & Keiderling, T.A. Empirical modeling of the peptide amide I band IR intensity in water solution. *Journal of Chemical Physics* **119**, 11253-11262 (2003).
55. Schmidt, J.R. et al. Are water simulation models consistent with steady-state and ultrafast vibrational spectroscopy experiments? *Chemical Physics* **341**, 143-157 (2007).
56. McCanne, R., King, J.T., Baiz, C.R. & Kubarych, K.J. Vibrational Energy Transfer and Spectral Diffusion Dynamics in a Vibrational Aggregate with Disorder-Induced Delocalization. *Forthcoming* (2011).
57. Mukamel, S. *Principles of nonlinear optical spectroscopy*. (Oxford University Press: New York, 1995).
58. Kim, Y.S. & Hochstrasser, R.M. Comparison of linear and 2D IR spectra in the presence of

fast exchange. *Journal of Physical Chemistry B* **110**, 8531-4 (2006).
59. Greene, B.I., Hochstrasser, R.M., Weisman, R.B. & Eaton, W.A. Spectroscopic studies of oxy- and carbonmonoxyhemoglobin after pulsed optical excitation. *Proc Natl Acad Sci U S A* **75**, 5255-9 (1978).
60. Dougherty, T. & Heilweil, E. Ultrafast transient infrared absorption studies of M(CO)6 (M = Cr, Mo or W) photoproducts in n-hexane solution. *Chemical Physics Letters* **227**, 19-25 (1994).
61. Janes, S.M., Dalickas, G.A., Eaton, W.A. & Hochstrasser, R.M. Picosecond transient absorption study of photodissociated carboxy hemoglobin and myoglobin. *Biophysical Journal* **54**, 545-9 (1988).
62. Kovalenko, S.A., Eilers-Konig, N., Senyushkina, T.A. & Ernsting, N.P. Charge transfer and solvation of betaine-30 in polar solvents - A femtosecond broadband transient absorption study. *Journal of Physical Chemistry A* **105**, 4834-4843 (2001).
63. Rini, M., Kummrow, A., Dreyer, J., Nibbering, E.T.J. & Elsaesser, T. Femtosecond mid-infrared spectroscopy of condensed phase hydrogen-bonded systems as a probe of structural dynamics. *Faraday Discussions* **122**, 27-40 (2003).
64. Kong, Q. et al. Ultrafast X-ray Solution Scattering Reveals Different Reaction Pathways in the Photolysis of Triruthenium Dodecacarbonyl (Ru-3(CO)(12)) after Ultraviolet and Visible Excitation. *JOURNAL OF THE AMERICAN CHEMICAL SOCIETY* **132**, 2600-2607 (2010).
65. Regier, T., Vogt, J., Sammynaiken, R. & Sham, T. Advances in Time Resolved X-ray Excited Optical Luminescence Instrumentation at the Canadian Light Source. *SRI 2009: THE 10TH INTERNATIONAL CONFERENCE ON SYNCHROTRON RADIATION* **1234**, 838-841 (2010).
66. Stone, K.W., Turner, D.B., Gundogdu, K., Cundiff, S.T. & Nelson, K.A. Exciton−Exciton Correlations Revealed by Two-Quantum, Two-Dimensional Fourier Transform Optical Spectroscopy. *Accounts of Chemical Research* **42**, 1452-1461 (2009).
67. Tokmakoff, A., Kwok, A.S., Urdahl, R.S., Francis, R.S. & Fayer, M.D. Multilevel Vibrational Dephasing and Vibrational Anharmonicity from Infrared Photon-Echo Beats. *Chemical Physics Letters* **234**, 289-295 (1995).
68. Owrutsky, J.C. & Baronavski, A.P. Ultrafast infrared study of the ultraviolet photodissociation of Mn2(CO)10. *J. Chem. Phys.* **105**, 9864 (1996).
69. Baiz, C.R., McCanne, R., Nee, M.J. & Kubarych, K.J. Orientational Dynamics of Transient Molecules Measured by Nonequilibrium Two-Dimensional Infrared Spectroscopy. *The Journal of Physical Chemistry A* **113**, 8907-8916 (2009).
70. Baiz, C.R., Nee, M.J., McCanne, R. & Kubarych, K.J. Ultrafast nonequilibrium Fourier-transform two-dimensional infrared spectroscopy. *Opt. Lett.* **33**, 2533-2535 (2008).
71. Ginsberg, N.S., Cheng, Y.C. & Fleming, G.R. Two-Dimensional Electronic Spectroscopy of Molecular Aggregates. *Accounts of Chemical Research* **42**, 1352-1363 (2009).
72. Demirdoven, N., Khalil, M. & Tokmakoff, A. Correlated vibrational dynamics revealed by two-dimensional infrared spectroscopy. *Phys Rev Lett* **89**, 237401 (2002).
73. Bredenbeck, J., Helbing, J., Kolano, C. & Hamm, P. Ultrafast 2D-IR Spectroscopy of transient species. *Chemphyschem* **8**, 1747-1756 (2007).
74. Bredenbeck, J. et al. Transient 2D-IR spectroscopy: Snapshots of the nonequilibrium ensemble during the picosecond conformational transition of a small peptide. *Journal of Physical Chemistry B* **107**, 8654-8660 (2003).
75. Chung, H.S., Shandiz, A., Sosnick, T.R. & Tokmakoff, A. Probing the folding transition state of ubiquitin mutants by temperature-jump-induced downhill unfolding. *Biochemistry* **47**, 13870-7 (2008).
76. Rubtsov, I.V., Redmore, N.P., Hochstrasser, R.M. & Therien, M.J. Interrogating

conformationally dependent electron-transfer dynamics via ultrafast visible pump/IR probe spectroscopy. *J Am Chem Soc* **126**, 2684-5 (2004).

Chapter 2

Theoretical Framework and Background

2.1: The Optical Response Function

2.1.1 General optical response

Spectroscopy is governed by the response of matter to interaction with an applied light field. The molecular property that couples with the applied electric field is the polarization P, which can be written as the expansion

$$P=P^{(1)}+P^{(2)}+P^{(3)}+\ldots+P^{(n)} \quad (1)$$

where $P^{(n)}$ is the material interaction with the nth power of the electric field.[1] This first order response $P^{(1)}$ is the linear material response, probed by low applied power fields. The collection of $P^{(2)}$ and greater is collectively referred to as the non-linear response, scaling non-linearly with applied field strength. Though in principle all orders are present for every experiment, in practice specific orders can be isolated by application of proper selection criteria. Very low power fields almost exclusively probe the linear response, with additional terms being negligible in most cases. Non-linear signals can be isolated using phase matching and energy conservation rules, though linear scattering is always a concern. All molecular processes that are probed by optical spectroscopy are determined by their polarization response, making this the key quantity to compute.

The principal concern for non-linear interactions will be dealing with the time ordering of the individual interactions, n for an nth order process. The frequency domain response contains all possible permutations of these time orderings, which indicates that a

complete response in the time domain can only be found by integrating multiple time domain response orderings. To begin with, the material will be treated quantum mechanically, while the optical field will be treated as a classical wave. This adequately captures the many-photon interaction picture and greatly simplifies the calculations. Secondly, the system will be treated in the perturbative limit, where applied electric fields, even strongly interacting ones at higher orders, are small in comparison to the internal electric fields of the system. Though interesting behavior can be observed in the non-perturbative limit, including the so called "dressed state" of a combined field and matter, a full discussion of these effects is beyond the scope of this work.

Following the derivation in Mukamel's *Principles of Nonlinear Spectroscopy*, the field-matter interaction Hamiltonian in the semi-classical picture is given by

$$H_{int} = -\int E(r,t) \cdot P(r) \cdot dr \tag{2}$$

for material polarization density P(**r**) and applied classical transverse electric field E(**r**,t). This holds for the interaction of any particle and light field. Generally individual particles will be much smaller than the applied light field for optical spectroscopies. The matter can then be approximated as a point dipole with respect to the applied field. Considering a single particle at **r** the time dependent interaction Hamiltonian is then given by

$$H_{int}(t) = -E(r,t) \cdot V \tag{3}$$

with the dipole operator V expressed as

$$V = \sum_n q_n (r - r_n) \tag{4}$$

for the collection of all charges n with charge q_n and position $\mathbf{r}_n$. Note that both E and V are vectors, making the response functions derived from them tensors. This provides for the calculation of an orientational response in anisotropic media, such as the crystals used for parametric frequency conversion in generating infrared light from a visible laser. The tensor nature will not be indicated, but assumed.

The optical polarization must begin from an initial equilibrium at $t = t_0$. This is given by

$$\rho(t_0)=\rho(-\infty)=\frac{e^{\left(\frac{-H}{k_B T}\right)}}{Tr\left[e^{\frac{-H}{k_B T}}\right]} \tag{5}$$

with Boltzmann constant k_B and temperature T. The observable of a system is given by the expectation value applied to the operator, denoted by angular brackets $\langle\rangle$. This is computed by taking the trace of the matrix state, resulting in a set of eigenvalues, here applied to the exponentiated Hamiltonian. The state of the system is described by the density matrix ρ, which contains diagonal populations and off-diagonal coherences. The total Hamiltonian can be written as $H_T = H + H_{int}(t)$ with a time independent and dependent term. The dynamics can be described by applying the Liouville equation

$$\frac{d\rho}{dt}=-\frac{i}{\hbar}\left([H,\rho]+\left[H_{int}(t),\rho\right]\right) \tag{6}$$

computing the commutation of each Hamiltonian with the density matrix.

The time-dependent density matrix can be expanded in electric field powers to yield

$$\rho(t)=\rho^{(0)}+\rho^{(1)}(t)+\rho^{(2)}(t)+\rho^{(3)}(t)+\ldots \tag{7}$$

for nth order interaction with the electric field. Here $\rho^{(0)} = \rho(-\infty)$ is the time independent equilibrium density matrix, exactly equal at any time before t_0. For simplicity, the Liouville notation can be used, converting commutation operations on an ordinary operator A into "super" operators in the following way:

$$LA=[H,A], \tag{8a}$$

$$L_{int}(t)A=\left[H_{int}(t),A\right]. \tag{2.8b}$$

The nth order interaction density matrix is then given by

$$\begin{aligned}\rho^{(n)}(t)=&\left(-\frac{i}{\hbar}\right)^n\int_{t_0}^{t}d\tau_n\int_{t_0}^{\tau_n}d\tau_{n-1}\cdots\int_{t_0}^{\tau_2}d\tau_1\ldots\\ &G(t-\tau_n)L_{int}(\tau_n)G(\tau_n-\tau_{n-1})L_{int}(\tau_{n-1})\cdots G(\tau_2-\tau_1)L_{int}(\tau_1)G(\tau_1-t_0)\rho(t_0)\end{aligned} \tag{9}$$

with time ordered τ such that $t\geq\tau_n\geq\tau_{n-1}\geq\cdots\geq\tau_1\geq t_0$ and

$$G(\tau)=\theta(t)e^{\left(-\frac{i}{\hbar}L\tau\right)} \tag{10}$$

the material propagation in the absence of light. The introduction of θ(t) is simply a Heavyside function equal to one at times greater than t_0 and zero at earlier times to enforce causality and ensure evolution only after the initial field interaction.

The initial density matrix does not evolve with time, so applying the material Hamiltonian to the time zero density matrix gives simply the initial density matrix again. Furthermore, $L_{int}(t) = -E(t)V$, where V is the Liouville operator of the commutation [V,A]. Together with (9) this gives

$$\begin{aligned}\rho^{(n)}(t)=\left(\frac{i}{\hbar}\right)^n\int_{t_0}^{t}d\tau_n\int_{t_0}^{\tau_n}d\tau_{n-1}\cdots\int_{t_0}^{\tau_2}d\tau_1 E(r,\tau_n)E(r,\tau_{n-1})\cdots E(r,\tau_1)\cdots\\ G(t-\tau_n)VG(\tau_n-\tau_{n-1})V\cdots G(\tau_2-\tau_1)V\rho(t_0).\end{aligned} \tag{11}$$

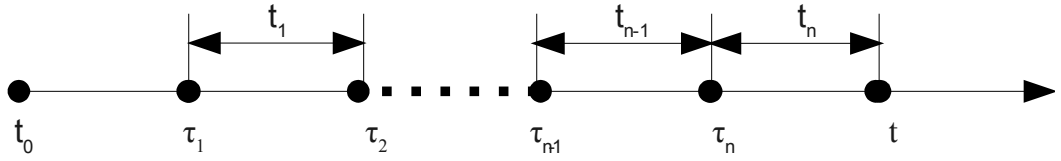

Figure 3: Time ordering of light-matter field interactions field-free evolution. The density matrix is calculated for each light-matter interaction at each τ while the system evolves via the intrinsic Green function during the each interval t.

Lastly, the time variables are simplified by redefinition as intervals

$t_1=\tau_2-\tau_1,\ t_2=\tau_3-\tau_2,\ \cdots,\ t_n=t-\tau_n.$ The density matrix is time independent and does not evolve before interaction with the field at t_0, making t_0 equivalent to $t = -\infty$, and giving

$$\begin{aligned}\rho^{(n)}(t)=\left(\frac{i}{\hbar}\right)^n\int_{0}^{\infty}dt_n\int_{0}^{\infty}dt_{n-1}\cdots\int_{0}^{\infty}dt_1 G(t_n)VG(t_{n-1})V\cdots G(t_1)V\rho(-\infty)\times\ldots\\ E(r,t-t_n)E(r,t-t_n-t_{n-1})\cdots E(r,t-t_n-t_{n-1}\cdots-t_1).\end{aligned} \tag{12}$$

The time dependent-polarization is the expectation of the dipole moment operator V, such that

$$P(r,t)=Tr[V\rho(t)] \tag{13}$$

and can be expanded in a Taylor series to nth order as in (1), such that the polarization of

given order in electric field is given by

$$P^{(n)}(r,t)=Tr\left[V\rho^{(n)}(t)\right]. \tag{14}$$

Each order of P represent a class of experiments dependent on n interactions with the electric field. $P^{(1)}$ is the linear absorption process, $P^{(2)}$ is the second order non-linear process used in sum frequency generation and second harmonic generation, and $P^{(3)}$ is the third order polarization used in four-wave mixing (FWM) and 2DIR spectroscopy, as well as pump-probe spectroscopy in general. Finally, using the expansion of ρ(t) in equation (14), the nth order polarization is given by

$$\begin{aligned} P^{(n)}(r,t)=&\int_0^\infty dt_n\int_0^\infty dt_{n-1}\cdots\int_0^\infty dt_1 S^{(n)}(t_n,t_{n-1},\ldots,t_1)\cdots \\ &E(r,t-t_n)E(r,t-t_n-t_{n-1})\cdots E(r,t-t_n-t_{n-1}-\cdots-t_1), \end{aligned} \tag{15}$$

with

$$S^{(n)}(t_n,t_{n-1},\ldots,t_1)=\left(\frac{i}{\hbar}\right)^n Tr\left[VG(t_n)VG(t_{n-1})V\cdots G(t_1)V\rho(-\infty)\right]. \tag{16}$$

$S^{(n)}$ is the linear response function for order n = 1 and the non-linear response function of the nth order in electric field, and is the complete set of molecular information for n field interactions. Furthermore, because $P^{(n)}$ is observable, it is necessarily real. The same is true for the electric field E. Thus the response functions $S^{(n)}$ must also be real. Additionally, $S^{(n)}$ are causal, as each polarization proceeds from a preceding electric field interaction. Equations (15) and (16) together allow the experimentally observable polarization to be calculated from a given molecular response.

2.1.2 Linear spectroscopy

The response function $S^{(n)}$ contains n operations of the Liouville dipole operator V. Each operation is an application of a commutation, which can act from either the left or the right of he density matrix, equivalent to acting on the bra or the ket of the system. Thus, each interaction with the field produces 2^n terms in the response function. In general, this will result in 2^{n-1} terms

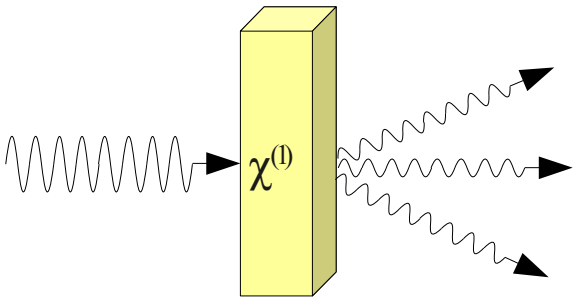

Figure 4: Material linear interaction with an applied light field. Incoming light is attenuated and scattered according to the linear susceptibility $\chi^{(1)}$, while evolution is governed by the Green function of the material in response to application of an electric field.

and their corresponding complex conjugates with their signs being determined by right or left action. In particular, for a single field interaction in linear spectroscopy, there are two conjugate terms.

From equation (16), the linear response function is given by

$$S^{(1)}(t_1) = \frac{i}{\hbar} Tr\left[VG(t_1)V\rho(-\infty)\right] \tag{17}$$

or, alternatively,

$$S^{(1)}(t_1) = \frac{i}{\hbar}\theta(t_1)\langle\left[V(t_1), V(t_0)\right]\rho(-\infty)\rangle. \tag{18}$$

This yields the two time orderings

$$J(t_1) = \langle V(t_1)V(0)\rho(-\infty)\rangle, \tag{19a}$$

$$J(t_1) = \langle V(0)V(t_1)\rho(-\infty)\rangle, \tag{19b}$$

and the resulting response

$$S^{(1)}(t_1) = \frac{i}{\hbar}\theta(t_1)\left(J(t_1) - J(t_1)\right). \tag{20}$$

Often of interest is the frequency response of a system. Equation (20) can be rewritten using the Fourier transform relation

$$F(\omega)=\sqrt{\frac{1}{2}\pi}\int dtF(t)e^{-i\omega t}, \tag{21}$$

which has itself as it's own inverse with ω and t reversed. Inserting equation (20) into equation (16) gives the remarkably similar

$$S^{(1)}(\omega_1)=\left(-\frac{1}{\hbar}\right)\left(J(\omega_1)-J(-\omega_1)\right), \tag{22}$$

where here the individual terms are defined as Fourier transforms of the previous time-domain terms, yielding

$$J(\omega_1)=-i\int_0^\infty dt_1 e^{i\omega_1 t_1}J(t_1). \tag{23}$$

Note the use of the one-sided Fourier transform, only over the positive limit. This again limits the signal to the causal domain.

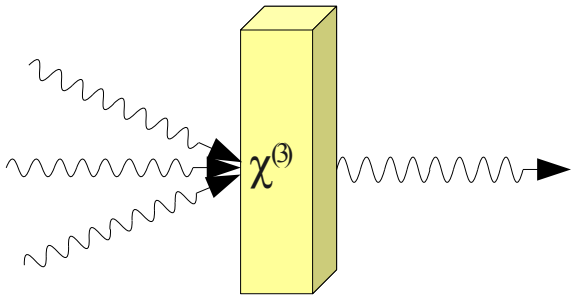

Figure 5: Material interaction to the third order of an electric field. Though this arrangement is slightly disingenuous, it nevertheless portrays the dependence of the exiting light field on the phase and orientation of the incoming fields. Collinear excitation is allowed as well, though the resulting field will look the same in this picture. The response is governed by the third-order non-linear susceptibility $\chi^{(3)}$ of the material.

2.1.3 Third-order Spectroscopy

For three field interactions, equation (16) gives

$$S^{(3)}(t_3,t_2,t_1)=\left(\frac{i}{\hbar}\right)^3 Tr\left[VG(t_3)VG(t_2)VG(t_1)V\rho(-\infty)\right]. \tag{24}$$

Each application of V can again act from the left or the right, giving $2^3 = 8$ total terms in the third-order response function. The intermediate step of reduction to commutators is the same as from equation (17) to equation (18) in the linear case above, yielding the final third-order time domain response function

$$S^{(3)}(t_3,t_2,t_1)=\left(\frac{i}{\hbar}\right)^3 \theta(t_1)\theta(t_2)\theta(t_3)\sum_{n=1}^{4}\left[R_n(t_3,t_2,t_1)-R_n(t_3,t_2,t_1)\right]. \tag{25}$$

The four R here form the set of non-linear response functions generated by unique interaction conditions. In later sections, the specific R_n measured by an experiment will be shown to be dependent on both timing conditions as well as wave vector matching. They are given as

$$R_1(t_3,t_2,t_1)=\langle V(t_1)V(t_1+t_2)V(t_1+t_2+t_3)V(0)\rho(-\infty)\rangle, \tag{26a}$$

$$R_2(t_3,t_2,t_1)=\langle V(0)V(t_1+t_2)V(t_1+t_2+t_3)V(t_1)\rho(-\infty)\rangle, \tag{26b}$$

$$R_3(t_3,t_2,t_1)=\langle V(0)V(t_1)V(t_1+t_2+t_3)V(t_1+t_2)\rho(-\infty)\rangle, \tag{26c}$$

$$R_4(t_3,t_2,t_1)=\langle V(t_1+t_2+t_3)V(t_1+t_2)V(t_1)V(0)\rho(-\infty)\rangle. \tag{26d}$$

As in the linear case, these functions are often useful expressed in the frequency domain. Though this can be done in whole as in the linear case, for many experiments the relevant information is contained in the frequencies during t_1 and t_3, and in the time for t_2. As a result, a partially transformed signal $S^{(3)}(\omega_1, t_2, \omega_3)$ is generally considered. The full frequency domain response is actually a function of not ω_3, but of $\omega_1 + \omega_2 + \omega_3$. This is reduced in most experiments to simply ω_3 by phase matching conditions such that the frequency ω_1 is equal to the frequency ω_2 and, additionally, the sign of the wave vector is opposite. Thus, they cancel, leaving simply the third frequency.

2.2: Liouville pathways

The full response $S^{(3)}$ produces a signal dependent on not just the time orderings between field interactions, but also their k-space wave vectors. For three incident fields, the resulting FWM signal must obey both conservation of energy as well as conservation of momentum. The

general signal wave vector must be

$$k_s = \pm k_1 \pm k_2 \pm k_3 . \tag{27}$$

The signs also indicate interaction with the bra or the ket in the Liouville notation. This results in a large set of possible permutations between both the time and space parameters. Thankfully, only a few are relevant for use with 2DIR spectra.

The FWM signal emitted by the third order polarization falls into two responses. In the first, the phase during t_1 is conjugate to that during t_3. Here, the coherence created during t_3 evolves conjugate to the coherence during t_1, resulting in a return of the phase to the initial point. The result is the so-called rephasing signal S_R composed of the FWM response functions R_1 and R_4. The second response contains no such phase conjugation, and evolution of the t_3 coherence is unconstrained relative to t_1. The result is the so-called non-rephasing signal S_{NR} composed of the FWM response functions R_2 and R_3. The full FWM response can then be rewritten as

$$\begin{aligned} S^{(3)}(t_3,t_2,t_1) \propto \Re\left[R_R(t_3,t_2,t_1)\right]\cos(\varphi_1+\varphi_3) + \Re\left[R_{NR}(t_3,t_2,t_1)\right]\cos(\varphi_1-\varphi_3) - \ldots \\ \Im\left[R_R(t_3,t_2,t_1)\right]\sin(\varphi_1+\varphi_3) + \Im\left[R_{NR}(t_3,t_2,t_1)\right]\sin(\varphi_1-\varphi_3) \end{aligned} \tag{28}$$

for the phase between ϕ_n during t_n. Note that the scaling prefactor and heavyside operators have been dropped for convenience.

There are two common methods of measuring the full response employed in FWM spectroscopy. In the first, a collinear geometry is used for field interactions with k_1 and k_2. This results in the full signal in equation (28) emitted with wave vector $k_{\pm.} = \mp k_1 \pm k_2 + k_3$ where k_+ and k_- are collinear. The signal is collected by interferometric interference with the the third field

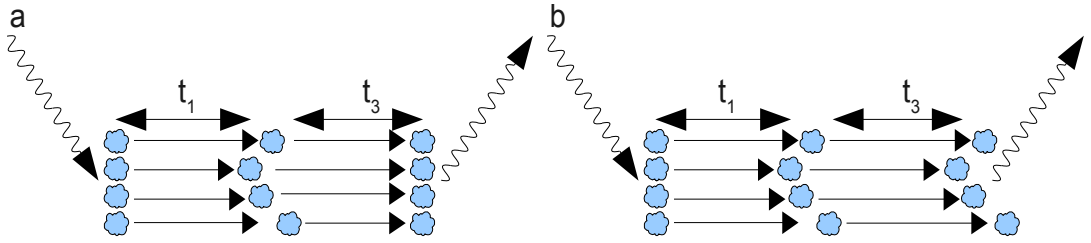

Figure 6: Illustration of rephasing and non-rephasing propagation.
The distribution after t_1 is not in physical space as shown, but in phase space. The molecular phases during t_3 propagate conjugate to t_1 in generating rephasing signal (a), returning the system to the initial phase state, while in generating the non-rephasing signal (b) they continue to propagate independently.

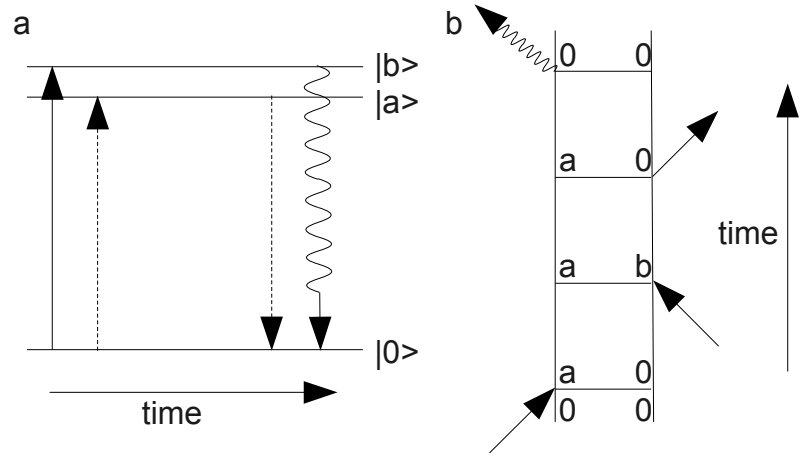

Figure 7: Energy level versus double sided Feynman diagram. On the left (a), absorption (stimulated emission) is denoted by upward (downward) arrows and interaction on the bra (ket) is denoted by solid (dashed) lines. On the right (b), absorption (stimulated emission) is denoted by an arrow pointing towards (away from) the diagram and interaction with the bra (ket) denoted by an arrow on the left (right). The density matrix representation ρ_{ab} is here simplified to only the row and column subscripts a and b. Both diagrams show the same process: a |0a> coherence is initiated by k_1, followed by an |ab> coherence during t_2, then k_3 stimulates emission to a |0a> coherence, which radiates the four wave mixing signal, returning the system to the ground state population. Not present in the energy level diagram is the sign of the wave vector; in the Feynman diagram, a right (left) pointing arrow denotes a positive (negative) sign of the corresponding k.

with k_3, collinear with the resulting signal. Phasing is automatic, with the phases being set by collection of the entire spectrum at once. In the second method, a non-collinear geometry is employed, where k_1 and k_3 are no longer collinear. This results in wave vectors k_+ and k_- also non-collinear, and non-collinear with the third applied field with k_3. These two wave vectors are for the rephasing and non-rephasing spectra as mentioned above. They have complementary angles about the axis of symmetry between k_1 and k_2, and thus are generally collected separately.

Having reduced the dimension of ordering interactions necessary to consider for FWM, we turn to a graphical representation of these interactions. Because the field-matter interaction can occur on either the bra or the ket of the material Hamiltonian, a traditional energy-level diagram becomes difficult to interpret. Alternatively, double-sided Feynman diagrams can be employed to explicitly denote the bra and ket of the system. The system state is contained

between two vertical lines representing the bra and ket. Fields with wave vectors k then interact with either one side or the other with either absorption (pointing towards the vertical line) or emission (pointing away from the line). The direction of the arrow towards the left or towards the right also indicates the wave vectors sign, with a rightward pointing arrow being positive and a leftward pointing arrow being negative.

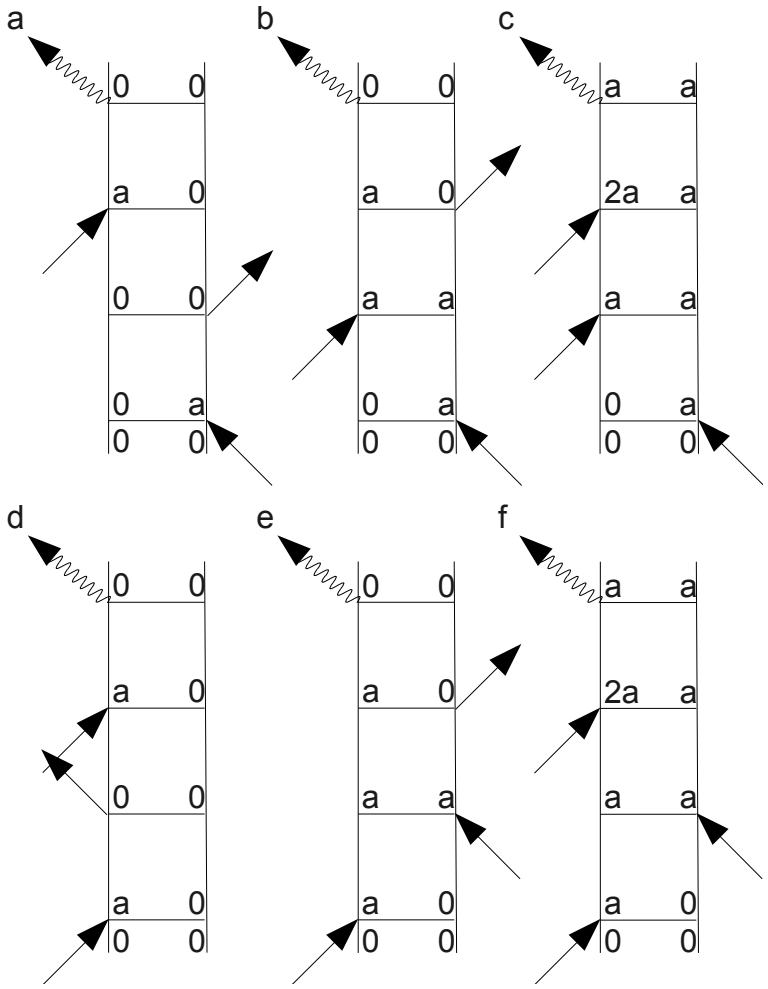

Figure 8: Set of six double-sided Feynman diagrams for FWM. Two signals with wavevectors $k_{\pm.} = \mp k_1 \pm k_2 + k_3$ *of a one oscillator system are shown. Diagrams a through c are rephasing pathways (*$k_R = -k_1 + k_2 + k_3$*) and diagrams d through f are non-rephasing pathways (*$k_{NR} = +k_1 - k_2 + k_3$*). Diagrams a and d propagate in the ground state during* t_2*, while diagrams b, c, e, and f propagate in the excited state. Additionally, diagrams c and f denote excitation to the second excited state of oscillator a (here 2a), giving rise to the anharmonic peak in a spectrum.*

The result is a set of 48 total time ordering diagrams multiplied by a total of 8 sign (spatial) orderings. Restricting this to the set of diagrams measured by FWM to 12 total time orderings between the rephasing and non-rephasing pathways multiplied by a total of 2 spatial orderings, for a total of 24 pathways collected by the standard FWM experiment. Additional experiments can be performed by exchanging the timings, producing unique conditions such as only two quanta coherences created during the t_2 waiting time. A representative sample of the pathways is shown in figure 6. Note that these are only equilibrium pathways, as they all initiate in the 0 quantum of a given state. Non-equilibrium experiments may contain additional pathways depending on the population present upon initiation of the FWM measurement. Also note that this is for a single oscillator system. Additional oscillators result in additional energy levels, geometrically raising the number of pathways that can be written.

Beginning at time zero, the system is assumed to be in a population, be it the equilibrium ground state or an non-equilibrium excited state. The initial field interaction promotes either the bra or the ket to a one quantum excited state in any resonant oscillator whose energy is within the bandwidth of the applied field. This creates a coherence between the 0 and 1 state that evolves during t_1. Application of the second field moves the system to one of three possible results. In the first, the second field acts on either the initial side of the bra and ket to return the system to a 0 quantum equilibrium population (or non-zero non-equilibrium population, but a population nevertheless), or on the opposite side producing an excited population state. In either case, the dynamics during t_2 will be population only, with relaxation being dominant in liquid systems. In the second case, requiring multiple oscillators within the excitation bandwidth, the second field acts on the opposite side from the first to elevate it to the first excited state of a *different* oscillator. The result is a coherence between the first excited state of one oscillator and the first excited state of a second. Such a coherence, in general, has a much lower energy difference than one excited during t_1. For example, in vibrational FWM such as 2DIR the $\upsilon_{0\rightarrow1}$ transition will be in the 1000 to 3000 cm^{-1} range, whereas <1a|1b> coherences between two levels a and b can be as low as a few wavenumbers, or indeed whatever the spacing between two first excited states happens to be. The dynamics during t_2 will be coherence dynamics, with dephasing being dominant. The third case requires a departure from the simplified pathways as laid out above. Here, the timings are exchanged such that $k_s = +k_1 + k_2 - k_3$. Because both initial fields act with the same sign, they act on the same side of the bra and ket. Furthermore, an initial population in the 0 quantum equilibrium state can only absorb. Thus, k_1 and k_2 must both be

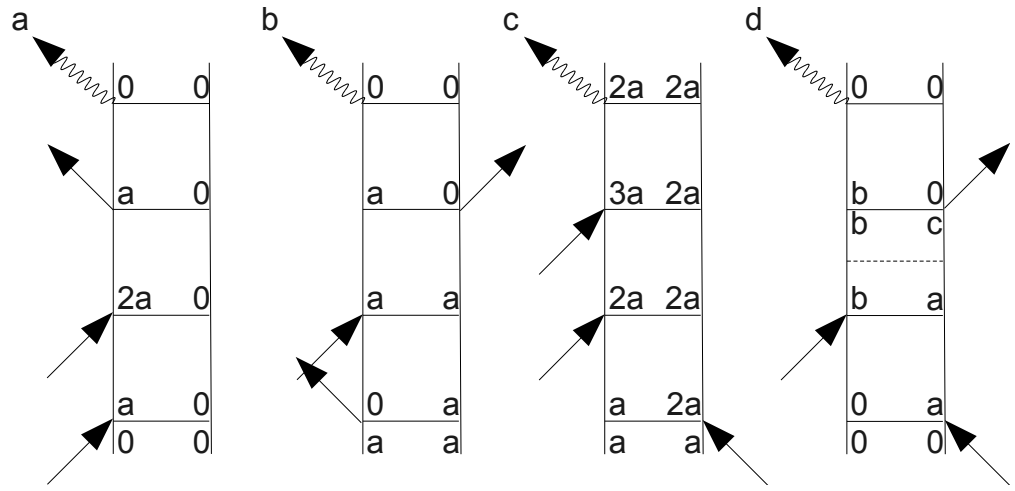

Figure 9: Additional pathways beyond rephasing and non-rephasing. In diagram a, $k_s = +k_1 + k_2 - k_3$, which propagates as a 2 quantum coherence during t_2. In diagrams b and c, the equilibrium ground state population is no longer the starting point, allowing both stimulated emission as the first action as well as excitation to the 3 quantum manifold ($|3a\rangle$). Finally, in d, a non-Redfield term in G is non-zero, producing a coherence transfer from $|ba\rangle$ to $|bc\rangle$ during t_2.

absorptions on the same side of the Hamiltonian. The 1 quantum coherence created during t_1 is then further excited to a 2 quanta coherence during the t_2 waiting time. This is a coherence approximately double in energy compared to the 1 quantum coherence in t_1. Dynamics during t_2 will be 2 quantum-coherence dynamics, with dephasing dominant, but reflect the larger ΔE.

The action of the third field entirely depends on the state of the system after the t_2 waiting time. The molecular response function G is a tensor with entries corresponding to several different types of behavior, and governs the propagation of the system during each of the time intervals t_1, t_2, and t_3. The entries governing behavior during t_1 include pure-dephasing components as well as non-Redfield coherence to population relaxation dynamics.[2] Though a full treatment of the Redfield approximation is beyond the scope of this work, this approximation generally holds in 2DIR experiments, restricting G to off-diagonal pure-dephasing terms and diagonal population relaxation terms and setting all coherence-population terms to zero. Recent work using 2D electronic spectroscopy indicates that this may not be a good approximation for electronic excitons,[3] though further work is needed before the approximation is to be relaxed as a starting point. Entries governing t_2 include similarly many dynamics, as well as population

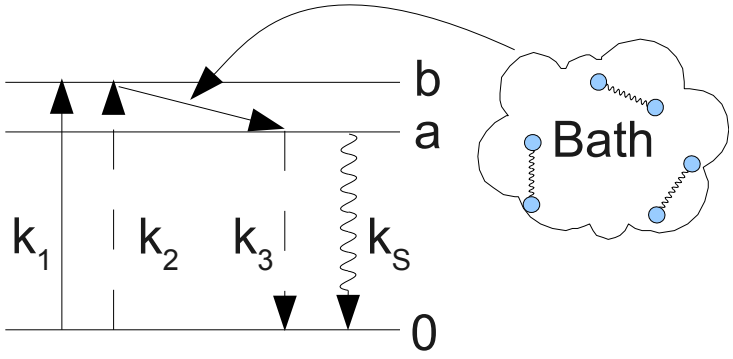

Figure 10: Energy matching between the system and bath energy levels. This allows population transfer, or IVR, from b to a during the waiting time.

relaxation dynamics should an excited state population be evolved by the second field interaction. This presents many possible states with which the third field may interact.

In particular, population transfer can occur in the form of intermolecular vibrational energy transfer (IVR).[4] Here, a population excited at the beginning of t_2 undergoes relaxation to a second state, for example b→a. Energy matching between the difference energy (E_b-E_a) and bath

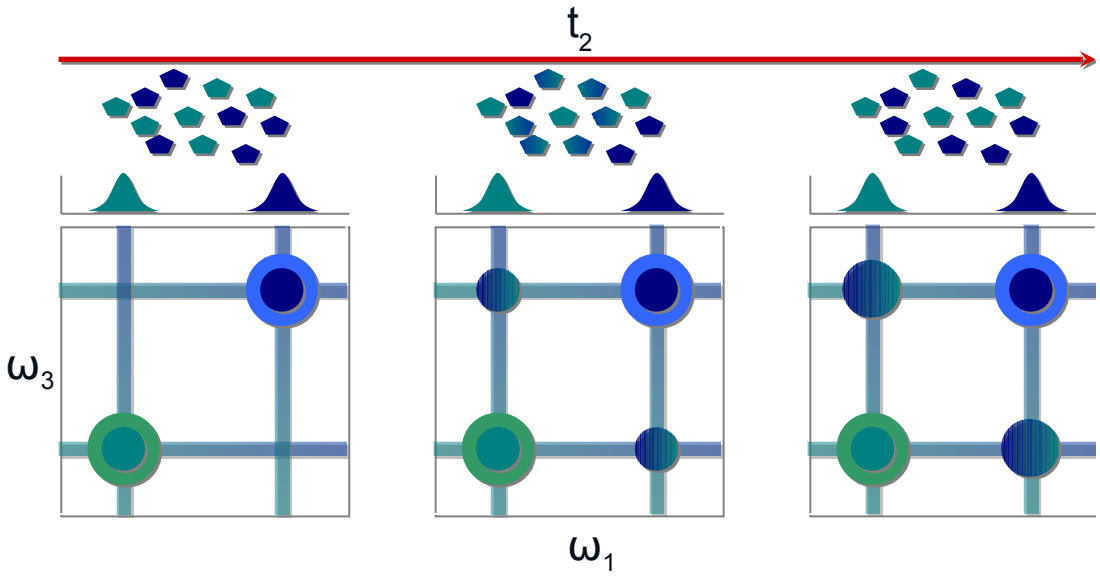

Figure 11: Peak growth with waiting time due to IVR is analogous to exchange. Instead of two transitions on two molecules that undergo exchange, however, IVR occurs when one molecule has two transitions that undergo population transfer during the waiting time.

energies enables this transfer; a higher density of bath modes will provide a higher probability of matching energy levels. This is remarkably similar to the process of population transfer as seen in exchange experiments involving multiple species, and in fact can be thought of in exactly the same way.[5] The difference here is that the transitions arise from the same species, enabling additional energy transfer pathways such as coupling through the ground state, as well as the IVR terms.

In a similar manner, fluctuations that are not well energy matched result in a set of microscopic environments that are sampled as a function of waiting time. This process of spectral diffusion results in line broadening in a linear spectrum that is impossible to extract due to being one of several broadening mechanisms all convolved together.[6] In 2D spectra, however, early time correlation results in a distinctly elongated peak shape along the diagonal. As additional microstates are sampled over t_2 initial excitation frequencies will become correlated with a variety of detection frequencies, which results in a rounded peak shape.

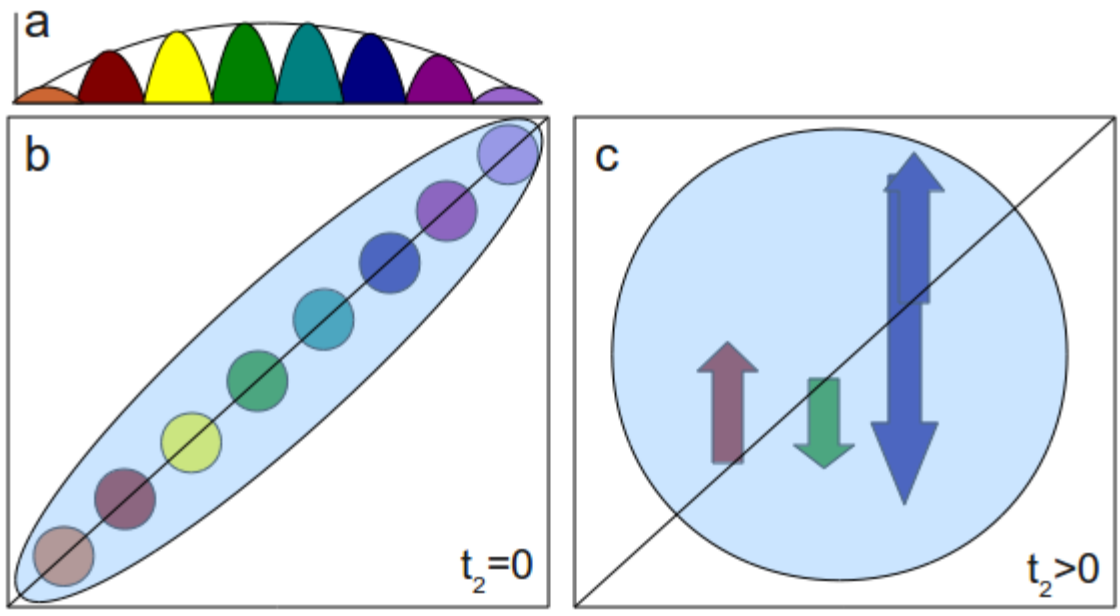

Figure 12: Spectral diffusion produces a signature tilt at early waiting times. (b) Transitions have no time to sample additional microscopic environments, resulting in a highly correlated set of peaks along the diagonal. (c) At later times, memory is lost as multiple microscopic environments produce frequency fluctuations in the correlation frequency. The result is a rounded peak shape. This spectral diffusion sampling impossible to isolate from a broadened peak (a), where multiple sources of brodening may be present.

Regardless, the only action of the third field that will result in a FWM signal produces a coherence of some two energy levels. These energies can be two different quantum states of the same oscillator, such as |a> and |2a>, two of the same quantum states of different oscillators, such as |a> and |b>, but not two different states and oscillators all together—there is no allowed single quantum radiative transition coupling, for example, |2a>|b> to a population, required for emission of signal. Additionally, because one set of pathways involves the creation of an excited states and coherences that persist through t_2, the action of the third field can also create a coherence between a 1 and 2 quanta pair of levels. This directly probes the second excitation manifold of a system, which is not possible using linear spectroscopy. The excitation frequency in the resulting 2D

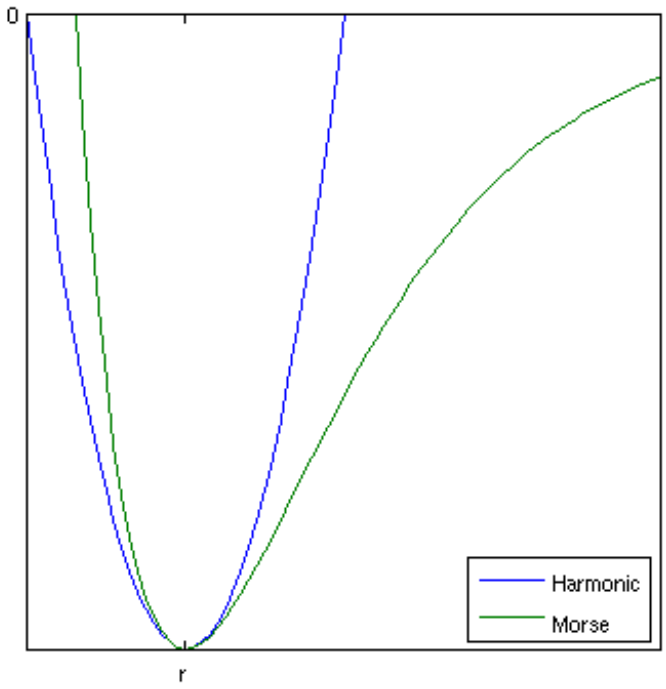

Figure 13: Juxtaposition of a harmonic potential and a Morse potential. Agreement at low energies produces similar ground states, but each successive excited state of a harmonic oscillator will be higher and higher in energy than the corresponding Morse state. This is intuitively due to the behavior between the two attractors at long distances, which is not captured at all by a harmonic oscillator model. The harmonic model also has a finite potential energy at very small distances as well, at odds with realistic models such as the Leonard-Jones model, which (from a chemical perspective) approach near infinite energies.

spectrum will reflect the fundamental 0→1 transition energy while the detection frequency will reflect the anharmonic 1→2 transition energy. In a perfect harmonic oscillator, $E_{0\to1} = E_{1\to2}$. Most real systems, however, are not perfect harmonic oscillators, but are more closely represented as Morse potentials given by

$$V(r) = D_e\left(1 - e^{-a(r-r_e)}\right)^2 \tag{29}$$

which tails to zero energy at long distances. Here D_e is the depth of the potential and a is inversely proportional to the width. The energy level spacing in a Morse potential is not equal, which offsets the anharmonic transition energy from the fundamental frequency. In most systems, this offset is negative, making each successive separation smaller.

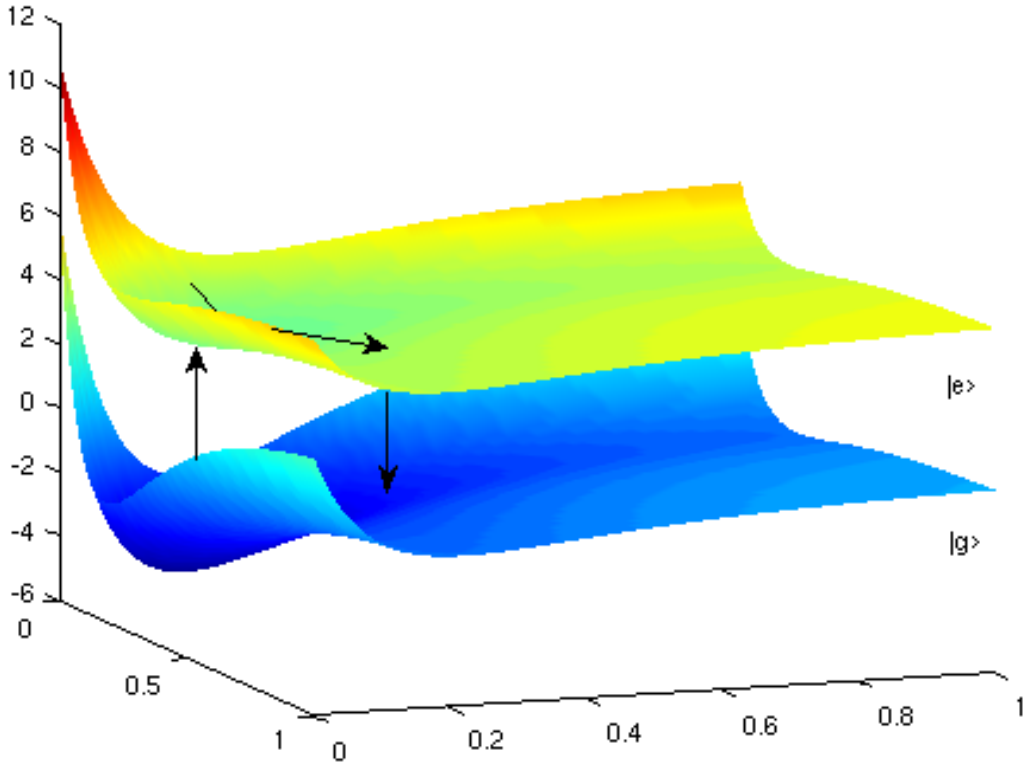

Figure 14: Ground and excited electronic energy surfaces with a transition between. A deep potential well traps the system in the ground state, but excitation to the excited state presents a much shallower potential. The system evolves with the excess energy of excitation away from the equilibrium radius before returning back to the ground state, displaced by the kinetic energy of separation.

The coherence evolved by the third field interaction will evolve with a characteristic dephasing time, resulting in radiation of the FWM signal. This returns the system to either the

equilibrium or first excited state population. In the infrared, these vibrational coherence signals span 10 ± 8 ps. They can be collected in the time domain by scanning techniques, or dispersed spectrally and detected in the frequency domain.

2.3: Excitons

2.3.1 General electronic exciton models

The previous treatment of the non-linear response in general, and the FWM response in particular, makes the convenient local field approximation. Though a full non-local treatment is beyond the scope of this work, excitonic treatment of the systems studied here nevertheless play a crucial role is a complete understanding of the system. While excitonic systems are usually systems of coupled local electronic states that give rise to delocalized molecular orbitals, we show that similar treatments are necessary and effective for highly vibrationally coupled systems where solvation causes dephasing to occur.[7]

Previous non-linear spectroscopy has covered a broad range of electronic excitonic systems, from optical lattices to light-harvesting proteins to quantum dots.[8,9] On the timescale of FWM experiments electronic delocalization is very fast, so the response must be treated in the non-local domain. The result is consistent with the classical HOMO and LUMO picture taught in any general chemistry class, where transitions occur from a delocalized highest occupied molecular orbital to a similarly delocalized lowest unoccupied molecular orbital.[10] This is generally as far as the picture goes, however, as many electronic systems contain a series of unordered levels.[11] The accessible manifold structure present as in, for example, a vibrational ladder is not present electronically, instead quickly breaking down in few excitations into a more complicated set of many oscillators. Indeed, the first electronic excited state is often sufficient to induce dissociation by cleavage of a bond, making the higher lying electronic states at the least more dissociative, if not inaccessible entirely.[12] The result is a system of two molecular objects with diverging trajectories due to residual energy from the electronic excitation.

In the gas phase this is precisely the reaction picture associated with many visibly-pumped transient spectroscopy experiments, used to study the reaction coordinate of separation of bimolecular gases such as HCl.[13] In the solution phase, the picture is muddled by interaction with the solvent, which helps to absorb and disperse directed kinetic energy into the many bath

modes.[14] In the case of homolytic cleavage of the dimanganese decacarbonyl ($Mn_2(CO)_{10}$, DMDC) dimer, for example, although the initial excitation at 400 nm contains several times the bond energy of the manganese-manganese bond and translates into a kinetic energy of separation along the bond coordinate, the packing of the surrounding solvent shell, together with coupling to additional local molecular vibrational modes, prevents the two monomers from actually separating.[15] Calculations show that instead of being driven in opposite directions, the first solvation shell traps them and does not disperse, allowing the monomer only sufficient room to spin in place. This provides enough time for the electronic excitation energy to dissipate into both molecular and solvent vibrational modes and return the system to a relatively cool state. This is sufficient time for the monomers to interact, leading to recombination, all due to solvent trapping effects.

2.3.2 Light Harvesting and the Fenna-Matthews-Olson Complex

Of interest in energy applications, light harvesting proteins such as photosystem I and II are highly studied.[11,16-19] Photosystem II is divided into several segments including a reaction

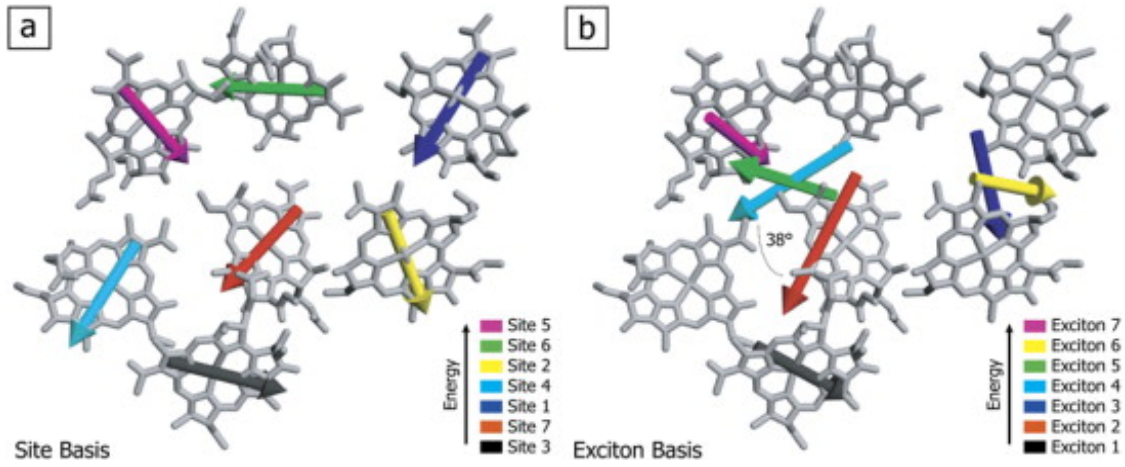

Figure 15: Calculation of the transition dipole moments of the FMO complex. (a) local site basis, (b) exciton basis. Coupling between the individual β-chlorophyll results in a distribution of energy between sites. These coherences have been reported to last much longer than the traditional picture of excitonic coherence would suggest. The position of the FMO chlorophylls relative to both the reaction center and the chlorosome antenna is uncertain, and not shown here.

center that efficiently produces stored chemical energy, a set of chlorosome antenna proteins to capture the incoming light, and the "wire" that connects the two.[20] This wire is the Fenna-

Matthews-Olson complex, the first chlorophyll protein structure solved by x-ray crystallography.[21] Though extensively studied with the goal of understanding electron transport in light energy harvesting, the ultrafast dynamics are only beginning to be probed.[3,17-19] Recently, low temperature 2D electronic spectroscopy (2DES) has been used to probe the ultrafast correlations that are reported to persist for many femtoseconds, significantly longer than most electronic correlations. Treating the system of coupled β-chlorophyll excitonically is critical to capturing these dynamics, as electronic delocalization is the fundamental process by which energy transfer through the FMO wire occurs. Being the strongest transitions, it is hypothesized that excitons 2 and 4 are the primary pathways for electron transfer from chlorosome antenna to the reaction center. The FMO complex would therefore align with the antenna at chlorophylls 3 and 4, the positive end of the transitions, and with the reaction center a chlorophylls 1 and 6, the negative ends of the two primary excitons. Though the specific utility of the arrangement of chlorophyll in FMO is still greatly debated, it is nevertheless clear that the arrangement of proteins takes great advantage of coherence to produce fast and efficient transport through FMO via these delocalized excitons, which is the key feature that is hoped can be captured and extended to artificially constructed light harvesting systems. Even so, additional studies are necessary to fully characterize the role of the observed coherences in energy transport to the reaction center, and to probe the coherence dynamics at temperatures approaching those the chlorophylls are employed at biologically

.

2.3.3 J Aggregates

J aggregates are a striking recent example of the importance of coherence in structure and dynamics. These aggregates are a quasi-one-dimensional system composed of strongly coupled cyanine dye molecules that align along the molecular dipole.[10,22] This causes π-to-π stacking that strongly distorts the aggregate spectrum when compared to the molecular response. Previous work has used functionalization with electron donating and withdrawing groups to perturb the π system and measure the resulting degree of intramolecular delocalization.[23] Additionally, J-aggregates have been shown to be very temperature sensitive. Bath phonons present at room temperatures have been shown to cause coherence dephasing, returning the system response

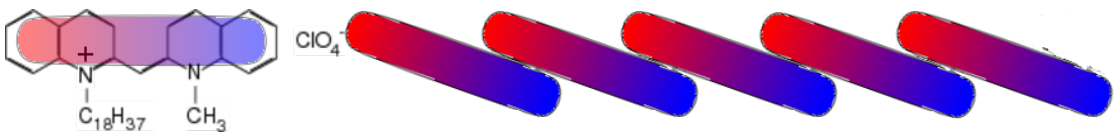

Figure 16: Aggregation of cyanine dipole into quasi-one-dimensional J-aggregate. The dipoles stack along their whole-molecule delocalized π system, effectively creating an extended electron box dependent on the wavefunction overlap between molecules.

from the measured aggregate spectrum to that measured for individual dye molecules.[24] The highly delocalized modes of many dye molecules at low temperatures become uncoupled and localize at the higher room temperatures, creating excitonic traps where the resonance has been removed. Though the alignment of the aggregates remains mostly unbroken, the solvent provides sufficient local site disorder that shifts the individual molecules out of frequency resonance on a fast timescale. This in turn dephases the coherences that would otherwise modulate and distort the measured spectrum.

2.4: Vibrational "excitons"

Though the use of an excitonic model is common in electronic systems, it has only recently begun to be considered in vibrational systems.[7,24,25] Vibrations are generally thought of as either well isolated due to the large frequency and spatial gaps present in many systems, or in the normal mode picture. In a protein, for example, the energetic gap between a C-H stretching vibration and a C-N stretching vibration is sufficiently large as to provide essentially

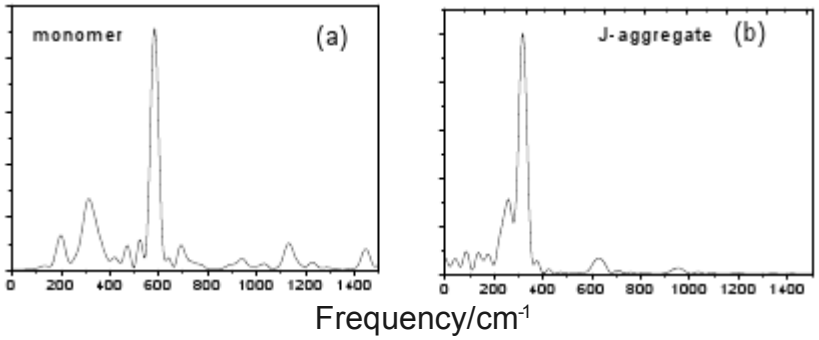

Figure 17: Cyanine vibrational frequency shift with aggregation. (a) monomer, (b) J-aggregate. Electronic coupling suppresses modes that are inconsistent with the aggregate structure and enhances modes that propagate along it.

zero coupling, and the spatial overlap between two C=O groups is also usually small, with separation preventing much coupling. Here coupling is defined in the Hamiltonian sense as the distortion of the otherwise isolated local vibrational C-H and C-N stretching modes; coupling of FWM excitation and detection frequencies through the shared electronic ground state is still observed, but is a different use of the term coupling.

Recently, however, vibrational analogues of electronic exciton systems have been considered in the solution phase. Though vibrational excitons have been studied extensively in the last several decades, most of the research has focused on crystal lattice structures.[8,26,27] Here the periodicity of the lattice causes constructive interference of the semi-local wavefunction, resulting in a high degree of delocalization. This results in phonon propagation through the coupled system, not entirely unexpected in a rigid solid. From this perspective, it would seem impossible to treat solutions in the same manner.

J aggregates in solution, however, have been shown to exhibit intramolecular phonon couping, selectively suppressing uncoupled local vibrational modes.[23,24] Additionally, when either of the two conditions above do not hold, multiple spatially and energetically overlapping vibrational modes couple together to form what is commonly thought of as the normal mode basis. In the case of many of the same strong oscillator it becomes advantageous from a solvation viewpoint to consider the system as a set of excitons. In metal carbonyls we have shown that solvent disorder acts consistent with an excitonic model, where modeling of the bath phonons as simply a disorder parameter creates trapped excitonic states caused by decoupling and localization of vibrational modes that are highly coupled in its absence.[7,28] Indeed, in a system as small as a pair of metals with multiple of the same oscillator coupled together the inevitable result is a highly delocalized vibrational manifold. The distinction from the protein case is the length scales involved in the interactions. In such a small molecule the distance between two oscillators necessitates a high degree of wave function overlap.

References

1. Mukamel, S. *Principles of nonlinear optical spectroscopy*. (Oxford University Press: New York, 1995).
2. Redfield, A.G. On the theory of relaxation processes. *IBM Jr.* **1**, 19 (1957).
3. Panitchayangkoon, G. et al. Long-lived quantum coherence in photosynthetic complexes at physiological temperature. *PROCEEDINGS OF THE NATIONAL ACADEMY OF SCIENCES OF THE UNITED STATES OF* **107**, 12766-12770 (2010).
4. McRobbie, P.L., Hanna, G., Shi, Q. & Geva, E. Signatures of Nonequilibrium Solvation Dynamics on Multidimensional Spectra. *Accounts of Chemical Research* **42**, 1299-1309 (2009).
5. Yamada, Y., Katsumoto, Y. & Ebata, T. Picosecond IR-UV pump-probe spectroscopic study on the vibrational energy flow in isolated molecules and clusters. *Phys. Chem. Chem. Phys.* **9**, 1170 - 1185-1170 - 1185 (2007).
6. Roberts, S.T., Loparo, J.J. & Tokmakoff, A. Characterization of spectral diffusion from two-dimensional line shapes. *Journal of Chemical Physics* **125**, - (2006).
7. King, J.T., Baiz, C.R. & Kubarych, K.J. Solvent-Dependent Spectral Diffusion in a Hydrogen Bonded "Vibrational Aggregate". *The Journal of Physical Chemistry A* **114**, 10590-10604 (2010).
8. Haran, G., Sun, W.D., Wynne, K. & Hochstrasser, R.M. Femtosecond far-infrared pump-probe spectroscopy: A new tool for studying low-frequency vibrational dynamics in molecular condensed phases. *Chemical Physics Letters* **274**, 365-371 (1997).
9. Srinivasan, K. & Painter, O. Linear and nonlinear optical spectroscopy of a strongly coupled microdisk-quantum dot system. *Nature* **450**, 862-865 (2007).
10. Mukamel, S. Communications: Signatures of quasiparticle entanglement in multidimensional nonlinear optical spectroscopy of aggregates. *J Chem Phys* **132**, 241105 (2010).
11. Stone, K.W., Turner, D.B., Gundogdu, K., Cundiff, S.T. & Nelson, K.A. Exciton−Exciton Correlations Revealed by Two-Quantum, Two-Dimensional Fourier Transform Optical Spectroscopy. *Accounts of Chemical Research* **42**, 1452-1461 (2009).
12. Levenson, R.A. & Gray, H.B. Electronic structure of compounds containing metal-metal bonds. Decacarbonyldimetal and related complexes. *Journal of the American Chemical Society* **97**, 6042-6047 (1975).
13. ALEXANDER, M., POUILLY, B. & DUHOO, T. SPIN-ORBIT BRANCHING IN THE PHOTOFRAGMENTATION OF HCI. *JOURNAL OF CHEMICAL PHYSICS* **99**, 1752-1764 (1993).
14. Moore, P., Tokmakoff, A., Keyes, T. & Fayer, M.D. The Low-Frequency Density-of-States and Vibrational Population-Dynamics of Polyatomic-Molecules in Liquids. *Journal of Chemical Physics* **103**, 3325-3334 (1995).
15. Baiz, C.R., McCanne, R., Nee, M.J. & Kubarych, K.J. Orientational Dynamics of Transient Molecules Measured by Nonequilibrium Two-Dimensional Infrared Spectroscopy. *The Journal of Physical Chemistry A* **113**, 8907-8916 (2009).
16. Abramavicius, D. & Mukamel, S. Quantum oscillatory exciton migration in photosynthetic reaction centers. *Journal of Chemical Physics* **133**, 9 (2010).
17. Engel, G.S. et al. Evidence for wavelike energy transfer through quantum coherence in photosynthetic systems. *Nature* **446**, 782-786 (2007).
18. Ishizaki, A. & Fleming, G.R. Theoretical examination of quantum coherence in a photosynthetic system at physiological temperature. *Proceedings of the National Academy of Sciences of the United States of America* **106**, 17255-17260 (2009).
19. Read, E.L. et al. Visualization of Excitonic Structure in the Fenna-Matthews-Olson Photosynthetic Complex by Polarization-Dependent Two-Dimensional Electronic

Spectroscopy. *Biophysical Journal* **95**, 847-856 (2008).
20. Myers, J.A. et al. Two-Dimensional Electronic Spectroscopy of the D1-D2-cyt b559 Photosystem II Reaction Center Complex. *The Journal of Physical Chemistry Letters* **1**, 2774-2780 (2010).
21. Fenna, R.E. & Matthews, B.W. Chlorophyll arrangement in a bacteriochlorophyll protein from Chlorobium limicola. *Nature* **258**, 573-577 (1975).
22. Ginsberg, N.S., Cheng, Y. & Fleming, G.R. Two-Dimensional Electronic Spectroscopy of Molecular Aggregates. *Accounts of Chemical Research* **42**, 1352-1363 (2009).
23. Virgili, T. et al. Coherent phonons in cyanine dye monomers and J-aggregates. *Ultrafast Phenomena XVI* **92**, 370-372 (2009).
24. Virgili, T. et al. Role of intramolecular dynamics on intermolecular coupling in cyanine dye. *Phys. Rev. B* **81**, 125317 (2010).
25. Londergan, C.H., Wang, J., Axelsen, P.H. & Hochstrasser, R.M. Two-dimensional infrared spectroscopy displays signatures of structural ordering in peptide aggregates. *Biophysical Journal* **90**, 4672-85 (2006).
26. Hirata, S. Bridging quantum chemistry and solid-state physics. *MOLECULAR PHYSICS* **108**, 3113-3124 (2010).
27. Nemova, G. & Kashyap, R. Laser cooling of solids. *REPORTS ON PROGRESS IN PHYSICS* **73**, (2010).
28. McCanne, R., King, J.T., Baiz, C.R. & Kubarych, K.J. Vibrational Energy Transfer and Spectral Diffusion Dynamics in a Vibrational Aggregate with Disorder-Induced Delocalization. *Forthcoming* (2011).

Chapter 3

Experimental Methods

3.1: Generation of 2DIR

A commercially available 1 kHz titanium sapphire laser, centered at 800 nm with a 100 fs full-width half-max and approximately 10 nm of bandwidth, is our source.[1,2] From this, 1 mJ is used for generating mid-IR for 2DIR spectroscopy while another 1 mJ is variously used to generate UV, visible, or near-IR for use as a pump in transient 2DIR experiments, as well as the occasional visible-pump visible-probe experiment. The IR generation consists of two sections, each with two parallel and independent lines: optical parametric amplification (OPA), followed by difference frequency generation (DFG). Once generated, the mid-IR is divided for purposes of interferometry. Lastly, a tunable portion, usually 100 μJ, of the uncompressed regenerative amplifier is removed before compression to be used to upconvert IR signals into the visible by means of sum frequency generation (SFG).

3.1.1 OPA

The 1 mJ laser output is split into three portions using a 1 inch thick fused silica window. The first reflection is attenuated by reflective neutral density filters to less than 1 μJ and focused by a 10 cm focal length fused silica lens into a 250 micron c-axis cut sapphire crystal mounted to a movable micrometer stage, generating white light. The white light is a broad continuum of frequencies, spanning more than two octaves of spectral bandwidth, and generated by self-phase modulation in the sapphire.[3] Self-phase

modulation causes an increasing index of refraction with time on the leading edge of the pulse, broadening the initial 800 nm to shorter wavelengths, and a decreasing index of refraction with time on the trailing edge, broadening to longer wavelengths. The result is a temporally chirped contiuum centered around the intial 800 nm input. The measured temporal width is approximately 2.5 ps. The white light is also highly divergent. The ouput is captured by a 10 cm focal length fused silica lens placed slightly further than 10 cm from the sapphire crystal. Though this second lens causes additional temporal stretching, for the purposes of the collinear optical parametric amplification used here this does not effect the temporal profile of the final IR output. The collecting lens slightly focuses the white light, which is then split into two portions and focused into two separate beta barium borate (BBO) crystals to function as the seed in two independent OPAs. The crystal position is adjusted such that optimum focusing is achieved at the

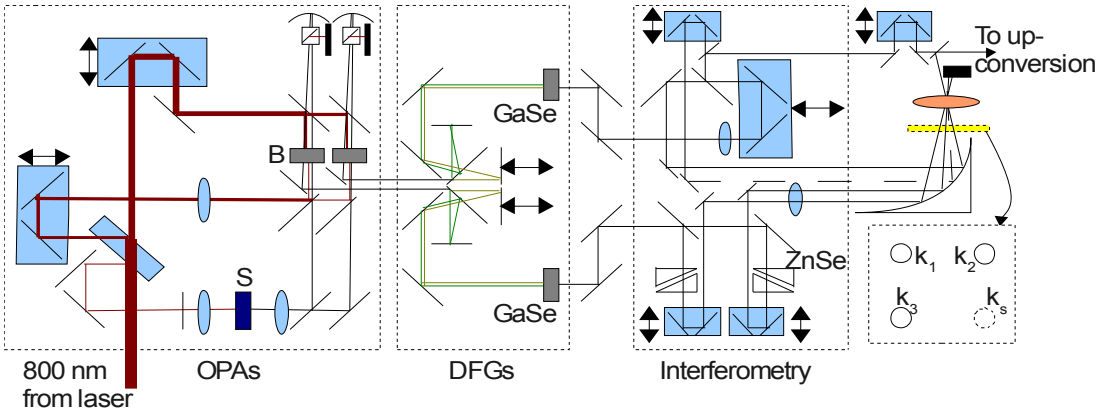

Figure 18: Schematic for converting 800 nm titanium:sapphire laser output to the IR. The three identifiable stages are dual OPAs, followed by dual DFGs, and finally interferometry. Labeled pars in order of left to right are: S = sapphire for white light generation, B = BBO for parametric down-conversion, GaSe = gallium selenide for difference frequency generation, ZnSe = zinc selenide wedges scanned for changing the t_1 delay. All blue rectangles are static delays set to the timing overlap of the incoming two fields, with the exception of the top two interferometric delay, the first of which is step-scanned for the t_3 delay and the second of which can be step-scanned for pump probe delays. The orange oval is the sample. The four fields are arranged in a box geometry with the three fields entering the sample at three corners of a square, producing the signal k_s in the fourth corner of the square.

BBO. An additional delay is geometrically present in arriving at the second BBO in the

second OPA, which is compensated for by a second -50 cm focal length lens. Because of this additional path length, and variation in otherwise 50/50 beamsplitters, the two OPA outputs are never exactly equivalent.

The remaining two portions of 800 nm light are approximately 100 μJ and 800 μJ. The low power portion is the second reflection taken from the initial fused silica window. After reflection, it passes through a delay stage and 20 cm focal length fused silica lens, then is split into two portions. Each is combined collinearly with the white light by dichroic beamsplitter before being sent into a 6 mm long BBO crystal in a type I configuration with identical polarization, forming the two first passes. The white light preferentially seeds parametric down conversion of one 800 nm photon into two tunable near IR photons, the signal and idler, at approximately 1400 and 1900 nm respectively. Energy conservation dictates that while these two photons are tunable, their energies (and thus frequencies) must always sum to the initial 800 nm photon energy and frequency.[4] Altering the vertical crystal angle alters the projection along the optically extraordinary axis with refractive index n_e, which in turn alters the phase matching condition for energy conversion from one frequency to another, allowing the frequency separation between the signal and idler to be tuned to a broad range of frequencies.

The resultant mixture of white light, 800 nm, 1400 nm, and 1900 nm is filtered in two ways, first by passing through a dichroic beamsplitter used to combine the second pass pump with the returning signal and idler, and second by passing through a polarizing beamsplitter cube. In a type I process, the polarization of the signal and idler—here 1400 and 1800 nm—is identical, and opposite to their sum—here 800 nm. The beamsplitter cube rejects the leftover 800 nm pump while passing both signal and idler. Because of similar geometric arrangements, rejected first pass pump from the first OPA is both collinear and cotemporal with the second pass of the second OPA. The additional filter is necessary to avoid the first OPA seeding the second OPA. The signal and idler collimated after filtering by a 10 cm spherical mirror and returned nearly collinearly, with a slight horizontal offset, to the BBO for a second pass of amplification.

The third, high power portion of 800 nm light passes through the initial fused silica window and a second delay stage. It is then telescoped down to match the size of

the second pass signal and idler. Finally, it is split into two roughly equal portions and combined collinearly by dichroic beamsplitter with the returning signal and idler into the BBO crystal, amplifying the first pass generation in a second pass. The signal and idler are isolated by passing through another dichroic beamsplitter, rejecting the leftover 800 nm pump. The OPA output power is measured as the sum of both signal and idler power after filtering. The first passes produce 1 μJ and 0.8 μJ in the first and second OPAs respectively, which the second pass amplifies to produce 150 μJ and 90 μJ, respectively.

3.1.2 DFG

Collinearity is extremely important in the OPAs, or the resulting signal and idler will experience additional spatial separation beyond spatial walkoff in the crystal. Moreover, use of a chirped white light introduces a temporal delay between the signal and idler, which is added to by different indicies of refraction in the BBO crystal for the different frequencies, causing temporal walkoff in the crystal as well. To compensate, the signal and idler from each OPA are separated by dichroic beamsplitter and pass through an interferometric delay. This allows the signal to be delayed with respect to the idler, overlapping them again in time.

Once overlapped temporally and spatially, the signal and idler frequencies generated by the OPAs are directed into two gallium selenide crystals, one for each OPA. This generates light at the difference between the two frequencies—here approximately 5000 nm, or 2000 cm^{-1}. The IR is filtered by passing through a removable dichroic beamsplitter that rejects leftover signal and idler. Removing the filter allows the signal and idler to propogate collinearly along the same path as the generated IR. While the mid-IR cannot be detected directly, the signal can be seen with readily available IR cards or IR viewers. This eases alignment greatly. The filter is then replaced once alignment is achieved. From the 150 μJ and 90 μJ OPA total powers of signal and idler, approximately half is measured after interferometry and DFGs. This generates 2 and 3 μJ of 2000 cm^{-1} with a bandwidth of greater than 150 cm^{-1} and pulsewidth of approximately 100 fs.

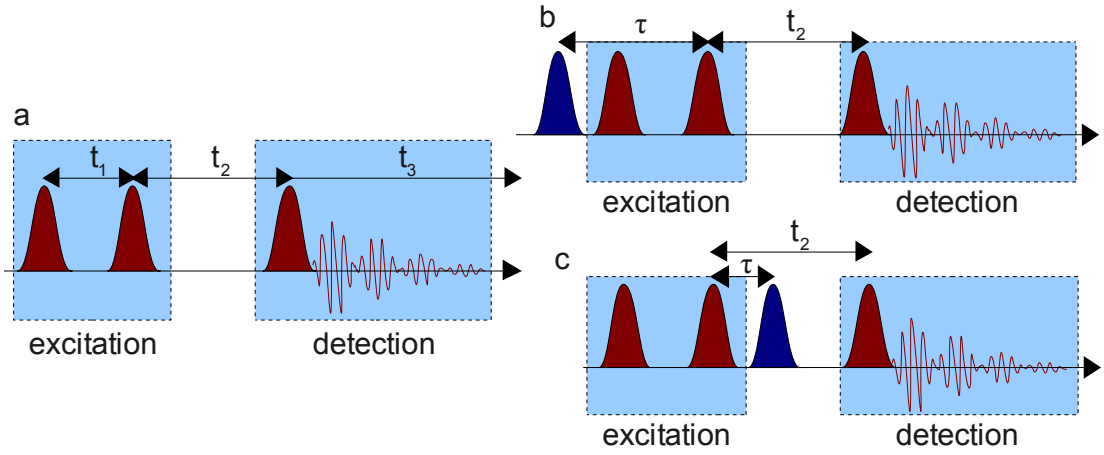

Figure 19: Pulse diagram for Fourier transform 2DIR (a) equilibrium experiments and (b), (c) non-equilibrium experiments. In (a), the initial two pulses create a grating off which the third pulse diffracts, producing the detected signal. Non-linear experiments discussed further on are performed by inserting an excitation either before the 2DIR experiment, allowing for 2DIR monitoring of a proceeding reaction, or between 2DIR excitation and detection, allowing for correlation of excitation frequencies to detected frequencies through the reaction itself.

3.1.3 Interferometer

Two different methods exist to generate a 2DIR spectrum.[5] The first is a frequency domain technique that employs narrow bandwidth excitations along with frequency scanning to generate a full 2D spectrum from individual excitation frequency strips. The second is a time domain technique that scans the time delay between two broad bandwidth and uses a Fourier transform to convert the resulting time domain response into a frequency spectrum. The merits of each will be discussed later. We employ the Fourier transform approach to generate FT-2DIR spectra, and thus must generate temporally scannable broad bandwidth pulses.

The 2 μJ DFG is passes through a 50-50 beamsplitter to create the k_1 and k_2 fields. Each passes through a pair of zinc selenide wedges with one wedge placed on a motor-controlled delay stage.[6] The wedges introduce little dispersion in the infrared. They do, however, provide a non-displacing and very sensitive method of generating a time delay

on each field. The wedge is scanned normal to the axis of optical entry, causing the incoming mid-IR to propagate through greater length of zinc selenide. Increased index of refraction relative to air introduces a time delay relative to the undelayed fields due to the decreased speed of light. The step size is dictated by the step size of the scanning motor, which is 7 nm. The result of scanning the wedge is an indirect step of approximately 0.7 nm, providing nearly attosecond resolution (though still field limited). The 3 μJ DFG similarly passes through a 50-50 beampslitter to create the k_3 field, and the second portion is again split to produce two fields k_{tracer} and k_{LO}. The first is used to align the experiment by tracing out the path in which the the four wave mixing signal will be generated, and can also be used as the probe for pump-probe experiments, while the second is used as a local oscillator reference for heterodyne interference detection of the signal.[7] The k_3 and k_{tracer} fields each pass through a retroreflective stage to generate a non-displacing, motor-controlled time delay with 7 nm step size, providing sub-femtosecond resolution, and the k_{LO} field passes through a static delay stage, set to an sufficient time delay to generate a clean interference signal displaced from the low frequency envelope. The delay resolution even on the directly motor-scanned k_3 is greater than 100 possible points per wave cycle.

The three fields E_1, E_2, and E_3 with wavevectors k_1, k_2, and k_3 are arranged in three corners of a square and focused into the sample by off-axis parabolic mirror to approximately a 250 micron spot The focal point is adjusted to coincide with the crossing point by use of very long 1 m focal length calcium fluoride lenses placed in the k_1 and k_2 paths, and into the path of the second DFG after IR generation but before separation into three portions. The sample is a liquid solution of millimolar concentration placed between two 2 mm width calcium fluoride windows with a Teflon spacer of 75, 150, or 250 μm. The three incoming fields generate a third order polarization that emits a fourth field k_s along the fourth corner of the square. The signal k_s is collimated by a second off-axis parabolic mirror, isolated by adjustable iris, and combined collinearly on a calcium fluoride window with the delayed k_{LO} field. The k_{LO} field passes through a static delay set such that the local oscillator propagates ahead of the four wave mixing signal. The local oscillator is 100 fs in duration, whereas the four wave mixing signal

persists for many picoseconds. Thus, placing the local oscillator earlier in time reduces direct temporal overlap between the two fields. This overlap has been calculated to cause additional phase distortions and noise on the signal, resulting in both distorted absolute value 2DIR spectral lineshapes and make computing the absolute value spectra through phasing the rephasing and non-rephasing spectra extremely difficult, if not impossible.

3.1.4 Two-dimensional spectra

An FT-2DIR spectrum is obtained by collecting many interferograms of k_s and k_{LO} while scanning and recording the time delay t_1 between k_1 and k_2. Each interferogram is converted to the frequency domain, then Fourier transformed. The signal is isolated from the low frequency envelope by super-gaussian window and inverse Fourier transformed back to the frequency domain. The collection of these spectra are then Fourier transformed along the t_1 axis to produce the conjugate excitation frequency axis ω_1. The detection frequency axis ω_3 is the CCD detected frequency after filtering. Heterodyne detection of the signal allows extraction of the full signal field, necessary for phased detection of 2D spectra.

A series of two dimensional spectra can be taken by iterating the above process while stepping the k_2 delay. This provides a finely controlled set of 2DIR spectra that are vibrational snapshots of the system for a given "waiting time" t_2. This can be thought of as the allowed propagation time between labeling the molecule (k_1 and k_2 excitation) and subsequent readout of molecular evolution (k_3 excitation and resulting signal emission). This yields the three dimensional data dependent on two frequencies ω_1 and ω_3 and on one time t_2.

3.1.5 FT-2DIR vs. double resonance 2DIR

There are advantages and disadvantages to employing both methods of 2DIR spectroscopy. Both require the generation of mid-IR as described through 3.1.2, but from there they differ. The narrow bandwidth pump, broad bandwidth probe double resonance

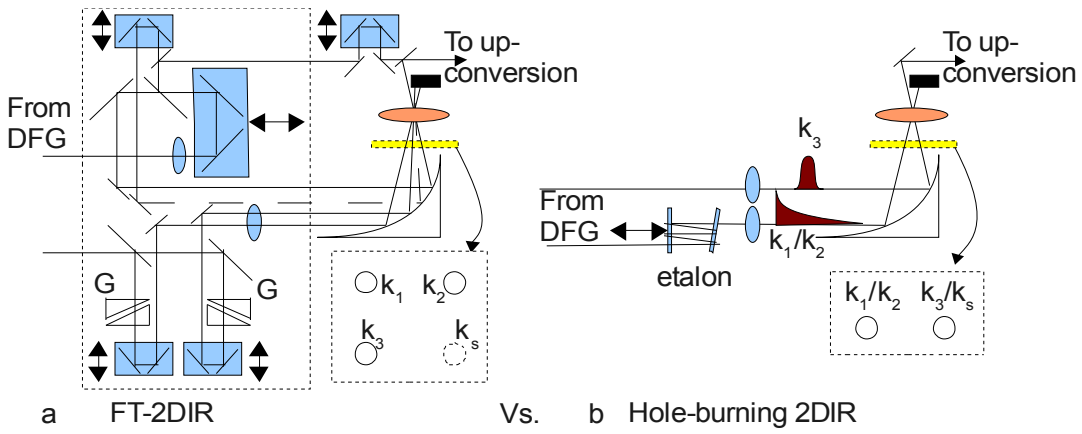

Figure 20: (a) Fourier transform 2DIR pulse generation schematic from DFG on as compared to (b) Double resonance pulse generation method. The double resonance method uses a simpler design, but requires a temporally longer pump pulse.

method takes the relatively broad mid-IR output from the DFG and generates a narrow pulse using one of any available methods. The most commonly employed technique uses a tunable Fabry-Pérot interferometer, or etalon, which selects a narrow frequency that is resonant with the etalon length.[5] This functions exactly like a laser cavity, amplifying any frequency whose wavelength constructively interferences upon reflection and suppressing all other frequencies. Note that this technique by nature requires a sufficiently narrow IR bandwidth to begin, i.e. less than a full octave of bandwidth must be employed or multiple frequencies will be resonant in the etalon.

The advantages to using a narrow bandwidth pulse include direct detection of the absorptive spectrum, ease of alignment, and simplification of 2D spectrum generation. Because the two initial field interactions k_1 and k_2 occur collinearly from the same pulse, the 2D signal emits collinear with the k_3 probe and includes both the rephasing and non-rephasing pathways together. The signal is then detected interferometrically by interference with the k_3 field. This simplifies every aspect of 2D spectrum generation, as less optics are involved in creating the fields, and fewer beams are necessary to align because of collinearity. The drawbacks to employing narrow bandwidth pulse include the inherently smaller information subset detected, reduced temporal resolution, and a high background signal. Because the absorptive spectrum is detected directly, not all

information contained in the rephasing and non-rephasing spectra is recorded. Instead, the absorptive spectrum is the sum of the real parts of the two spectra, meaning any pathways that interfere and cancel with not be represented in the resulting signal. The dispersive spectrum is calculable as well, though often overlooked, but contains the same limitation, in that it is composed of the sum of the imaginary parts. Additionally, by the Fourier transform relationship, a narrow bandwidth excitation will have a larger temporal width. This limits the resolution in either the time or frequency dimension. A higher frequency resolution requires a narrower bandwidth, in turn requiring a wider temporal width, and vice versa. Thus frequency resolution at early times is necessarily impossible to achieve with the double resonance method. Additionally, a longer temporal width will result in lower peak power, which in turn results in a lower signal strength. Finally, by employing a collinear geometry for the initial excitation, the signal is emitted collinearly with the probe field. While this simplifies actually detecting the heterdyne signal, it also creates a large background upon which the signal is superimposed. This makes finding the signal for weak absorbers more difficult.

The Fourier transform method proceeds as described in 3.1.3 and 3.1.4. The mid-IR output from the DFG is replicated into several fields, which are then arranged non-collinearly to produce a signal in a background free direction. This eases signal detection in weak absorbers, and simplifies attribution of signal features as the signal is not interfering with an additional field. Because a narrow bandwidth is not required, the full bandwidth available can be used, resulting in temporal pulse widths limited only by the width that can be generated out of the DFG. This provides excellent temporal resolution. Spectral resolution is achieved by longer temporal scans, which can actually be performed, or the interferograms simply padded after the fact with additional points at times longer than signal is actually generated. This sidesteps the Fourier transform relationship between temporal and spectral width and allows high resolution in both, making acquisition of fine frequency resolution at early times possible. Finally, the rephasing and non-rephasing spectra are detected independently, making additional information available. The drawbacks to employing the Fourier transform method revolve around additional experimental constraints and a higher degree of complexity.

The DFG outputs must be split into multiple fields, which must then be aligned separately, and an invisible signal further aligned once it is generated. In practice, these concerns are minimal. Indeed, we have also employed the collinear excitation method using a Fourier transform and temporal scanning rather than frequency scanning. This can be done by making the two pump fields k_1 and k_2 as shown in Figure 3 collinear and scanning the time delay between them in the same manner. The signal then emits collinearly with the third field k_3 as in the double resonance method. It was found that signal strength is extremely sensitive to collinearity, and signal levels significantly lower than the non-collinear design. Together with the inherent coupling of temporal and spatial resolution in the collinear double resonance method, non-collinear FT-2DIR presents a more attractive experimental profile.

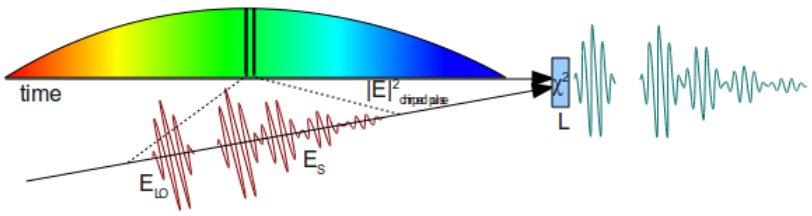

Figure 21: Upconversion of signal and local oscillator fields by sum frequency addition to a highly stretched chirped pulse. L = lithium niobate crystal used for SFG.

3.2: Upconversion

The incoming oscilator into the regenerative amplifier is deliberately highly chirped for amplification by passing through a grating stretcher. This is required to fully amplify the incoming seed without burning the titanium sapphire crystal. The laser is then recompressed after amplification, resulting in both a high power and short pulse. This process uses a folded grating compressor, where the amplified chirped ti:saph output is dispersed from a grating and returns after reflection from an adjustable retroreflector, which can be used to adjust the final laser compression. The initial diffraction via grating

is necessarily slightly lossy, as gratings are never perfect. The result is a series of grating reflections of positive and negative order, and an undiffracted zero-order reflection. This reflection is still highly chirped, and is ordinarily dismissed as loss. We have made use of it in a novel application, however, by using this chirped pulse to upconvert the IR signals into the visible using SFG.[2] This innovation provides many benefits, including increased sensitivity and decreased acquisition time. The work described in this thesis is not only the first of its kind with respect to the methods developed to generate the transient nonlinear signals, it is also the first to employ upconversion detection. In fact, much of what was accomplished was made possible precisely due to the enhanced sensitive provided by chirped-pulse upconversion (CPU).

Initially our implementation of CPU was done using the zero order reflection from the compressor grating. Sufficient work on low power IR signals, however, indicated a preference for the ability to tune the amount of chirped pulse available for upconversion. Further, in replacing the compressor grating with a newer model after damage was discovered, it was found that the zero-order reflection had diminished to less than 10 μJ of energy. Use of the zero-order spot was succeeded at this point by insertion of a half-wave plate and a polarizing beamsplitter oriented horizontally, both coated for anti-reflection at 800 nm. The wave plate allows the polarization of the laser output to be adjusted before entering compression. The polarizing beamsplitter then passes the purely horizontally polarized portion for compression in the stretcher while reflecting the vertically polarized portion out of the laser as the chirped pulse. This has allowed us to directly adjust the power of the chirped pulse for upconversion, proving invaluable for small signals. The additional chirp imparted by passage through the polarizing beamsplitter is small and primarily linear, and is easily compensated for by adding a small additional delay in the compressor.

Given a changing time delay between the initiation of signal at interaction with k_3 and the center of the chirped pulse, the signal will temporally overlap with a changing chirped pulse frequency. This results in a drift in the upconversion frequency, which is eliminated by locking the two to the same delay stage. The chirped pulse exits the laser and is telescoped down, then passes through a retroreflector mounted to the k_3 delay

stage. The chirped pulse is then delayed statically to temporally overlap with the signal and local oscillator and focused by a 20 cm spherical mirror into a wedged lithium niobate doped magnesium oxide crystal non-collinearly with the signal and local oscillator, also focused by the spherical mirror. The chirped pulse is sufficiently long in time that signal reflections in the crystal still temporally overlap and can thus still upconvert. A wedged crystal is employed redirect additional reflections and prevent interference.

Two lithium niobate crystals are employed in separate experiments for two purposes. First, a thin crystal wedge of width 0.3 to 0.8 mm is employed for large amplitude signals where larger detection bandwidths are required. Second, a thicker crystal of width 4 to 4.5 mm is employed for low amplitude signals. Non-linear amplification occurs proportional to the length squared of the crystal used, translating to a factor of 20 signal amplification of the thicker crystal over the thinner. Conversely, the bandwidth acceptance decreases as the inverse of the crystal length, producing a smaller range of upconverted frequencies in the thicker crystal. The thicker crystal dimensions were chosen to still provide 100 cm^{-1} of upconverted bandwidth. In practice, due to real world concerns, this is closer to 80 cm^{-1} due to the steep drop off in phase matched power. The thinner crystal produces greater upconverted bandwidth than the IR pulses and is not limiting.

The bandwidth of the chirp pulse is 10 nm with a 350 ps FWHM, approximately 700 ps from base to base. The linear chirp over the relatively long time comparted to the signal provides a narrow frequency for signal upconversion, with the four wave mixing signal on the order of several picoseconds in time overlapping with only a narrow frequency slice of the chirped pulse. The SFG signal for the 800 nm chirped pulse plus the 5000 nm signal is centered around 690 nm. A short wavelength pass filter removes the 800 nm chirped pulse, and the signal is dispersed by a 1200 grooves/mm grating in a spectrometer and detected in the wavelength domain by conventional CCD camera. The spectrum is detected synchronously with the laser output at 1 kHz by camera triggering and by limiting the active area of the CCD array to 1340x20 pixels that are binned vertically to produce one 1340 pixel spectrum.

A slight vertical tilt is observed in the upconverted spectrum. This is due to the conservation of momentum in the wave vector addition in the SFG process. A signal of finite temporal width will upconvert with a, albeit narrow, range of chirped pulse frequencies. Higher chirp pulse frequencies contain a slightly higher energy, such that addition of the signal and chirped pulse wave vectors, which is weighted by their energies, results in a range of upconverted wave vectors with slightly differing angles. The phase matching angle of the crystal is arranged to be in the horizontal dimension. The signal and chirped pulse are thus arranged non-collinearly in the vertical dimension upon entering the crystal, resulting in the spread in wave vector angles also being vertical (as well as removing non-collinear phase matching concerns). The spectrometer-diffracted line is then titled over approximately 5 vertical pixels of the CCD camera as well as being dispersed across the 1340 horizontal pixels. The vertical binning ensures that this tilt has effect on detection.

3.3: Transient spectroscopy

3.3.1 Narrowband excitation

Photoexcitation frequencies were derived in two ways. Using the remaining 1 mJ of source laser, a narrow bandwidth pump at either 400 or 266 nm was obtained by doubling or tripling the laser fundamental. Alternatively, a broad bandwidth non-collinear optical parametric amplifier (NOPA) was implemeted to produce tunable pulses across the visible. The NOPA will be discussed in the next section, while the doubling and tripling are briefly mentioned here.

The 1 mJ of 800 nm is attenuated, collimated and directed at normal incidence into 400 micron thick BBO cut at $\theta = 29.2^{\circ}$ and $\Phi = 0^{\circ}$. This is the optimum phase matching angle for the production of the second harmonic 400 nm of 800 nm. The resulting near UV is necessarily collinear with the 800 nm pump, and is separated by use of two narrowband mirrors that reflect only the second harmonic at great than 90% efficiency. The output power of 400 nm is made tunable by use of a polarizing

beamsplitter and waveplate placed in the 800 nm fundamental, where these introduce less temporal broadening. Powers over 100 mJ have been achieved, though actual experiments were generally performed with between 1 and 10 mJ.

Production of the third harmonic 266 nm of 800 nm is achieved by a similar mechanism, but in two stages. The 1 mJ of 800 nm is attenuated and passes through the

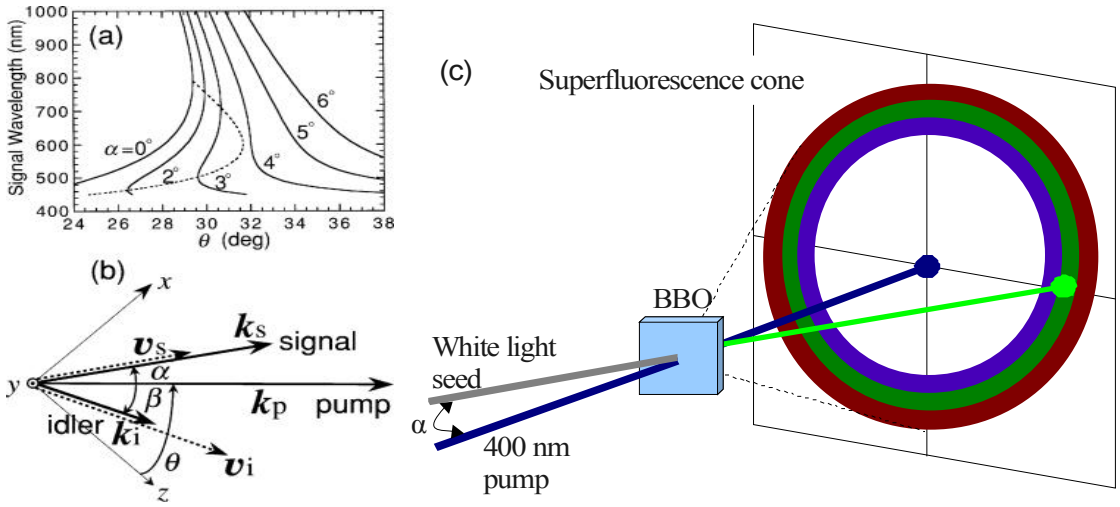

Figure 22: (a) Optimum phase matching angle for two incoming fields with separation angle α in the BBO crystal. A angle of 0˚ corresponds to collinear, which requires several degrees of crystal angle to cover the visible. At 3˚ of separation, however, a crystal angle just over 30 degrees covers from 475 nm to more than 800 nm of bandwidth. (b) Illustration of the superfluorescence cone created by parametric downconversion of the incoming 400 nm pump based on the vectors shown in (b). The cone angle is dictated by the BBO crystal angle, and in turn dictates the optimum crossing angle α between the pump and the seed.

same polarizing beamsplitter and waveplate for tunable output power, and is then focused by a 25 cm fused silica lens into the same BBO crystal used for doubling, placed several centimeters before the focus. Instead of rejecting the remaining 800 nm, however, it remains collinear with the 400 nm second harmonic, and the pair continue focusing into a second 300 micron BBO crystal cut at $\theta = 44.3^\circ$ and $\Phi = 0^\circ$. This is the optimum phase matching angle for the SFG process of 800 nm plus 400 nm, resulting in the third harmonic 266 nm. It was found that, although some temporal walkoff is introduced by propagation through the first BBO doubling crystal, the addition of a dispersive material between the two BBO stages was both ineffective and unnecessary in generating

sufficient output power for experiments.[8] The third harmonic is filtered by four passes on narrowband mirrors that reflect only 266 nm at greater than 90% efficiency. Powers of as high as 10 mJ were measured, though actual experiments were performed with between 1 and 5 mJ.

3.3.2 Broadband generation and excitations

To access portions of the visible spectrum unavailable using narrowband SFG methods, a NOPA was implemented. In an optical parametric amplifier (OPA), the incoming fields are aligned collinearly. This simplifies both the theoretical and experimental concerns regarding the field-crystal angle, and generally results in a fixed preferred frequency of parametric conversion with a relatively narrow bandwidth. In BBO, for parametric down-conversion of 800 nm to ~1400 and ~1900 nm, the limiting bandwidth is determined by the longer wavelength 1900 nm, resulting in approximately 300 cm^{-1} of bandwidth. This is more than sufficient in the IR to cover several transitions of interest. In the visible, however, for parametric down-conversion of 400 nm to ~550 nm (here the complementary ~1500 nm is of no interest), the bandwidth is only around 30 cm^{-1}. In the visible, centered at 550 nm, this generously yields a field spanning 549 to 551 nm. Even 300 cm^{-1} of bandwidth at 550 nm yields a field with only 20 nm of bandwidth. Clearly, this method is insufficient for generating broad bandwidth pulses.

This is acceptable for simple transient excitations in the visible, as most visible absorptions are very broad. Any frequency generated within that broad absorption is generally sufficient to excite the transition of interest. Further, OPAs can be tuned by angle, so as long as a single experiment does not require the broad bandwidth or multiple excitation frequencies, the transient pump can simply be tuned between experiments. Generating visible by parametric down-conversion, however, is limited to frequencies less than the initializing pump, in this case doubling of the ti:saph output to 400 nm. This leaves the near UV range below 400 nm impossible to access. Many reactions can be initiated by molecular absorption in this region, making it of vital importance to access with a pump pulse.

The solution to both the tuning problem and the higher energies problem is the

implementation of a non-collinear OPA (NOPA). The phase matching bandwidth for a given field highly depends on the incoming angle.[9] A NOPA takes advantage of changing this angle for only one of the incoming fields, resulting in a higher bandwidth for this field, while retaining the angle of maximum parametric conversion between fields. The

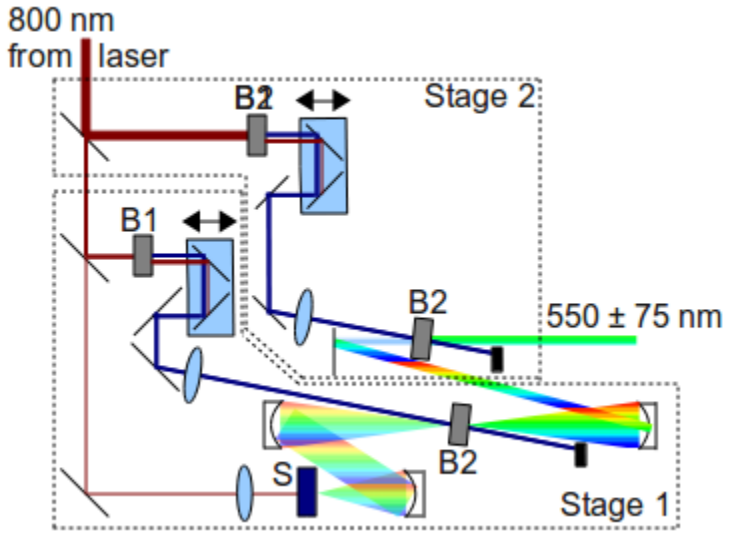

Figure 23: Schematic of the NOPA implementation. Labeled items are: S = sapphire for white light generation, B1 = BBO crystal cut at 29.2˚, B2 = BBO cystal cut at 31˚. Stage 1 generates 5 μJ of broadband visible, Stage 2 amplifies to 50 μJ.

result is a much broadened phase matching bandwidth, over almost the entire visible spectrum. When seeded with a low power white light continuum, easily generated in a sapphire crystal, the result is parametric conversion of over 2500 cm^{-1} of visible bandwidth, which is sufficient to cover over 100 nm centered at 550 nm. This, too, is tunable, allowing for very broadband coverage of the entire 400 to 800 nm region.

Using 250 μJ of laser output at 800 nm, a small portion is attenuated and used to generate white light by focusing into a sapphire crystal. This is the same procedure used in generating the seed for the OPAs in converting 800 nm light to near IR. The white light is collimated by spherical mirror to reduce further dispersion. The remainder is collimated into a BBO crystal cut at $\theta = 29.2^\circ$ and $\Phi = 0^\circ$. This is the optimal phase matching angle for type I SHG, producing 85 μJ of 400 nm light, which is then used as

the pump for parametric down-conversion into the visible. The white light is focused by a 15 cm focal length spherical mirror with an external angle of 6˚ relative to the 400 nm pump (corresponding to an internal angle of 3˚), which is focused by a 25 cm fused silica lens. The two converge on a second BBO crystal cut at $\theta = 31^{\circ}$ and $\Phi = 0^{\circ}$, the optimal NOPA angle for type I conversion, as indicated in Figure 3.4.

Electromagnetic pulses have a fundamental minimum temporal width related to the amount of spectral width due to the time-frequency Fourier relationship. A pulse with a spectral width of 1 cm^{-1} has a so-called transform limited temporal width of $\Delta t = (\Delta \upsilon * c)^{-1}$, or 33.3 ps, where c is the speed of light, $\Delta \upsilon$ is the spectral bandwidth, and Δt is the temporal width. To achieve few femtosecond temporal widths, then, requires a spectral bandwidth of more than 3000 cm^{-1}. The transform limit, however, assumes temporal alignment of the entire range of frequencies present in a pulse. Dispersion, which is dependent on frequency, will result in those frequencies spread out in time. In particular, second-order spectral dispersion results in a first order temporal dispersion, also known as a linear chirp. The frequencies are spread out linearly in time, with a positive chirp increasing in frequency with time and a negative chirp decreasing in frequency with time.

Because of the nature of both the white light seed and the parametric down-conversion, the resulting pulse is broadened relative to the 100 fs input (here closer to 85 fs due to narrowing during doubling of 800 nm to 400 nm). The visible output centered at 550 nm is chirped over ~500 fs. Shorter pulses achieve two goals: firstly, they provide better time resolution for visible experiments. In combining visible excitation with 2DIR, this is important to allow closer arrangement of the visible excitation in time to the IR. Secondly, in order to reach the near UV for excitation, we can double the NOPA output using SHG in BBO. Furthermore, better non-linear conversion of first to second harmonic is achieved with higher peak powers. Thus, in order to reach viable energies in the near UV for use in transient 2DIR experiments, the NOPA output must be compressed from chirped to transform limited.[10]

Previous work has had much success in generating broadband visible pulses using modified NOPAs that include spectral broadening of the pump for greater angular phase

matching in the BBO crystal, temporal broadening of the pump for greater temporal overlap with the highly chirped white light seed, pre-compression of the white light to a shorter temporal pulse width, and pulse front tilting to best match the seed beam profile.[11-14] Each of these methods provides a broader resulting bandwidth at some expense. In the case of spectral broadening, a prism is often employed, which while increasing the angular dispersion also serves to increase the higher order spectral dispersions of the pump. This effect is not negligible to a transform limited 100 fs 400 nm pulse. In the case of temporal broadening, output power is lowered twofold, as some pump power is lost in stretching the pulse and further output power is lost due to lower peak power in the BBO crystal. In the case of pre-compression, the use of a grating compressor adds a great deal of length and complexity to the optical setup for marginal gains. Indeed, calculations show that compression is highly dependent on the white light output, and in some cases it cannot be compressed at all. In the case of pulse front tilting, complicated apparatus are again needed to produce a result that is impossible to visually identify, making optimization problematic.

Especially when introducing additional temporal broadening elements, the final NOPA output will need to be compressed to achieve the goals above. Though mirrors are available that provide some dispersion upon reflection, the total amount is usually very small, generally on the order of 50 fs^2. A broadband NOPA output on the other hand can be chirped over 1000 fs^2, requiring many passes on very expensive chirped mirrors. Additionally, chirped mirrors are designed for maximal second order and minimal higher order dispersion, but still impart a small amount of the higher order. Multiple passes will accumulate additional higher order dispersion, eventually resulting not in a transform limited pulse, but in a more complicated pulse structure in higher orders than linear temporal dispersion.

To compensate for all orders of dispersion we have implemented a phase mask that can manipulate the phase of each frequency individually to the resolution of the mask.[15] The NOPA output is dispersed from a grating and collected by spherical mirror. This collimates the dispersed frequencies in the horizontal direction while focusing the vertical to a single pixel line. This is imaged onto our phase mask, a electro-optic 19

pixel membrane deformable mirror. The 19 channels provide the control to implement up to a 22nd order polynomial on the mirror surface (including the two pinned edges) in the horizontal dimension, allowing it to correct up to very high order dispersions. Though there is some spatial dispersion produced by a smooth membrane deformation, this is

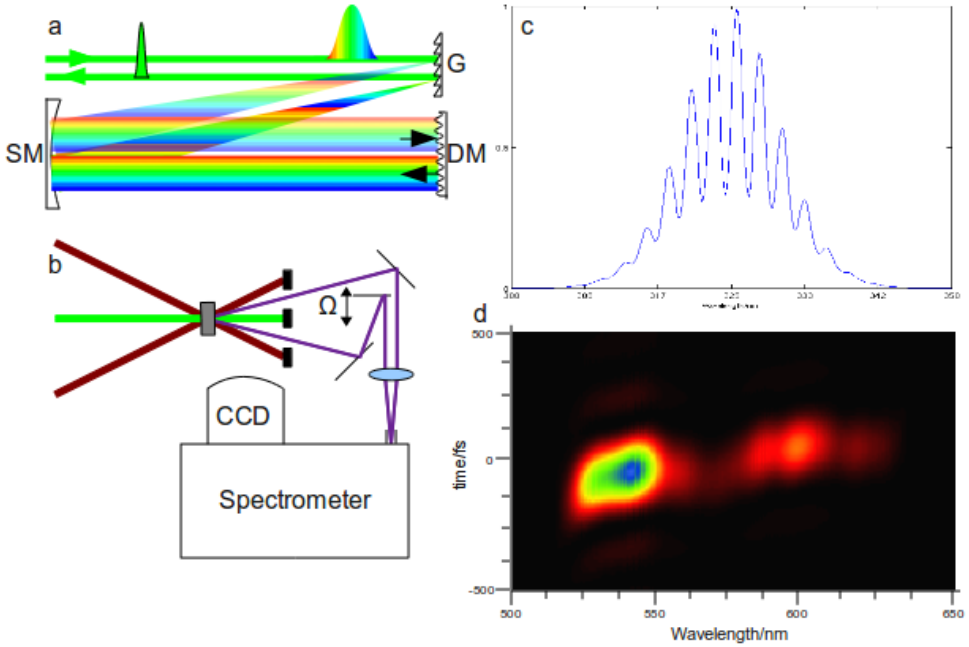

Figure 24: NOPA compression process. In (a), the NOPA enters a folded grating compressor, where a 19 channel deformable mirror alters the temporal phase. The incoming and outgoing beams are offset vertically for clarity. The NOPA profile is then measured in (b) by ZAP-SPIDER using left over the zero-order reflection of the chirped 800 nm output from the regenerative amplifier. The result is an interferogram such as (c), from which the NOPA phase and amplitude are extracted. The full sonogram of amplitude versus time is plotted in (d).

limited due to the maximum deformation distances. The membrane operates by high voltage attraction of the grounded mirror surface underlayer to the channel side high voltage. The edges are pinned in place, providing the central channel the largest possible deformation relative to zero voltage. The central channel maximum negative deformation is -6 μm. Using negative deformation on the outer channels with positive deformation on the central channel results in a maximum positive deformation of 2 μm.

Deformations of this size result in an angular spatial dispersion of much less than the error on the collimating spherical mirror.

To monitor the compressed output, zero-additional-phase spectral phase interferometry for direct electric field reconstruction (ZAP-SPIDER) was used, providing single shot detection of the full spectral amplitude and phase. ZAP-SPIDER uses two copies of a strongly chirped pulse to upconvert an unknown pulse by sum frequency generation in a non-linear crystal, here BBO.[16] The NOPA output was mixed with two copies of chirped pulse, derived from the zero-order reflection in the regenerative amplifier grating compressor, converting the 550 nm NOPA output to the near UV around 325 nm. One of the two upconverting chirped pulses was delayed with a known static delay Ω, known as the shear. This gives the upconverted UV pulses two slightly different center frequencies ω_0 and $\omega_0 + \Omega$. The value of Ω is determined by monitoring sum frequency generation of the two chirped pulse copies to find $\Omega = 0$ and delaying one copy with a static delay stage. The frequency can then be calculated from the known chirp of the chirped pulse. Once set to an experimentally optimal value, usually around 1 THz, this delay remains unadjusted. The two upconverted UV copies of the NOPA are then recombined with a delay τ and interfered to produce a single shot measurement of the NOPA. One interferogram is taken to find τ after being set to an optimal value, usually around 1 ps; every subsequent frame is a complete real-time pulse characterization.

The deformable mirror was optimized in two ways. First, the system of 19 channels can be optimized by hand to produce the desired chirp. Because the ZAP-SPIDER analysis produces real-time sonogram results, the chirp can be easily tweaked visually by a system of 19 voltage dials with the sonograms as feedback. Though this sounds like a large system to optimize, in practice the landscape is relatively smooth, with little coupling between channels. Two rotations of tuning each channel voltage was generally sufficient to compress the NOPA output from chirped to near transform limited (Figure 3.7). Optimization was performed in less than 30 seconds.

Secondly, the deformable mirror was optimized using a genetic algorithm.[17] The 19 voltage channels are conveniently 8-bit integers. They functioned as the adjustable parameters. The genetic algorithm was constrained by a flat spectral phase with no

higher order dispersion. Every combination of settings resulted in conversion on a result very similar to Figure 7b, further indicating that the shaping landscape was very smooth and simple. No improvement over the hand-optimized case was found, and genetic optimization running time was on par with the manual case.

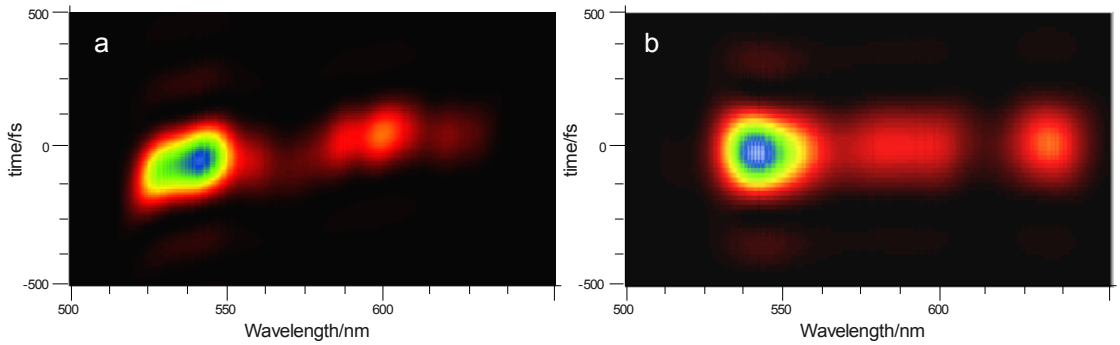

Figure 25: Comparison of (a) negatively chirped NOPA output without deformable mirror compression and (b) near transform limited NOPA after deformable mirror compression.

3.3.3 Flowing sample

The use of a high power electronic excitation in transient spectroscopy will often produce a long-lived response in the system. This necessitates a new sample volume for each laser shot in order to avoid measuring the photobleaching rate or thermally driven processes as well as any other dynamics of interest.[18,19] The can be done using a flowing sample volume, which was achieved using two configurations, each with their own merits. Strong photobleaching was observed without a flowing sample down to 1% molecular excitation (ΔmOD < 30) with both delayed and incomplete recovery over several minutes, further indicating the necessity of a refreshed sample after each UV excitation.

Initially, a wire-guided jet was used to the specifications given by Bradforth et al.[20] A wire-guided jet provides a flowing fluid film suspended between the two sides of a bent wire inserted into a narrow, crimped flow tube. The thickness of the film is dictated by the wire thickness, the wire separation, the initial aperture thickness, and the

vertical extent of the film. Our system used a 250 μm wire with a 200 μm crimped aperture, a wire separation of 1 cm, and a sample length of approximately 5 cm. This was verified by optical density of a sample solution to produce a 200 μm width film that varied little in thickness from top to bottom. Physical contact of the wire bottom with a

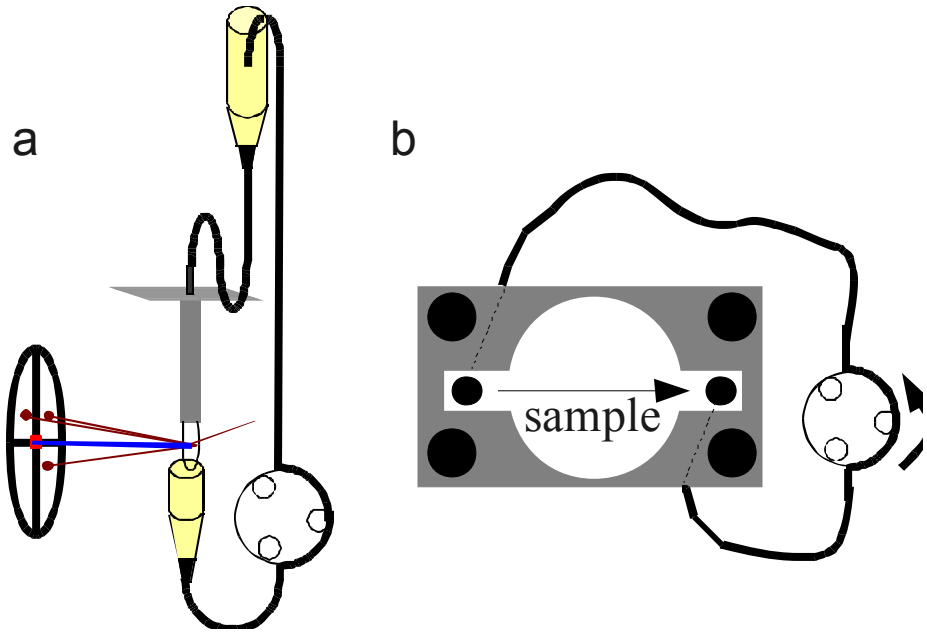

Figure 26: Diagram of the wire-guided jet and flowing cell used for transient experiments. (a) A thin wire is bent and inserted into a small metal tube, forming the two anchors for a downward-flowing fluid. The solution is suspended above the wire in a reservoir and is gravity-fed only. Solution is collected by a receptacle touching the bottom of the wire for smooth flow. A peristaltic pump regenerates the reservoir. (b) Two CaF windows are sandwiched in a metal frame with inlet and outlet ports.

receptacle cup ensures smooth flow from the wire-suspended film into a pump return, which regenerates a sample reservoir above the wire. Varying the reservoir height allows the fluid flow rate to be adjusted such that the sample volume is completely refreshed for every laser shot. The reservoir height was generally set to achieve a flow rate of 25 cm/s, or 250 μm/ms. With a measured IR spot size of 250 μm, this corresponds to a complete refresh of the sample volume at 1kHz, sufficient to our laser repetition rate. A refreshed sample volume was measured by monitoring the pump probe bleach of a flowing sample.

No bleach was observed. Although a peristaltic pump is used to regenerate the sample reservoir from the collection volume, the wire-guided sample is not pumped, and instead is only gravity fed. This helps reduce pumping noise and create a more stable film. The film stability was measured interferometrically using a helium-neon laser at 632 nm to be excellent, with less than 60 nm root-mean-square deviation. Because the film is a suspension between two wires, the film thickness varies as a function of distance from each wire, forming an inward-curving surface both in front and back, much like a concave lens. Proper horizontal and depth positioning of the sample in the focus of the beam-crossing ensured little to no lensing occurred. This left the vertical dimension free to adjust, allowing for the smoothest film portion to be sampled experimentally.

Though the film formed by a wire-guided jet provided excellent stability and a windowless sample, evaporation of highly volatile solvents proved challenging. Coupled with condition-sensitive problems initiating stable film formation, the wire-guided jet design was replaced by a commercial flowing cell. The cell consisted of a 100 μm teflon spacer sandwiched between two 2 mm windows. Inlet and outlet flow was connected to a peristaltic pump. Unlike the gravity-driven wire-guided jet, which provided a smooth flow over time, the flow in the commercial cell is pulsed due to the peristaltic pumping cycle. Because the sample volume was consistently bounded by the windows, however, sample thickness did not vary with pumping. It was therefore not necessary to smooth the flow, but simply ensure a refreshed sample was present for every laser shot. This was accomplished using a sufficiently high flow rate. The sample flow rate was estimated to be greater than 30 cm/s using the cell parameters and measured displacement volume for a given time. Complete sample refresh was confirmed experimentally by monitoring the pump-probe bleach with a flowing sample. No photobleaching was observed. In both the wire-guided jet and flowing cell cases, non-linear pumping effects such as film instability in the wire-guided jet due to absorption of the pump and white light generation in the flowing cell windows due to non-linear self-focusing of the pump before any photobleaching appeared.

3.3.4 Transient 2DIR

Transient 2DIR spectra can be taken simply by introducing an additional excitation pulse to perturb the system from equilibrium.[21] We have applied both visible and ultraviolet excitation using this novel method. The pump is not phase matched with the 2DIR experiment, meaning there is no condition dictating directionality in the application. A single lens focuses the pump to match the size at the sample with the IR sizes, and the pump is introduced with as little angular deviation from the IR as possible to maximize the length of spatial overlap. Visible and UV excitations often induce longer term fluctuations in the sample, requiring much more than 1 ms to equilibrate back to the initial state. Thus, a flowing sample is implemented to refresh the actual sample volume at each laser shot. This was done using first a gravity flow, windowless jet design, and later using a commercially available flow cell.

Two types of transient experiments have been explored. The first, pump-probe 2DIR (PP-2DIR, Fig. 4b) is analogous to a traditional pump-probe technique, where the excitation is placed temporally before the 2DIR pulse sequence. The result is a pump-probe type experiment where the probe is 2DIR.[22-26] This extends the benefits of 2DIR spectroscopy to non-equilibrium processes, allowing their correlation functions to be similarly mapped. Because the Fourier transform method is used, the excitation cannot approach $\tau = 0$ too closely due to the necessity of scanning the t_1 delay. This limits the types of ultrafast dynamics that can be observed to in practice those that occur on a greater than 5 ps timescale. The second method of transient 2DIR, triggered-exchange 2DIR (TE-2DIR, Fig. 4b) does not have an analogue in more traditional pump-probe spectroscopy. Here the excitation is placed between the initial 2DIR excitation by k_1/k_2 and the subsequent initiation of signal by k_3, during the t_2 waiting time. Continuing the analogy from equilibrium 2DIR, the initial two fields E_1 and E_2 label a vibrational population. During t_2, that population would evolve under equilibrium conditions; in TE-2DIR, the equilibrium populations are transferred to non-equilibrium populations that evolve along the excited-state potential. The third field interaction E_3 then probes not the equilibrium molecular state that has evolved, but instead the non-equilibrium product.

Thus, a TE-2DIR spectrum correlates initial reactant vibrations to resulting products vibrations.[21] Currently there is no other direct method to obtain this type of information —it can only be inferred, sometimes incorrectly.

Traditionally pump-probe experiments are performed such that the equilibrium spectrum is taken in concert with the transient spectrum. This allows any slow fluctuations of the laser to be removed and helps alleviate shot-to-shot variations. This can be accomplished by mechanically chopping the excitation pulse, typically at half the repetition rate of the laser, resulting is a series of spectra where each odd numbered spectrum is of the transient photoproduct, while each even numbered spectrum is of the equilibrium species. This can be integrated over many laser shots to improve signal to noise, and over a series of time points, to produce an equilibrium (unpumped) and transient (pumped) spectrum pair for each delay τ between the pump and the probe. In order to highlight transient features in the spectrum relative to the large probe pulse background, the difference is taken, which results in a spectrum containing two types of peaks. Negative-going peaks indicate a bleach of equilibrium state molecules that are depleted by photoexcitation, while positive-going peaks indicate a transient feature of a non-equilibrium product of the photoreaction.

To extend this to FT-2DIR spectra, two separate scans of t_1 must be taken to generate two sets of spectra, pumped and unpumped. This reintroduces the problem of laser drift over the time between taking the two spectra, as they are no longer temporally short. Instead, the t_1 scans are taken simultaneously but interleaved. That is, the pump is again mechanically chopped at half the repetition rate of the laser, but now instead of collecting a complete pumped or unpumped spectrum, a single t_1 timepoint of the 2D spectrum is taken. The result is a series of spectra where every odd member is a pumped spectrum at a given t_1 and every even member is an unpumped spectrum at a slightly shifted t_1 (Fig. 10). Because the frequency axis is built via interpolation, however, the result is two complete set of spectra, pump on and pump off, at uniform times. These two sets of interleaved spectra are deinterlaced in analysis and treated separately, yielding an unpumped spectrum and a pumped spectrum that are subtracted to give a transient difference spectrum.[27] This is then extended to multiple t_2 waiting times similarly to

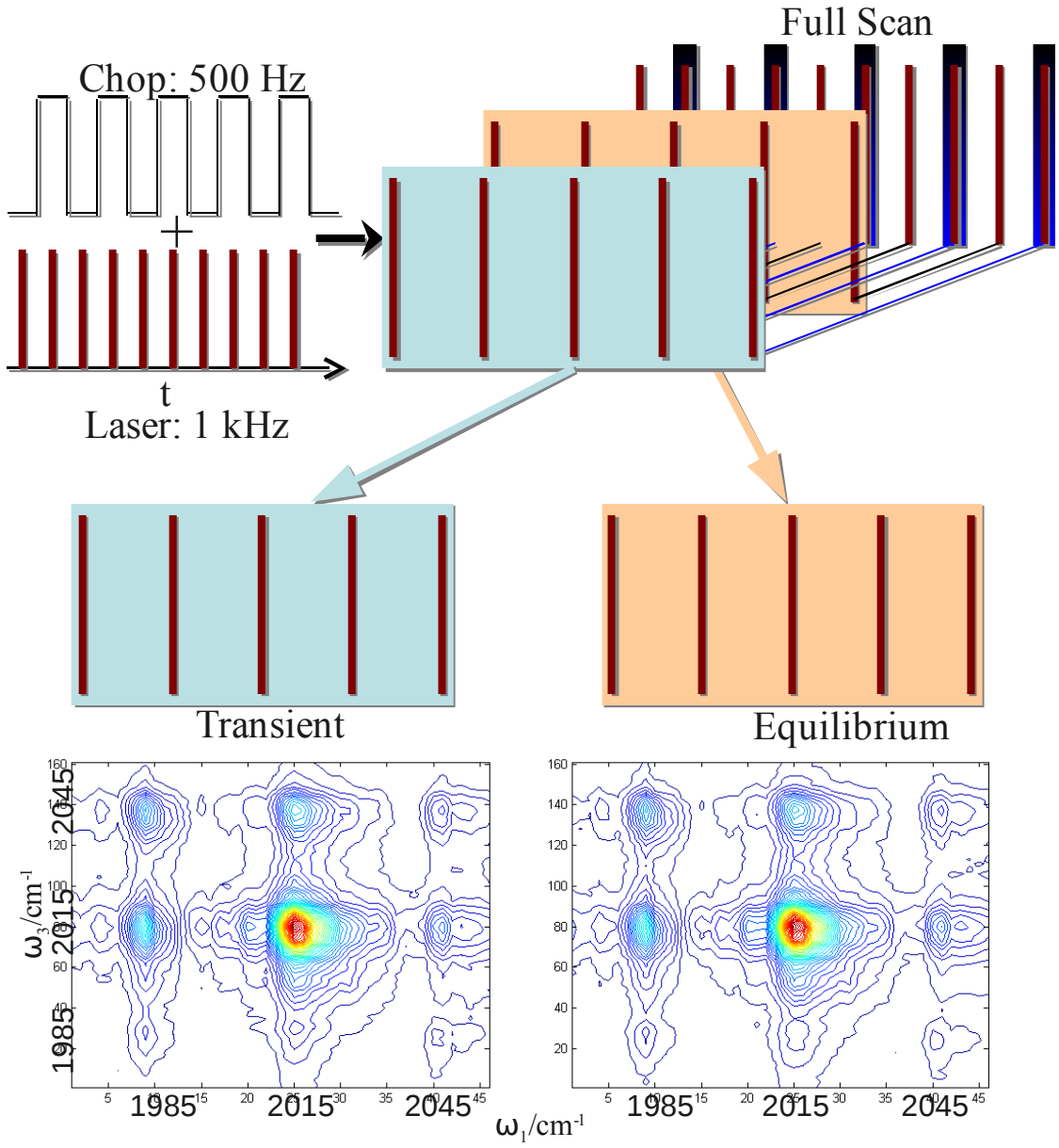

Figure 27: The excitation field is chopped at half the laser repetition rate, resulting is an interleave of pumped and unpumped shots. A 2DIR spectrum is composed of a series of these shots. The two sets are deinterlaced and Fourier transformed separately, resulting in two 2DIR spectra: one with the pump on and one with the pump off. Transient features are often small and swamped by the larger equilibrium features. Thus the difference is often taken between the two spectra, resulting in a spectrum with negative-going bleaches that denote a removal of ground state molecules and positive-going transients that denote a non-equilibrium species.

equilibrium 2DIR spectra.

This novel method of transient 2DIR stands in contrast to previous double resonance transient 2DIR experiments. The primary advantage of the Fourier transform method lies in the accessibility of shorter delay times within the 2DIR pulse sequence. Double resonance experiments that use an etalon cannot access dynamics earlier than ~2 ps due to the long tail of the first infrared pulse. The waiting time resolution of the Fourier transform method used here, however, is limited only by the infrared temporal width. A pulse width of 100 fs gives us access to dynamics such as fast IVR that are otherwise impossible to resolve in the hybrid time-frequency method employed by the Hamm group.

The result is a four dimensional data set dependent on all three 2DIR parameters, ω_1, ω_3, and t_2, as well as the pump probe delay τ as measured from the pump to the second IR interaction with k_2. Because of the use of scanning in the equilibrium 2DIR experiment, an exact pump probe delay analogous to the one dimensional case is difficult to assign; does the non-equilibrium state evolve from the 2DIR experiment beginning at the first application of k_1, or later? In fact the 2DIR pulse sequence is always of finite temporal width, meaning some degree of transient evolution will be bound up in the various 2DIR delays. Particularly, this adds additional dynamics being monitored to the waiting time beyond those present in the equilibrium case. Both equilibrium decays and non-equilibrium evolution will be present.

References

1. Nee, M., Baiz, C., Anna, J., McCanne, R. & Kubarych, K. Multilevel vibrational coherence transfer and wavepacket dynamics probed with multidimensional IR spectroscopy. *JOURNAL OF CHEMICAL PHYSICS* **129**, (2008).
2. Nee, M.J., McCanne, R., Kubarych, K.J. & Joffre, M. Two-dimensional infrared spectroscopy detected by chirped pulse upconversion. *Optics Letters* **32**, 713-5 (2007).
3. Cerullo, G. & De Silvestri, S. Ultrafast optical parametric amplifiers. *REVIEW OF SCIENTIFIC INSTRUMENTS* **74**, 1-18 (2003).
4. Kaindl, R.A. et al. Generation, shaping, and characterization of intense femtosecond pulses tunable from 3 to 20 μm. *J. Opt. Soc. Am. B* **17**, 2086-2094 (2000).
5. Cervetto, V., Helbing, J., Bredenbeck, J. & Hamm, P. Double-resonance versus pulsed Fourier transform two-dimensional infrared spectroscopy: An experimental and theoretical comparison. *Journal of Chemical Physics* **121**, 5935-5942 (2004).
6. Anna, J.M., Nee, M.J., Baiz, C.R., McCanne, R. & Kubarych, K.J. Measuring absorptive two-dimensional infrared spectra using chirped-pulse upconversion detection. *J. Opt. Soc. Am. B* **27**, 382-393 (2010).
7. Jones, K.C., Ganim, Z. & Tokmakoff, A. Heterodyne-Detected Dispersed Vibrational Echo Spectroscopy. *Journal of Physical Chemistry A* **113**, 14060-14066 (2009).
8. LIU, H., YAO, J. & PURI, A. 2ND AND 3RD HARMONIC-GENERATION IN BBO BY FEMTOSECOND TI SAPPHIRE LASER-PULSES. *OPTICS COMMUNICATIONS* **109**, 139-144 (1994).
9. Shirakawa, A. & Kobayashi, T. Noncollinearly phase-matched femtosecond optical parametric amplification with a 2000 cm[sup −1] bandwidth. *Appl. Phys. Lett.* **72**, 147 (1998).
10. Demirdoven, N., Khalil, M., Golonzka, O. & Tokmakoff, A. Dispersion compensation with optical materials for compression of intense sub-100-fs mid-infrared pulses. *Optics Letters* **27**, 433-5 (2002).
11. Fecko, C.J., Loparo, J.J. & Tokmakoff, A. Generation of 45 femtosecond pulses at 3 mu m with a KNbO3 optical parametric amplifier. *Optics Communications* **241**, 521-528 (2004).
12. Fuji, T. & Suzuki, T. Generation of sub-two-cycle mid-infrared pulses by four-wave mixing through filamentation in air. *Optics Letters* **32**, 3330-3332 (2007).
13. Nisoli, M., DeSilvestri, S. & Svelto, O. Generation of high energy 10 fs pulses by a new pulse compression technique. *Applied Physics Letters* **68**, 2793-2795 (1996).
14. Spanner, M. et al. Tunable optimal compression of ultrabroadband pulses by cross-phase modulation. *Optics Letters* **28**, 749-51 (2003).
15. Kobayashi, T. & Baltuska, A. Sub-5 fs pulse generation from a noncollinear optical parametric amplifier. *MEASUREMENT SCIENCE & TECHNOLOGY* **13**, 1671-1682 (2002).
16. Baum, P. & Riedle, E. Design and calibration of zero-additional-phase SPIDER. *JOURNAL OF THE OPTICAL SOCIETY OF AMERICA B-OPTICAL PHYSICS* **22**, 1875-1883 (2005).
17. Nemoto, K., Nayuki, T., Fujii, T., Goto, N. & Kanai, Y. Optimum control of the laser beam intensity profile with a deformable mirror. *APPLIED OPTICS* **36**, 7689-7695 (1997).
18. Bopp, M.A., Jia, Y., Li, L., Cogdell, R.J. & Hochstrasser, R.M. Fluorescence and photobleaching dynamics of single light-harvesting complexes. *Proc Natl Acad Sci U S A* **94**, 10630-5 (1997).
19. Jiao, G.S. et al. Syntheses, photophysical properties, and application of through-bond energy-transfer cassettes for biotechnology. *Chemistry* **12**, 7816-26 (2006).
20. Tauber, M.J., Mathies, R.A., Chen, X.Y. & Bradforth, S.E. Flowing liquid sample jet for resonance Raman and ultrafast optical spectroscopy. *Review of Scientific Instruments* **74**,

4958-4960 (2003).
21. Bredenbeck, J., Helbing, J., Kolano, C. & Hamm, P. Ultrafast 2D-IR Spectroscopy of transient species. *Chemphyschem* **8**, 1747-1756 (2007).
22. Hamm, P., Ohline, S.M. & Zinth, W. Vibrational cooling after ultrafast photoisomerization of azobenzene measured by femtosecond infrared spectroscopy. *Journal of Chemical Physics* **106**, 519-529 (1997).
23. Cervetto, V., Hamm, P. & Helbing, J. Transient 2D-IR spectroscopy of thiopeptide isomerization. *Journal of Physical Chemistry B* **112**, 8398-8405 (2008).
24. Bredenbeck, J., Helbing, J. & Hamm, P. Transient two-dimensional infrared spectroscopy: Exploring the polarization dependence. *Journal of Chemical Physics* **121**, 5943-5957 (2004).
25. Bredenbeck, J., Helbing, J. & Hamm, P. Labeling vibrations by light: Ultrafast transient 2D-IR spectroscopy tracks vibrational modes during photoinduced charge transfer. *Journal of the American Chemical Society* **126**, 990-991 (2004).
26. Bredenbeck, J. & Hamm, P. Transient 2D-IR spectroscopy: Towards a molecular movie. *Chimia* **61**, 45-46 (2007).
27. Baiz, C.R., Nee, M.J., McCanne, R. & Kubarych, K.J. Ultrafast nonequilibrium Fourier-transform two-dimensional infrared spectroscopy. *Opt. Lett.* **33**, 2533-2535 (2008).

Chapter 4

A Transient 2DIR Examination of Tungsten Hexacarbonyl

4.1: Design and testing using dimanganese decacarbonyl

Many experimental challenges exist in applying transient 2DIR to large molecules. Molecular response must be both sufficiently diffuse to ensure sampling of the dynamics of interest, as well as sufficiently resolved as to allow a spectroscopic method of reaction monitoring. Together with the inherently lower signal amplitudes of non-linear measurements,[1] multidimensional transient measurements on larger molecules are only now being attempted.[2] In order to understand and interpret the results of such experiments, a complete understanding of transient 2DIR spectra is first necessary. Thus applying transient 2DIR to first a set of smaller systems, which are more easily modeled, provides an excellent avenue to explore transient 2DIR effects.

Initially transient 2DIR experimental procedure was applied to our perennial test molecule, dimanganese decacarbonyl ($Mn_2(CO)_{10}$, DMDC).[3,4] The metal carbonyl series is of great interest as catalysts in directed hydrocarbon reactions, as well as being important donors in carbonyl addition reactions.[5-7] Additionally, transient 2DIR can aid in understanding the early time molecular motions that occur on CO removal, in order to better understand and utilize metal carbonyl catalysis. DMDC has proven to be an excellent beacon in constructing and testing both our 2DIR and transient 2DIR experimental setups. Carbonyls provide one of the highest IR oscillator strengths, making metal carbonyls extremely good absorbers of infrared.[8] In turn, this provides a strong and clear signal for building and tuning the experimental 2DIR. In addition to

that, many metal carbonyls undergo high quantum yield photoreactions at easily accessible frequencies. Unfortunately, DMDC provides a less tractable transient 2DIR spectrum. Clear indications of transient effects can be observed, making a transient signal easy to isolate, yet the actual transient features for one excitation nearly overlap, proving difficult to analyze.[9-11]

DMDC undergoes two important photoreactions that have been previously reported, corresponding to two distinct absorption features in the UV absorption spectrum.[9,10] UV-pump, IR probe experiments have shown that when excited near 400 nm, DMDC undergoes metal-metal cleavage, producing two monomer radicals. Additional experiments then demonstrated that when excited near 300 nm, DMDC undergoes metal-carbon cleavage, releasing a CO into solution. The branching ratio is not exclusive to one product by tuning the excitation frequency, but previous studies have

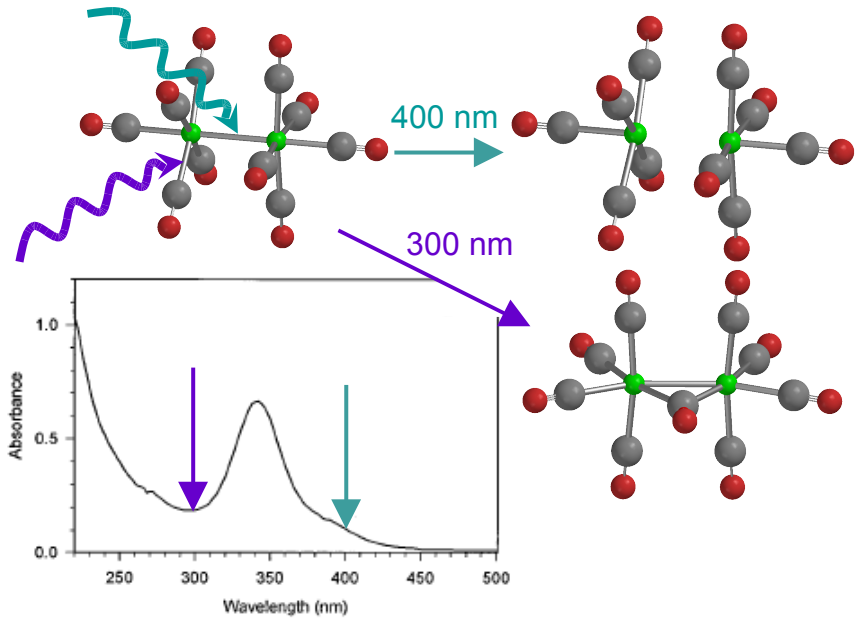

Figure 28: UV/Vis reaction pathway for the dissociation of DMDC. Excitation near 400 nm cleaves the manganese-manganese bond, resulting in two identical radical monomers, while excitation near 300 nm causes cleavage of a metal carbon bond, resulting in a bridged metal carbonyl and a free CO.

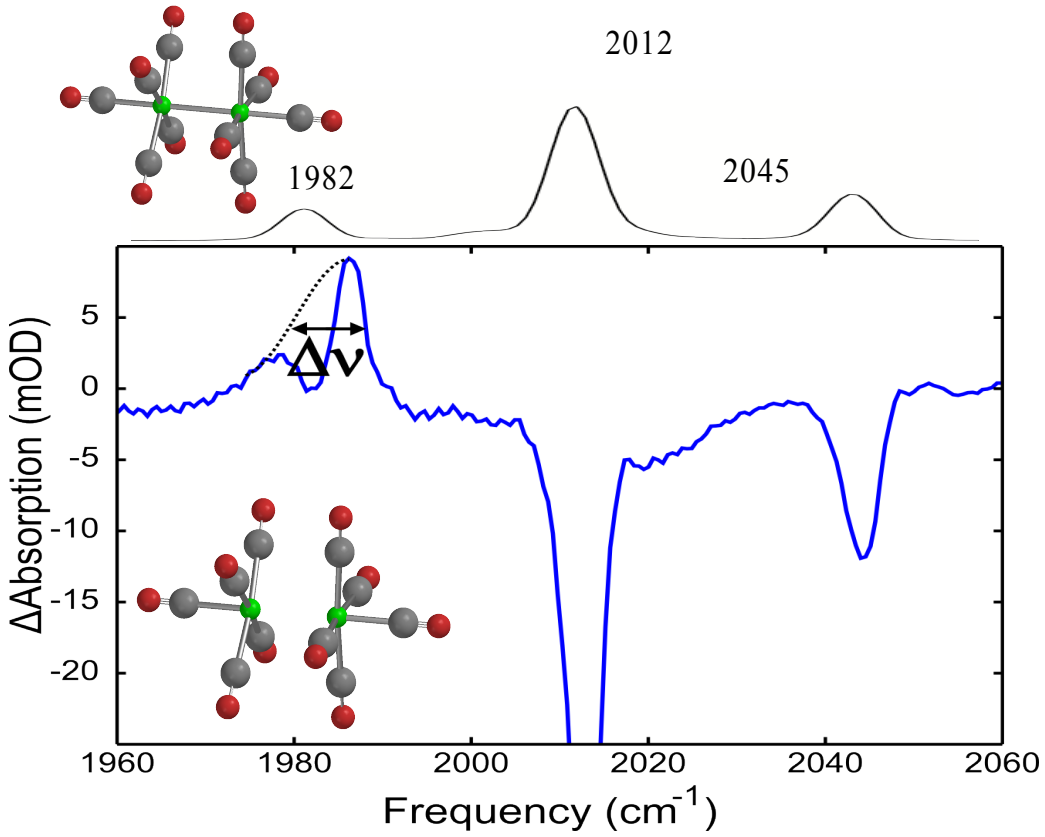

Figure 29: Excitation at lower energies produces overlapped transient spectra. The DMDC parent absorption at 1982 cm^{-1} results in a bleach that obscures the pentacarbonyl product absorption at almost the same frequency. This necessitates additional fitting analysis to produce the product peak width as a function of pump-probe delay.

found a greater than 9:1 ratio of monomer product formation for excitations wavelengths longer than 350 nm and a less than 3:1 ratio of free CO product formation for excitations wavelengths shorter 300 nm.

Both reactions result in bands that overlap the equilibrium absorption bands of DMDC as shown in pump probe spectra. In the metal cleavage monomers, one new band is reported at 1982 cm^{-1}, overlapping exactly with the low frequency 1982 cm^{-1} band of the parent DMDC. In the carbonyl cleavage $Mn_2(CO)_9$ product, several new bands are reported, partially overlapping both the 1982 and 2012 cm^{-1} bands of DMDC. Additional bands are reported at lower frequencies, as well, with one near 1700 cm^{-1} attributed to a

bridged carbonyl shared by both metal centers. These combinations of bands results in transient 2DIR spectra that contain many overlapping peaks, which hinders analysis of transient photoproduct behavior. The isolated bridging peak would be easier to analyze, but is difficult to produce experimentally using the current pulse bandwidth and tuning. Advances in broader IR pulses will soon make this region more easily accessible, making CO bridge formation a more viable avenue of study.

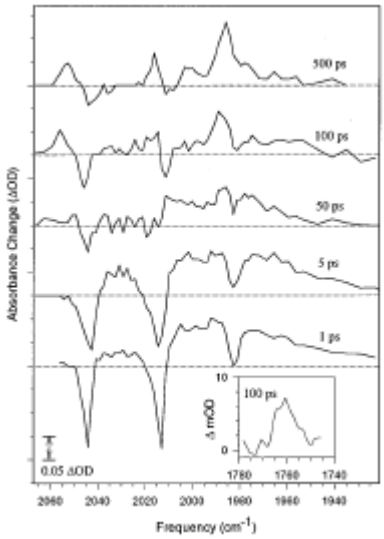

Figure 30: Higher energy excitation preferentially cleaves a carbonyl. The branching ratio is lower than in the 400 nm photoreaction, resulting in several transients, which overlap both the parent bleaches and each other at early times.[9]

Despite the overlap of transient bands, they can nevertheless be analyzed by careful extraction of the two components. Both the triggered-exchange (TE-2DIR) and the pump-probe (PP-2DIR) methods of transient 2DIR were applied. The signal level of TE-2DIR was found to be weak, a result of scrambling of reactant vibrational modes by excitation through the transition state. TE-2DIR spectra can be understood in the following way: transient peaks arise due to new frequencies detected after stimulation of emission by k_3 whose initially labeled frequencies belonged to the equilibrium parent molecule. Thus, a transient peak correlates excitation frequency of the *parent* with detection frequency of the *product*.[12] In the TE-2DIR spectrum of DMDC (Fig. 2a),

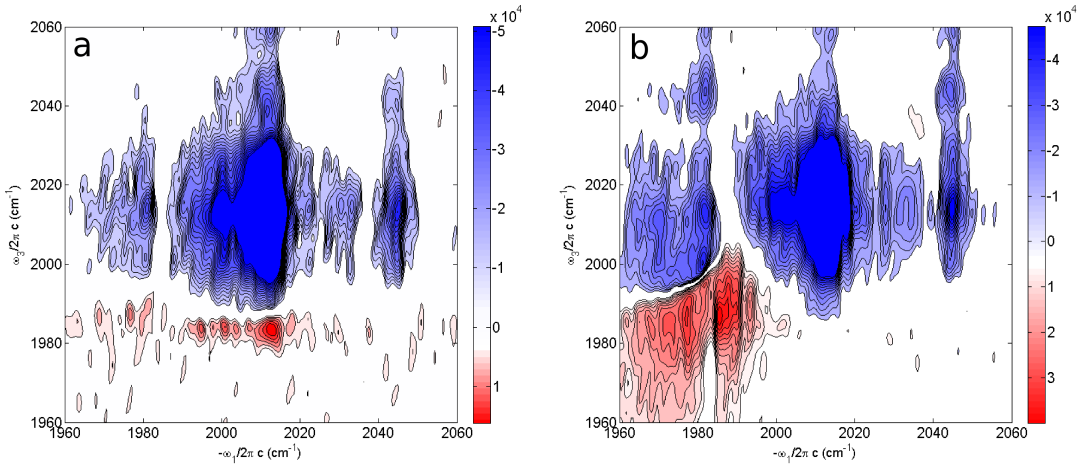

Figure 31: Transient 2DIR of DMDC excited by 400 nm light.
(a) TE-2DIR of DMDC. The transient mode at 1982 cm^{-1} contains contributions primarily from the parent E modes at 2012 cm^{-1}, but with a small amount of the parent A_2 mode at 1982 cm^{-1} as well. (b) PP-2DIR of DMDC. Lineshape analysis is complicated by overlap of the parent decacarbonyl and product pentacarbonyl bands.

though the majority of the pentacarbonyl product mode at 1982 cm^{-1} comes from a contribution by the parent E modes, indicated by the positive band at ω_1 = 2012 cm^{-1}, ω_3 = 1982 cm^{-1}, a small portion is also due to the low frequency A_2 parent mode, indicated by the band at ω_1 = 1982 cm^{-1}, ω_3 = 1982 cm^{-1}.[11] Some mixing of vibrational modes during the reaction must be occurring for multiple parents modes to contribute to a single product mode.

A series of PP-2DIR spectra were also taken mapping out the t_2 and τ parameter space as shown in Figure 3.[4] By analyzing the behavior of the transient peak amplitude as a function of waiting time and pump-probe delay, and carefully removing the bleach behavior, it was shown that the lifetime of the vibrational relaxation of the photoproduct band depended on the pump-probe delay time. This was interpreted as a temperature dependent relaxation of the photoproduct. The excitation at 400 nm is in excess of the metal-metal bond energy by over 10,000 cm^{-1}, which causes initial broadening of the product bands. One-dimensional pump-probe experiments have shown a distinct narrowing of the band as a function of pump-probe delay, corresponding to a decrease in vibrationally populated excited states as the initially hot photoproduct cools. Two-

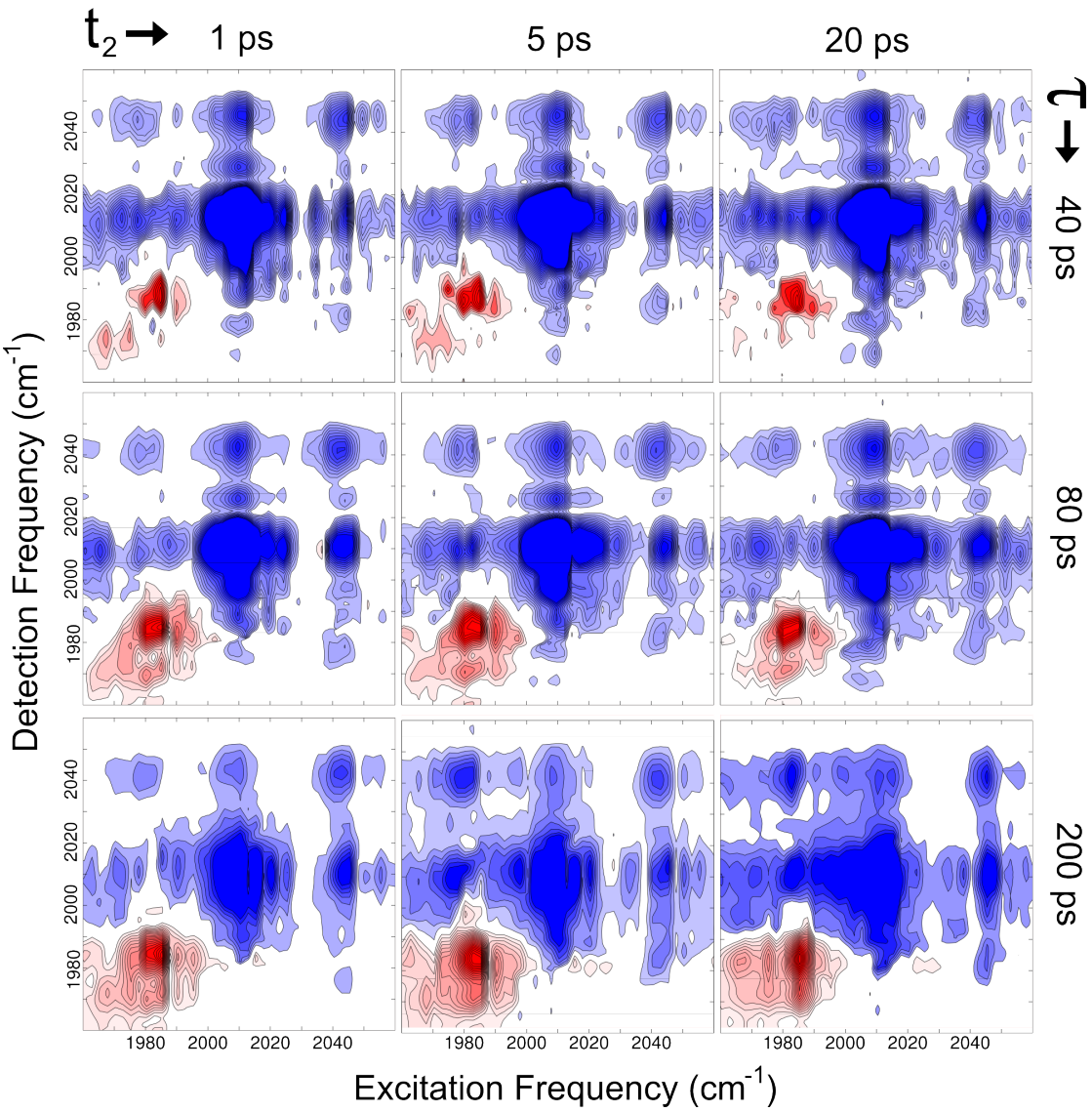

Figure 32: A scan of t_2 and τ produces a large set of PP-2DIR spectra. The waiting time increases from left to right and the pump-probe delay increases from top to bottom.

dimensional experiments here show the same behavior as a function of τ, with the added ability to monitor the vibrational dynamics during t_2.

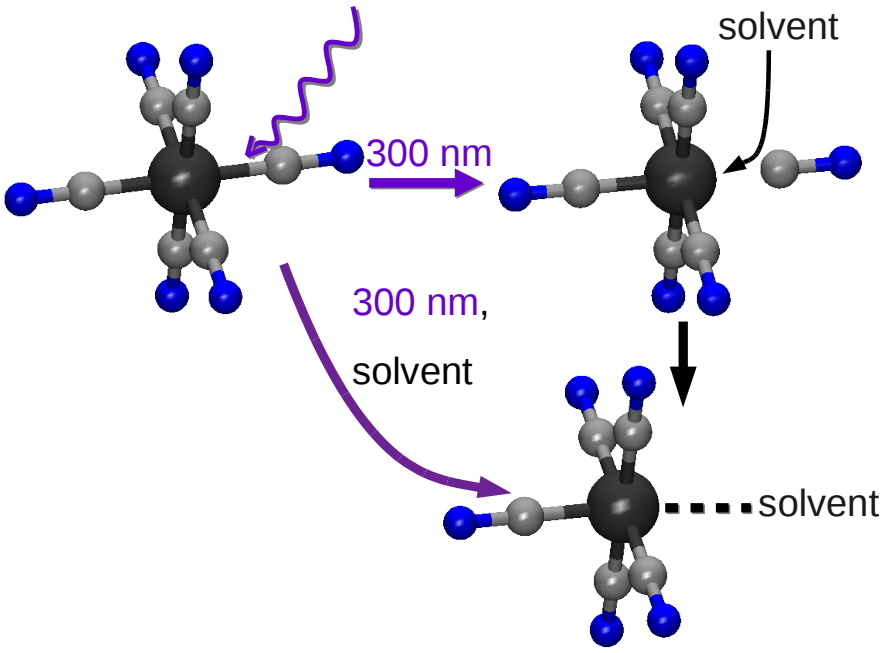

Figure 33: Excitation of tungsten hexacarbonyl in the near UV results in metal-carbon bond cleavage, producing the pentacarbonyl and free CO. Solvent coordination happens quickly, perhaps in a single coordinated step.

4.2: Transient 2DIR of tungsten hexacarbonyl

4.2.1 Experimental concerns

In order to better isolate the photoproduct vibrations from the parent spectrum, tungsten hexacarbonyl ($W(CO)_6$) was examined. Previous work on has included equilibrium spectral measurements as well as IR-pump IR-probe and visible-pump IR-probe.[13-19] $W(CO)_6$ has one triply degenerate IR active T_{1u} collective CO mode at 1982 cm^{-1}. Two Raman CO modes are also present at higher frequencies (a 2020 cm^{-1} A_{1g} and a 2120 cm^{-1} E_g), which are important when considering relaxation dynamics. Previous transient IR work has assigned the $\upsilon = 2$, 3, and 4 energies of the IR active mode to be 3949, 5901, and 7834 cm^{-1} (1967, 1952, and 1933 cm^{-1} anharmonic transition energies) in

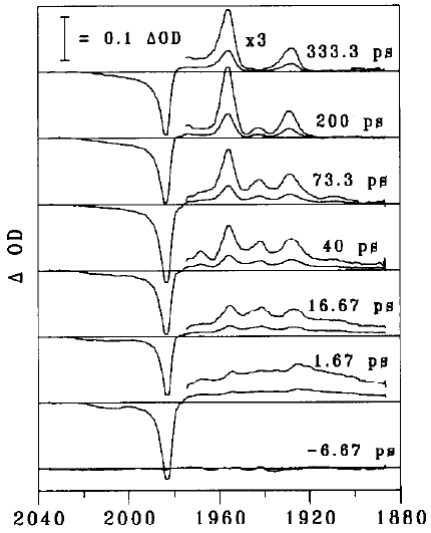

Figure 34: $W(CO)_6$ transients are well separated from the parent bleach. Two long-lived peaks appear to the red of the bleach that decay on a vibration lifetime scale. Two additional peaks appear at intermediate times and have been assigned as the anharmonic transitions of the two previous transitions. An additional peak at 1965 cm^{-1} is unassigned. Transient peaks appear broadened at early time due to excess energy available from the photoexcitation.

n-hexane.[19] Previous transient visible studies of $W(CO)_6$ have shown one primary photoreaction, where a single carbonyl is removed upon excitation near 300 nm, removing the issue of branching ratios from consideration.[18] This excitation is in excess of the metal-carbon bond energy by more than a factor of two, with a bond energy of approximately 16,000 cm^{-1} and an excitation energy in excess of 35,000 cm^{-1}, resulting in a highly energized photoproduct pair. Temperature estimates put the majority of the energy in the metal carbonyl, with an initial temperature just following bond cleavage of nearly 2000 K. More importantly spectroscopically, $W(CO)_6$ presents a single collective carbonyl band at 1982 cm^{-1} while the pentacarbonyl photoproduct spectrum is reported to consist of two bands at 1928 and 1956 cm^{-1} indicative of the two product A_1 and E modes. Additional transient peaks are also seen, with two of them at 1942 and 1908 cm^{-1} attributed to $\upsilon_{1\rightarrow2}$ anharmonic transitions. A third peak is indicated near 1965 cm^{-1}, though never discussed, leading to a further interest in studying the transient system.

This removes the transient dynamics from the ground state bleach region of the spectrum, easing analysis.

The transient 2DIR rephasing and non-rephasing spectra of $W(CO)_6$ were taken in cyclohexane for a range of waiting times from -1 ps to 60 ps and a range of τ from -10 to 150 ps. A τ less than zero corresponds to a triggered exchange experiment where the photoinitiation occurs during the waiting time. A τ greater than zero corresponds to a pump-2DIR probe transient experiment. The range of τ from -1 to 5 ps was avoided to prevent overlap of the 2DIR experiment and the pump. While this presents a valid experimental technique, the resulting experiment is a fully fifth order process and beyond the scope of this project. Separating the transient pump from the 2DIR process allows the results to be treated as the sum of a second order excitation and a third order probe.

4.2.2 $W(CO)_6$ results

The difference spectra were computed to highlight transients at each of the delays, resulting in a matrix of data, represented in Figure 8. A broad bleach dominates at $\omega_1 = \omega_3 = 1982$ cm^{-1}. The parent absorption is broad compared to similar compounds that have been studied, with a peak width of over 10 cm^{-1} even in less interacting solvents such as cyclohexane and n-hexane. This is further enhanced in the 2DIR spectra by excess energy present in the system and by the low contouring used to enhance the transient features.

Four transient diagonal features are visible at early waiting and pump-probe times. These correspond to the four features identified in the 1D pump-probe spectra. Additionally, cross peaks appear selectively between the transient diagonals due to coupling through the initial state of the system following photoexcitation and preceding 2DIR labeling (Figure 9). This is similar to coupling through the ground state that occurs in equilibrium 2DIR. Here, however, the system is left in a vibrationally excited state by

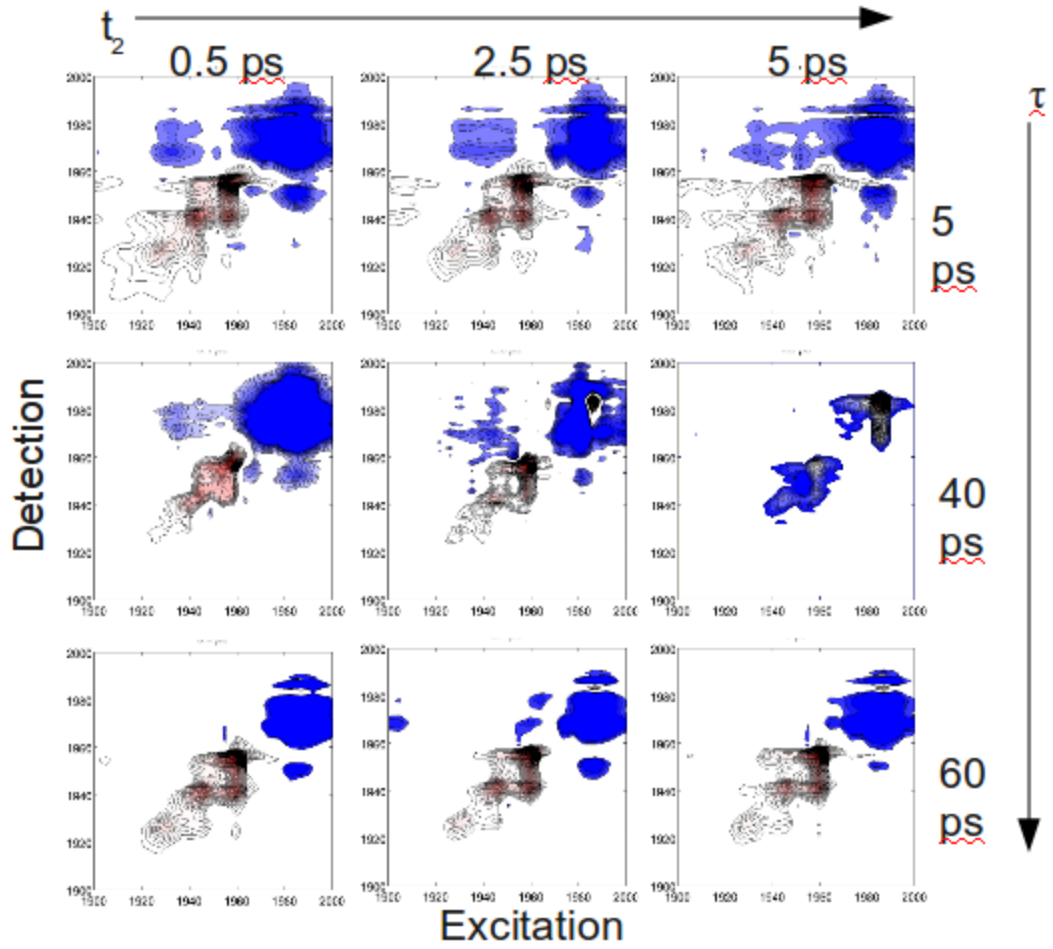

Figure 35: PP-2DIR spectra of $W(CO)_6$ varying waiting time and pump-probe delay. A broad bleach feature is prominent at all times. At early times, transient features appear along the diagonal and off diagonal. They narrow and decay as a function of both delays. The low frequency diagonal at 1908 cm^{-1} disappears almost entirely, as do several transient cross peaks present at early times.

the excess energy deposited by photoexcitation. Excitation at 266 nm imparts an excess 36,000 cm^{-1} of energy into the $W(CO)_6$ reactant, while the metal-carbon bond energy is only 16,000 cm^{-1}. Thus there is 20,000 cm^{-1} of excess energy localized mainly on the pentacarbonyl fragment, which causes excitation of a large number of low frequency modes that couple to the carbonyl transitions, giving rise to the broadening at early times.

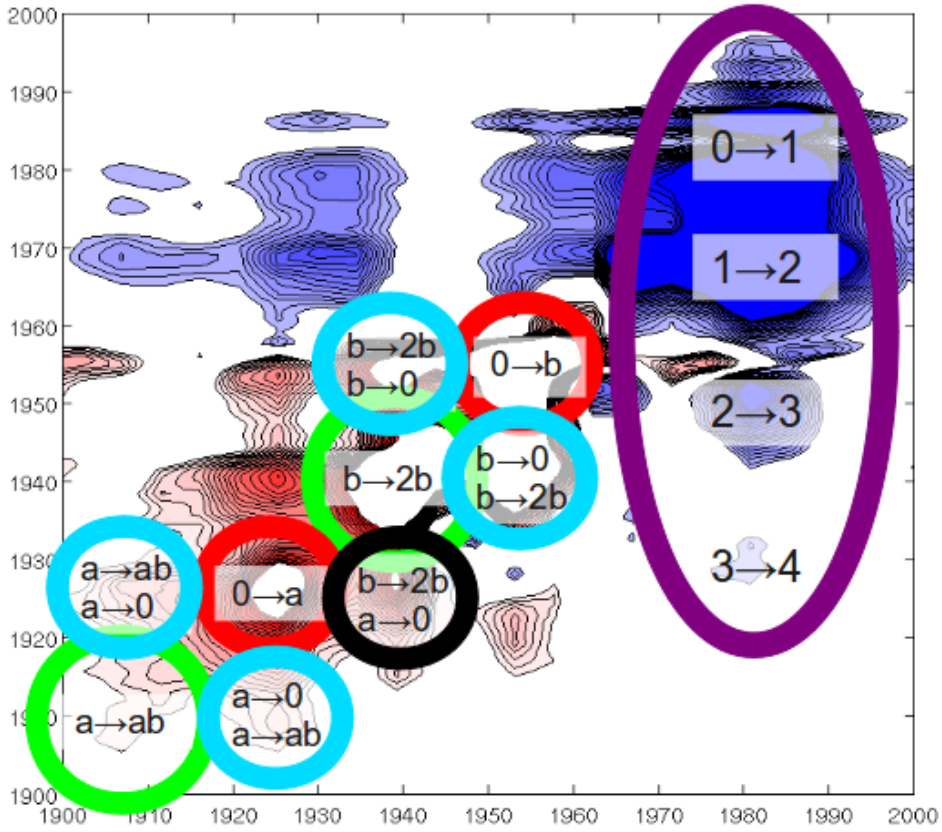

Figure 36: Peak assigments for the transient diagonal and cross peaks. Additional diagonal peaks appear due to a hot photoproduct with a populated first vibrational state. Transitions can then occur to the second excited vibrational manifold, resulting in two diagonal peaks for each band. Cross peaks occur between the first and second manifolds in the same way. An additional cross peak corresponds to labeling at |b>→|2b> but detecting at |a>→|0>. This requires IVR from |b> to |a> during t_2.

Additionally, 20,000 cm^{-1} over five carbonyl transitions corresponds to several quanta of excitation in each. As a result, the system is in a vibrationally hot state following excitation, allowing access to the second manifold directly, and thus the additional 1D transients and 2D diagonals (Figure 9, a→ab and b→2b as marked).

The evolution of the pentacarbonyl product was monitored as a function of waiting time by integration of peak volume (Figure 12). The decay of this volume as a function of time in principle contains all the elements contributing to loss of signal as a

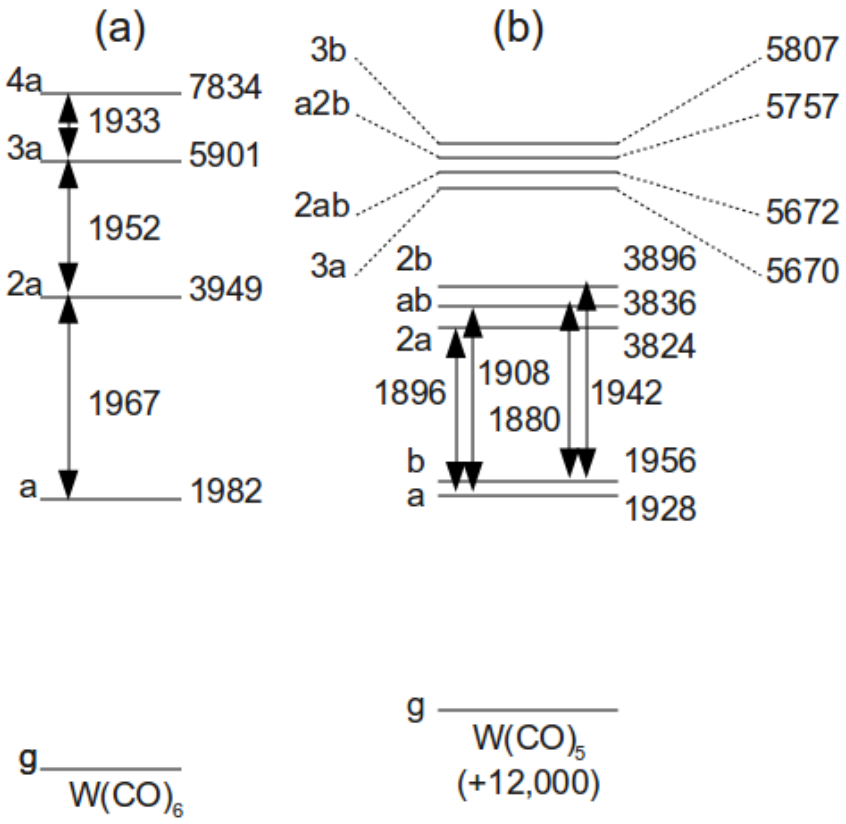

Figure 37: Hexacarbonyl parent and pentacarbonyl product energy levels. (a) the first four manifolds as found experimentally and by DFT calculations of the T_{1u} mode are shown. (b) the first three manifolds of the E and A_1 modes are shown.

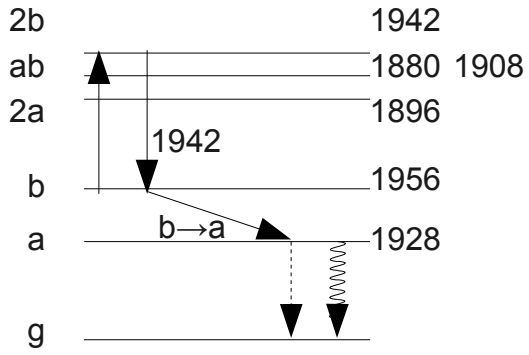

Figure 38: Crosspeak between 1942 and 1928 cm^{-1} requires IVR.

function of vibrational waiting time: IVR, reorientation, and vibrational lifetime. Because of the separation of timescales, however, the middle time of several picoseconds reflects only the reorietational rate.[4] IVR occurs within the first few picoseconds, while the lifetime has been reported to be 160 ps.[18] As such, the 2 to 60 ps range was well fit by a single exponential decay, giving the reorientational rate for each peak at each pump-probe delay. The resulting reorientational rates were plotted as a function of pump-probe delay, which indicated a decrease in rate. The diagonal and off diagonal peaks showed similar rates of decay around 40 ps. The off diagonal peaks, however, showed a larger amplitude decay. The off-diagonal peaks between 1927 and 1944 cm^{-1} correspond to excitation (detection) of $\upsilon_{b\rightarrow 2b}$ and detection (excitation) of $\upsilon_{a\rightarrow 0}$. This requires IVR of b→a (a→b)

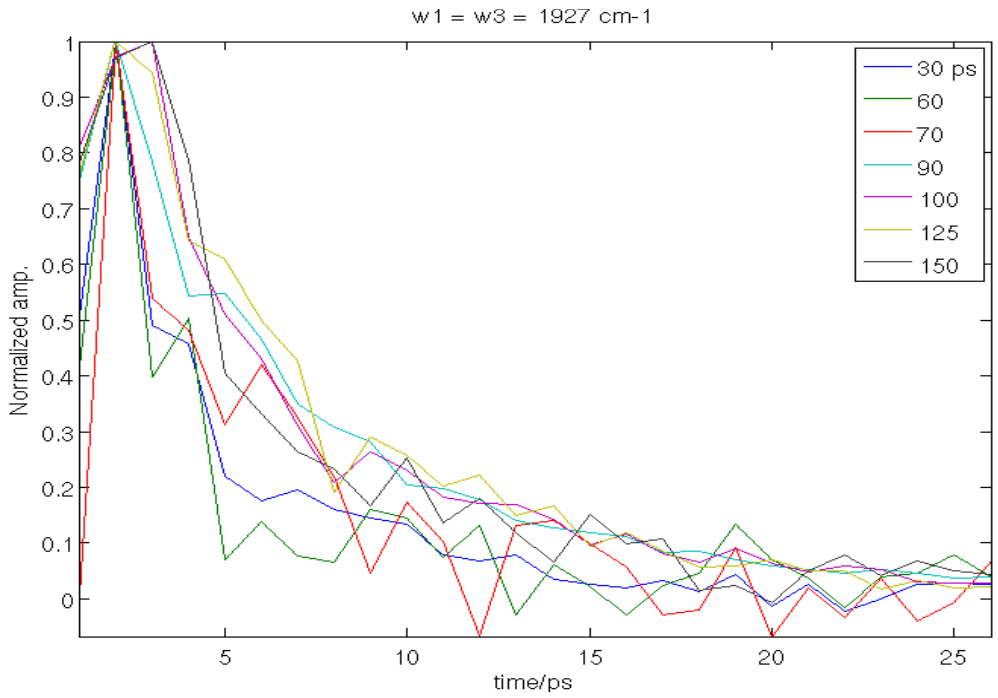

Figure 39: Peak volume as a function of waiting time for $\upsilon_{0\rightarrow a}$ peak (1927 cm^{-1}). IVR occurs in a few picoseconds, while the vibrational lifetime is about 160 ps. The tens of picoseconds decay corresponds to reorientation photoproduct.

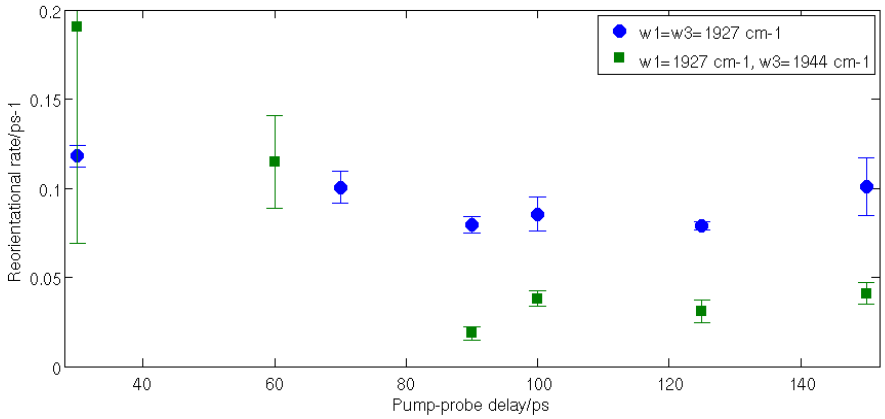

Figure 40: Decrease in reorientational rate with greater pump-probe delay. Though the timescale is similar, the early times are poorly sampled. As a possible result, the diagonal peak shows less than a factor of two decrease, while the off diagonal peak shows a decrease by almost a factor of five.

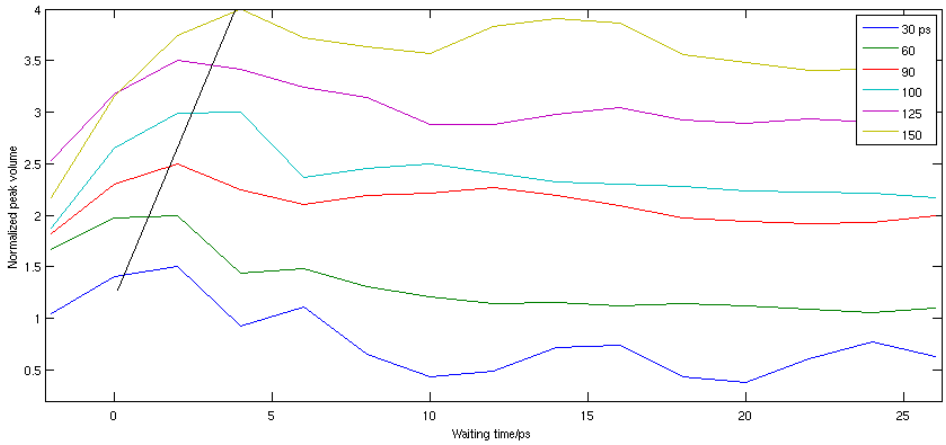

Figure 41: Peak volume as a function of waiting time at early times. A shift in waiting time can be seen for the early maximum, indicated by the vertical line. This corresponds to only a few experimental points, making a rate impossible to extract.

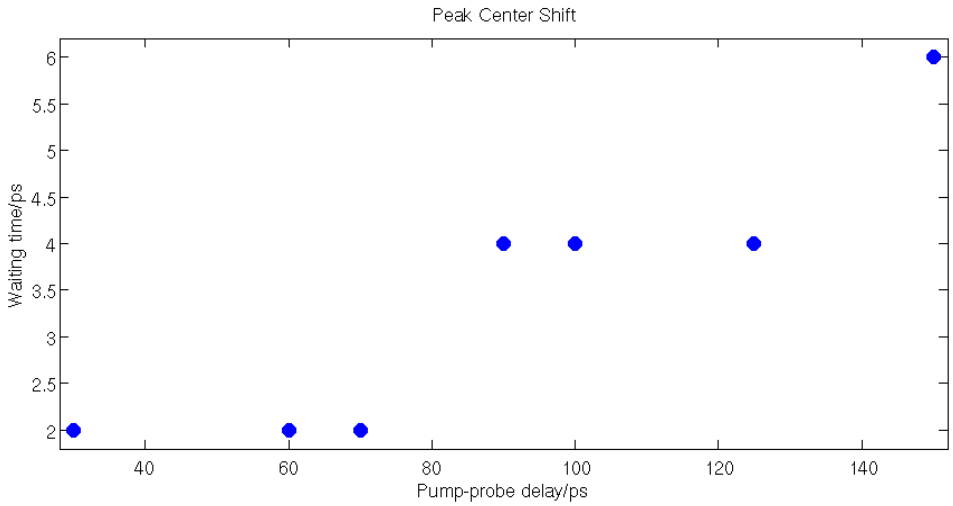

Figure 42: Peak maximum waiting time as a function of pump-probe delay. The waiting time was sampled in 2 ps steps, making the time shift in peak maximum over only two pixels of resolution. Nevertheless, the increase occurs on the timescale of vibrational cooling.

during the waiting time (Figure 11). IVR is in this way most easily considered a population transfer, where here both populations are IR-active. At early pump-probe delays, no growth can be seen in the cross peak amplitudes. As the pump-probe delay is lengthened, a slight shift in the waiting time is observed for the maximum of the cross peak volume. Though this represents only two sampled time points, too small to extract a rate, it can nevertheless be seen that as the pentacarbonyl product cools, the IVR rate is decreasing.

4.2.3 Discussion of transient $W(CO)_6$ spectroscopy and hot photoproducts

The peaks were assigned using the experimental and calculated energy levels of $W(CO)_5$. The two diagonal peaks at 1956 and 1927 cm^{-1} are assigned as the fundamental absorptions of an E and A_1 mode, respectively. The cross peaks between these occur just as in equilibrium spectra, due to a shared initial state. The diagonal peak at 1944 cm^{-1} is assigned as the $\upsilon_{b\rightarrow 2b}$ anharmonic transition. In contrast to previous studies, the diagonal peak at 1908 cm^{-1} is assigned not to the $\upsilon_{a\rightarrow 2a}$ anharmonic transition, but rather the $\upsilon_{a\rightarrow ab}$ transition to the combination band using both our own calculations and those of

Dougherty and Heiweil (Figure 10).[18] The $\upsilon_{a\rightarrow ab}$ anharmonic transition is expected at 1896 cm^{-1}. Crosspeaks with the 1956 and 1944 cm^{-1} peaks at the very edge of the experimental bandwidth hint that this transition occurs where expected. Cross peaks also occur between several of these diagonal peaks. Of particularly note are the cross peaks which require IVR during the waiting time.

The initial excitation of $W(CO)_6$ deposits a large excess energy into the photoproduct, which must then be distributed through the available degrees of freedom. This can occur through IVR, allowed the energy in the pentacarbonyl to equilibrate on a short time scale, and through coupling to the bath. The former is responsible for increased peak volume at early times, while the latter is responsible for peak broadening.[20] $W(CO)_6$ also presents unusual behavior. Even in the absence of photoexcitation multiple anharmonic peaks are observed in the spectrum, even at low IR excitation energies. It seems that ladder climbing is unavoidable for the parent molecule, in stark contrast to other metal carbonyls studied.[18,19] The photoproduct behavior is similar, in that extra spectral features are observed in contrast to studies in previous metal carbonyls. In part this may be due to the higher excess energy available, or it may be due to fewer available mechanisms of equilibration due to fewer degrees of freedom available.

Also unique to this system is the observation of IVR between two photoproduct modes at very high temperatures. This IVR then evolves as the temperature cools. Previous studies show that IVR rate is directly proportional to the liquid phonon population of the matching energy difference between the two IVR modes.[21] The population is given by

$$n_j = \frac{1}{e^{E_j/RT} - 1}. \tag{30}$$

For an energy difference of 28 cm^{-1} between the two modes labeled a and b this suggests a sevenfold increase in IVR rate from room 300 °C to 2000 °C. Compared to previous metal carbonyls with IVR rates around 1-2 ps, IVR would then occur in the hot photoproduct on the order of the experimental resolution, 100-200 fs. Photoproduct cooling occurs within 40 ps, at which point IVR rates should return to values more

representative of room temperatures. Indeed, a shift of the peak maximum with waiting time can be observed in Figures 12 and 13. Finer resolution may find that at early pump-probe delays the IVR still occurs within the experimental resolution of 100 fs. IVR at later pump-probe delays, however, clearly occurs on a slower timescale, more consistent with a cooled product closer to room temperature.

4.3: Conclusions

Transient 2DIR presents valuable tools towards understanding non-equilibrium dynamics by correlating frequency information across two frequency dimensions and through an ultrafast waiting time. This allows for greater understanding of the system as compared to 1D transient spectroscopy. Just as 1D transient spectroscopy contains inherent limitations, however, new complications occurs in transient 2DIR. While the greater information content provides valuable insight into ultrafast IVR and vibrational cooling, much efforts must be expended on isolating and assigning the resulting complex spectra.

The photoreaction of $W(CO)_6$ has been studied, showing similar reorientational times to those predicted by 1D transient spectroscopy. A reorientational time of at most 40 ps is nearly twice as fast as the previously studied $Mn_2(CO)_{10}$. This may be due simply to the tungsten product containing only one monomer to the manganese two monomers. The additional diagonal and cross peaks of the spectrum were assigned, with the peak previous assigned to the a→2a transition by transient absorption spectroscopy instead reassigned to transition to the combination band, a→ab.

Two additional peaks were shown to arise solely from IVR during the waiting time, which slowed with increasing pump-probe delay. This is due to a decrease in the liquid phonon population coupled to the IVR as the product cools. The predicted result is a sevenfold increase in IVR time with cooling, consistent with the shift in crosspeak maximum as a function of waiting time.

References

1. Cervetto, V., Helbing, J., Bredenbeck, J. & Hamm, P. Double-resonance versus pulsed Fourier transform two-dimensional infrared spectroscopy: An experimental and theoretical comparison. *Journal of Chemical Physics* **121**, 5935-5942 (2004).
2. Andresen, E.R. & Hamm, P. Site-Specific Difference 2D-IR Spectroscopy of Bacteriorhodopsin. *The Journal of Physical Chemistry B* **113**, 6520-6527 (2009).
3. Baiz, C.R., McRobbie, P.L., Anna, J.M., Geva, E. & Kubarych, K.J. Two-Dimensional Infrared Spectroscopy of Metal Carbonyls. *Accounts of Chemical Research* **42**, 1395-1404 (2009).
4. Baiz, C.R., McCanne, R., Nee, M.J. & Kubarych, K.J. Orientational Dynamics of Transient Molecules Measured by Nonequilibrium Two-Dimensional Infrared Spectroscopy. *The Journal of Physical Chemistry A* **113**, 8907-8916 (2009).
5. Ito, K., Hara, Y., Mori, S., Kusama, H. & Iwasawa, N. Theoretical Study of the Cycloaddition Reaction of a Tungsten-Containing Carbonyl Ylide. *CHEMISTRY-A EUROPEAN JOURNAL* **15**, 12408-12416 (2009).
6. Cadierno, V. et al. Ruthenium-catalyzed redox isomerization/transfer hydrogenation in organic and aqueous media: A one-pot tandem process for the reduction of allylic alcohols. *GREEN CHEMISTRY* **11**, 1992-2000 (2009).
7. Hebrard, F. & Kalck, P. Cobalt-Catalyzed Hydroformylation of Alkenes: Generation and Recycling of the Carbonyl Species, and Catalytic Cycle. *CHEMICAL REVIEWS* **109**, 4272-4282 (2009).
8. Banno, M., Ohta, K., Yamaguchi, S., Hirai, S. & Tominaga, K. Vibrational Dynamics of Hydrogen-Bonded Complexes in Solutions Studied with Ultrafast Infrared Pump−Probe Spectroscopy. *Accounts of Chemical Research* **42**, 1259-1269 (2009).
9. Owrutsky, J.C. & Baronavski, A.P. Ultrafast infrared study of the ultraviolet photodissociation of Mn2(CO)10. *J. Chem. Phys.* **105**, 9864 (1996).
10. Steinhurst, D., Baronavski, A. & Owrutsky, J. Transient infrared spectroscopy of Mn-2(CO) (10) with 400 nm excitation. *CHEMICAL PHYSICS LETTERS* **361**, 513-519 (2002).
11. Baiz, C.R., Nee, M.J., McCanne, R. & Kubarych, K.J. Ultrafast nonequilibrium Fourier-transform two-dimensional infrared spectroscopy. *Opt. Lett.* **33**, 2533-2535 (2008).
12. Bredenbeck, J., Helbing, J. & Hamm, P. Labeling vibrations by light: Ultrafast transient 2D-IR spectroscopy tracks vibrational modes during photoinduced charge transfer. *Journal of the American Chemical Society* **126**, 990-991 (2004).
13. Lannone, M., Cowen, B.R., Diller, R., Maiti, S. & Hochstrasser, R.M. High-repetition-rate infrared-pump, infrared-probe spectrometer. *Appl Opt* **30**, 5247-9 (1991).
14. Tokmakoff, A., Sauter, B., Kwok, A.S. & Fayer, M.D. Phonon-Induced Scattering between Vibrations and Multiphoton Vibrational up-Pumping in Liquid Solution. *Chemical Physics Letters* **221**, 412-418 (1994).
15. Tokmakoff, A. et al. Vibrational Photon-Echoes in a Liquid and Glass - Room-Temperature to 10-K. *Journal of Chemical Physics* **101**, 1741-1744 (1994).
16. Tokmakoff, A., Kwok, A.S., Urdahl, R.S., Francis, R.S. & Fayer, M.D. Multilevel Vibrational Dephasing and Vibrational Anharmonicity from Infrared Photon-Echo Beats. *Chemical Physics Letters* **234**, 289-295 (1995).
17. Tokmakoff, A. et al. Infrared Vibrational Photon-Echo Experiments in Liquids and Glasses. *Journal of Physical Chemistry* **99**, 13310-13320 (1995).
18. Dougherty, T. & Heilweil, E. Ultrafast transient infrared absorption studies of M(CO)6 (M = Cr, Mo or W) photoproducts in n-hexane solution. *Chemical Physics Letters* **227**, 19-25 (1994).

19. ARRIVO, S., DOUGHERTY, T., GRUBBS, W. & HEILWEIL, E. ULTRAFAST INFRARED-SPECTROSCOPY OF VIBRATIONAL CO-STRETCH UP-PUMPING AND RELAXATION DYNAMICS OF W(CO)(6). *CHEMICAL PHYSICS LETTERS* **235**, 247-254 (1995).
20. Tokmakoff, A., Sauter, B. & Fayer, M.D. Temperature-Dependent Vibrational-Relaxation in Polyatomic Liquids - Picosecond Infrared Pump-Probe Experiments. *Journal of Chemical Physics* **100**, 9035-9043 (1994).
21. Anna, J.M. & Kubarych, K.J. Watching solvent friction impede ultrafast barrier crossings: A direct test of Kramers theory. *J. Chem. Phys.* **133**, 174506 (2010).

Chapter 5

Vibrational Energy Transfer and Spectral Diffusion Dynamics in a Vibrational Aggregate with Disorder-Induced Delocalization

5.1: Introduction

5.1.1 Dynamics

Solvation dynamics play a crucial role in reaction chemistry.[1] In order to understand them ultrafast time resolution is required. Hydrogen-bonding in particular produces fast and complex solvent fluctuations, resulting in dynamics that are impossible to extract from a static one dimensional spectrum.[2-5] Two dimensional infrared (2DIR) spectroscopy provides both sensitivity to solute fluctuations as well a femtosecond time resolution. Together, these allow the exploration of factors involved in solvating small molecules. Previous work has measured the frequency fluctuations in complex hydrogen-bonded environments, including OH/OD and liquid water solutions.[6] Frequency-frequency correlations help link observable spectral evolution to underlying molecular dynamics using both molecular dynamics simulations and, in the case of hydrogen-bonding, excitonic-based calculations and electrostatic maps based on *ab initio* calculations.[7] Most exciton considerations, however, focus on electronic chromophores, where single exciton excitations are normally considered, there is generally less localized sensitivity, and information is reduced to a single excitonic state.[8] The vibrational analogue can contain multiple overlapping excitons resulting from a high degree of delocalization.[9] The local vibrational units become a useful tool to monitor both short-

and long-range correlations in both the molecule and its environment, while the number of excitons allows for the study of the interaction of many molecular modes.

Triruthenium dodecacarbonyl, $Ru_3(CO)_{12}$ (TRDC), is a molecule of interest in many ways. Used as a catalyst in CO exchange reactions, the method of rearrangement and extraction of particular interest.[10] Harris et al. and Ihee et al. have previously shown that several products result from photoexcitation, each with different dynamics.[11-13] In order to understand the reaction chemistry, however, the equilibrium solvation dynamics must first be characterized. This provides an excellent opportunity to study a nearly spherical molecule that nevertheless contains distinct internal dynamics.

$Ru_3(CO)_{12}$contains three primary IR-active CO stretching bands at 2011, 2031, and 2060 cm^{-1}. The high and low frequency bands are each pairs of degenerate E' modes composed of a mixture of axial and equatorial carbonyls, while the third, middle-frequency A_2" mode is entirely isolated to the six axial carbonyls (**Fig. 1**). Additional peaks at lower frequencies are observed in linear spectra for solvents that interact more weakly with the compound, likely including a third predicted degenerate E' pair near 2000 cm^{-1}. The isolated mode provides a unique window to understanding intramolecular vibrational energy redistribution (IVR) in solvation. Because there is no overlap between the three ground state orthogonal normal modes, energy transfer must be considered using a non-ground-state model. This is accomplished by considering the normal mode basis in an exciton framework.[9] Solvation is then modeled as a gaussian disorder, providing sufficient impetus to break the ground state symmetry of unsolvated $Ru_3(CO)_{12}$ and induce overlap between the otherwise isolated normal modes. The result is a simple exciton model that predicts many of the solvation dynamics associated with highly interacting and hydrogen-bonding solvents.

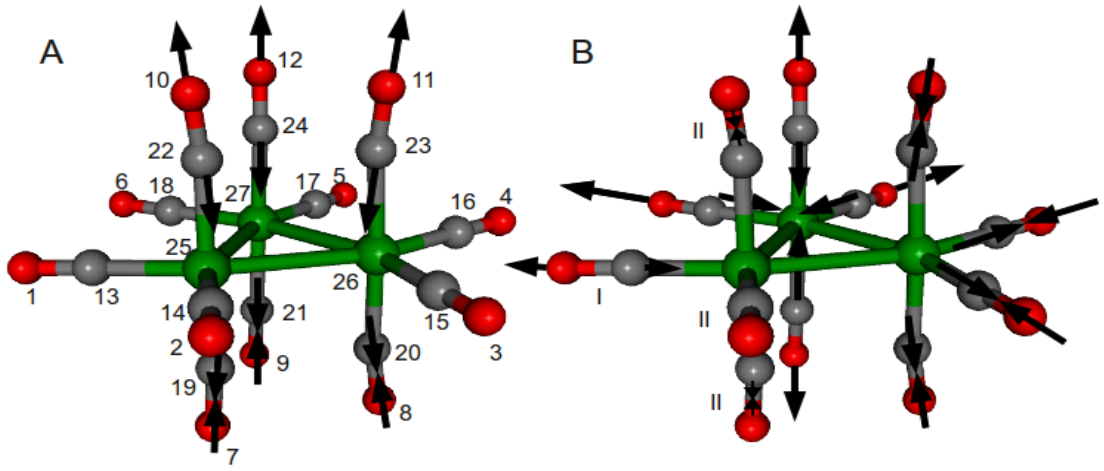

Figure 43: Two vibrational modes of $Ru_3(CO)_{12}$ as calculated by DFT. (a) Mode 8, the mode which gives rise to the middle frequency band at 2031 cm^{-1}, is labeled by atom in the arrangement used to generate the Hamiltonian. Carbonyls are numbered the same as the oxygens, and are composed of an oxygen atom labeled n and a carbon atom labeled n + 12. (b) Mode 11, one of two degenerate modes that gives rise to the high frequency band at 2060 cm^{-1}. Though the bulk of the carbonyl groups move with roughly equal amplitude, the CO labeled I moves significantly less, and those labeled II essentially do not move at all.

5.1.2 Spectral Diffusion and Intermolecular Vibrational Energy Redistribution

Linear IR spectra contain much information in the frequency domain in the form of peak positions, shapes, intensity, etc. that informs on the underlying molecular dynamics.[14,15] In solution constant fluctuations make extraction of this information difficult, resulting in situations where different dynamics can produce similar linear features. Time-resolved spectroscopies remove the limitation of relying on static information by measuring dynamic processes directly in the time domain. 2DIR specifically correlates initial frequency to detected frequency after evolution during a waiting time, directly monitoring fluctuations in the transition frequencies, which reflect atomic scale motions.[16] These correlations produce many effects on the two-dimensional line shapes and intensities. Analogous to in a linear spectrum, a fully absorptive 2DIR spectrum is the sum of the real parts of a rephasing and a non-rephasing spectrum. Rephasing spectra undergo phase evolution during detection conjugate to that during excitation, contrary to

non-rephasing spectra, and each can be represented as a separate set of Liouville pathways that give time and energy ordering to the excitations.[17] Inhomogeneous broadening causes a signature tilt to absorptive 2D peaks where the rephasing spectrum is enhanced, resulting from an imbalance between the rephasing and non-rephasing pathways. Conceptually, the tilt represents the isolation of distinct local environments where solvation has shifted the frequency of the solute. At early waiting times the solute has no time to sample additional local solvation states, resulting in a high degree of correlation between excitation and detection frequency while simultaneously displaying a broadened range of solute frequencies. At longer waiting times this imbalance relaxes as molecular memory is lost to microstate exploration. The solute samples a larger fraction of the local environments, which is detected as correlation between the initial local environment and additional local environment frequencies. Thus, a primarily diagonal, elongated peak slowly relaxes to a rounded peak lacking a tilt. The frequency-frequency

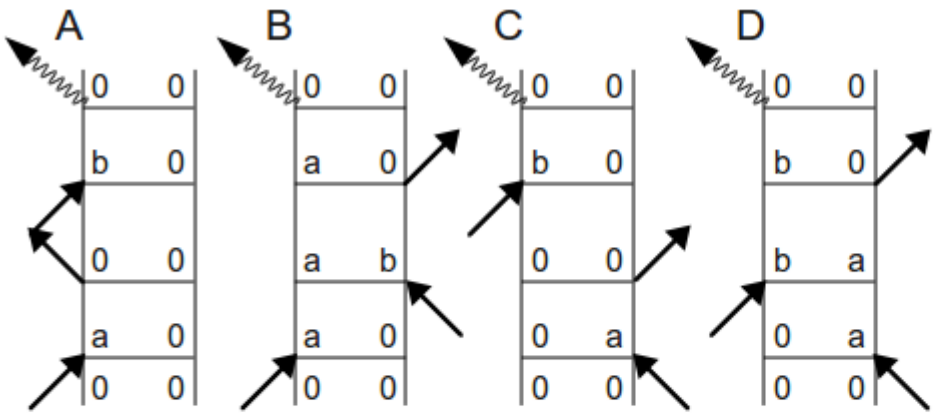

Figure 44: Representative Feynman diagrams showing the excitation orders resulting in the t_2 behavior of interest. Diagrams (a) and (b) are non-rephasing pathways and (c) and (d) are rephasing pathways. In (a) a ground state population evolves during the waiting time and a cross peak is produced at $\omega_1 = a$ and $\omega_3 = b$, while in (b) a coherence oscillates during the waiting time and a diagonal peak is produced at $\omega_1 = a$ and $\omega_3 = a$. In (c), a ground state population evolves during t_2 producing a cross peak, while in (d) a coherence oscillates during the waiting time and adds to the peak at $\omega_1 = a$ and $\omega_3 = b$.

correlation can be extracted without the fully absorptive spectrum from the inhomogeneity index

$$I = \frac{A_{rephasing} - A_{nonrephasing}}{A_{rephasing} + A_{nonrephasing}}, \tag{31}$$

where A is the amplitude of a single 2D peak in a given pair of rephasing and non-rephasing spectra, by monitoring peak amplitudes as a function of waiting time.[9] The time dynamics of this index are generally captured by single exponential decay, which gives the spectral diffusion rate and lifetime of the molecule in a given solvent. Additional decay components such as the vibrational lifetime cancel out as they are expected to be the same in both spectra. Additional components may also include a static offset, indicative of long-time correlations beyond the scope of the experiment performed.

In addition to solvent induced relaxation effects, molecules also undergo intramolecular vibrational energy redistribution (IVR), where IR active vibrational populations relax into other vibrational modes (including IR-dark Raman modes).[18-21] This relaxation can be seen as an additional decay component in 2DIR peak amplitudes where population is being lost, and as growth in populations that increase during the waiting time. This can be thought of as population exchange, similar to isomeric exchange in more familiar systems reaction systems. Unlike the more commonly studied electronic exciton systems, however, where the energy barrier to population transfer is many times k_BT, in vibrational systems the energy gap between vibrations is on the order of k_BT. This counter-intuitively allows for population transfer in what would generally be considered the uphill direction on the energy landscape. Thus, two types of IVR behavior will be seen: where generally but not necessarily higher frequency peaks decay with a fast, few picosecond lifetime into either a dark mode with an undetected growth during the waiting time or into an IR active mode exhibiting any growth at all during waiting time. Though the sum of the growth due to IVR would theoretically match exactly the sum of the loss, decay to dark modes in practice makes this impossible.

5.1.3 Excitonic Modeling

2DIR spectroscopy provides access to additional hidden dynamics beyond linear spectroscopy, but can be difficult to interpret. A model often is necessary to fully characterize the molecular dynamics.[7] Ranging from *ab initio* calculations for few-atom small molecules to molecular dynamics energy landscapes in large proteins, a variety of behaviors can be captured or overlooked. In small systems, typically few chromophores are found proximate. In metal carbonyls, however, the excess of CO groups on the molecule provide the ability to study excitations that have been previously considered more from an electronic standpoint.[9] Excitonic models are often used in highly coupled electronic systems where a high degree of electron delocalization leads to a whole molecule picture excitation, HOMO to LUMO transitions being a general example.[8] In vibrational systems, highly delocalized vibrational excitons have only recently been studied. Metal carbonyls provide a fertile framework for further exploration of these vibrational aggregates. Because of the coupling limitations, the vibrational energy landscape is in principle easily calculable as compared to electronic transitions, making modeling vibrational excitons much more feasible.

In an excitonic picture, a fully coupled Hamiltonian is first calculated. In electronic spectroscopy, the input usually includes a collection of transition frequencies that may or may not be complete, and few if any absolute transition amplitudes (oscillator strengths). A Hamiltonian is then generated that fits these constraints.[22] Such a system, however, can be underdetermined, resulting in a range of possible Hamiltonians that will behave differently when perturbed.[23] The additional complexity of chemically modeling such systems makes adding missing constraints to the system difficult. As a result, many excitonic Hamiltonians, while representative of *a* system with the given constraint frequencies and amplitudes, may not represent *the* system under consideration. In considering a vibrational aggregate, however, missing frequencies and amplitudes are easily calculated, resulting in a fully constrained Hamiltonian that can be much more accurate.

Using the generated Hamiltonian, solvation is modeled as a disorder in the local

site basis. Adding a single parameter of gaussian white noise $\delta\omega$ to each oscillator frequency ω_{osc} and subsequent rediagonalization produces a realization of the frequency spectrum of the disordered excitonic system. A range of noise parameters introduced maps out the frequency response to disorder. Experimental spectra can then be compared to the model spectra using their expected disorder, where highly interacting solvents (highly polarizable, dipole, etc.) are considered to impart a high degree of disorder.

5.2: Experimental and Modeling Methods

The implementation of 2DIR has been described elsewhere.[24] Briefly, a dual-OPA dual-DFG configuration generates two frequencies of independently tunable mid-IR. For the purposes of this experiment both were tuned to the frequency range of the CO stretch in $Ru_2(CO)_{12}$, approximately a 2050 cm^{-1} center frequency. The DFG output is split into four fields E_1, E_2, E_3, and E_{LO} with corresponding wave vectors k_1, k_2, k_3, and k_{LO}. The first three are focused into the sample in a box geometry, producing a four wave mixing signal $E_{+/-}$ with wave vector $k_{+/-}$ in the background free phase matched direction $k_{\pm.} = \pm k_1 \mp k_2 + k_3$. This signal is then mixed with E_{LO} providing a reference for heterodyne detection. Both signal and reference are upconverted by sum frequency generation in a lithium niobate crystal with leftover chirped 800 nm light from the regenerative amplifier. The resulting light near 690 nm is dispersed in a spectrometer and collected by conventional CCD camera, providing the detection axis for the 2DIR spectra. The excitation axis is obtained by scanning the time delay t_1 between k_1 and k_2 and subsequent Fourier transform after collection. A series of these spectra are obtained by stepping the time delay t_2 between k_2 and k_3, which are then used to extract time dependent dynamics with resolution limited by the IR pulse width of 100 fs. Linear spectra were also taken by FTIR spectrometer to compare extracted inhomogeneous line widths.

From a series of 2DIR spectra, the peak amplitudes of the rephasing and non-rephasing spectra are found at each t_2 waiting time. Oscillating peaks arise from pathways that evolve as a coherence during t_2, and are found along the diagonal in non-rephasing

spectra and cross peaks in the rephasing spectra (**Fig. 2**). The rephasing diagonal peaks and non-rephasing cross peaks contain terms that undergo only population evolution over t_2, containing therefore only pure growth and decay terms.[17] For the non-rephasing peaks, the cross peak amplitudes are plotted as a function of t_2 and the corresponding decay rates k extracted by fitting a double exponential. These rates contain information on every decay process that occurs during t_2, in particular any IVR that occurs. This is generally captured in the fast rate extracted by fitting, with the slower rate capturing the longer vibrational population decay. To extract the spectral diffusion rates, the difference of the amplitudes of a diagonal rephasing peak and the corresponding non-rephasing peak is divided by their sum to produce the Inhomogeneity ratio. This gives a reduced ratio representing the inhomogeneity of the system at each t_2 waiting time. In the highly inhomogeneously broadened limit the ratio reduces to $A_{[non-]rephasing}/A_{[non-]rephasing} = 1$. Once the system has relaxed the rephasing and non-rephasing amplitudes are roughly equivalent and the ratio approaches the limit of $0/(A_{rephasing}+A_{non\text{-}rephasing}) = 0$. The decay of this ratio is extracted by fitting a single exponential, producing a rate k_{SD} for the spectral diffusion.

To fully elucidate the experimental 2DIR results an excitonic model was developed. Excitonic models are more commonly used in modeling electronic systems, relying on the partial experimental picture of select measurable frequencies and minimal oscillator strength data. One advantage of studying smaller molecules is the ability to accurately model them using density functional theory. DFT modeling of $Ru_3(CO)_{12}$ matches crystal structure data well and also finds nearly correct frequencies for the CO transitions.[12] We therefore use the DFT-generated frequencies and oscillator strengths of the 12 CO modes of $Ru_3(CO)_{12}$ to generate a model Hamiltonian by a genetic algorithm search.

Using a similar process to our previous work on dimanganese decacarbonyl, the Hamiltonian

$$H = \sum_{n=1}^{12} \varepsilon_n |n\rangle\langle n| + \sum_{m \neq n=1}^{12} J_{mn} |m\rangle\langle n| \quad (32)$$

,

is composed of diagonal energies ε_n and off-diagonal couplings J_{mn}. $Ru_3(CO)_{12}$ contains 12 CO groups of two symmetry types, axial and equatorial, giving rise to two local vibrations S_1 and S_2.[9] Symmetry dictates the relation for off-diagonal couplings C_1 through C_{10}, producing a full Hamiltonian matrix

$$H=\begin{bmatrix} S_1 & C_1 & C_5 & C_7 & C_5 & C_8 & C_3 & C_9 & C_6 & C_3 & C_9 & C_6 \\ C_1 & S_1 & C_8 & C_5 & C_7 & C_5 & C_3 & C_6 & C_9 & C_3 & C_6 & C_9 \\ C_5 & C_8 & S_1 & C_1 & C_5 & C_7 & C_6 & C_3 & C_9 & C_6 & C_3 & C_9 \\ C_7 & C_5 & C_1 & S_1 & C_8 & C_5 & C_9 & C_3 & C_6 & C_9 & C_3 & C_6 \\ C_5 & C_7 & C_5 & C_8 & S_1 & C_1 & C_9 & C_6 & C_3 & C_9 & C_6 & C_3 \\ C_8 & C_5 & C_7 & C_5 & C_1 & S_1 & C_6 & C_9 & C_3 & C_6 & C_9 & C_3 \\ C_3 & C_3 & C_6 & C_9 & C_9 & C_6 & S_2 & C_4 & C_4 & C_2 & C_{10} & C_{10} \\ C_9 & C_6 & C_3 & C_3 & C_6 & C_9 & C_4 & S_2 & C_4 & C_{10} & C_2 & C_{10} \\ C_6 & C_9 & C_9 & C_6 & C_3 & C_3 & C_4 & C_4 & S_2 & C_{10} & C_{10} & C_2 \\ C_3 & C_3 & C_6 & C_9 & C_9 & C_6 & C_2 & C_{10} & C_{10} & S_2 & C_4 & C_4 \\ C_9 & C_6 & C_3 & C_3 & C_6 & C_9 & C_{10} & C_2 & C_{10} & C_4 & S_2 & C_4 \\ C_6 & C_9 & C_9 & C_6 & C_3 & C_3 & C_{10} & C_{10} & C_2 & C_4 & C_4 & S_2 \end{bmatrix},$$

again with high symmetry.

Additionally, the search is also constrained to fit the DFT calculated atomic motions (eigenvectors). This is not possible in studying electronic systems, as the electronic motions are not currently calculable. We found, however, that simply fitting the frequencies and oscillator strengths would often result in a model whose mode motions are entirely incorrect. This lead to serious concern that such a generated Hamiltonian, though reflective of *a* system with said frequencies and amplitudes, we not reflective of *this* system. Thus, the full constraint is given by

$$f=\sum_{n=1}^{12} a\left(\omega_{n,DFT}-\omega_n\right)+b\left(\mu_{n,DFT}-\mu_n\right)+c\left(\psi_{n,DFT}-\psi_n\right) \tag{3}$$

where α, β, and γ are scaling factors to adjust the amplitudes of frequency versus oscillator strength versus wave function error. Little difference was found with a ratio of scaling factor less than 10 for any given pair.

The inputs are the DFT frequencies, oscillator strengths, and amplitudes, as well

as the axial versus equatorial oscillator strength ratio. The resulting eigenvectors from genetic algorithm Hamiltonian generation closely match the DFT computed motions and result in exact agreement with the DFT transition frequencies and amplitudes. Agreement was found by constraining the ratio between axial mode transition dipole strength and equatorial mode transition dipole strength to between 1.3 and 1.6. This description neglects vibrational anharmonicty, modeling only the first vibrational level of excitation. Though there are several methods of including higher order excitations, those states are unnecessary for the present work.

Once the Hamitonian is generated, disorder is introduced by adding uncorrelated Gaussian frequency noise to each diagonal energy for each realization of the Hamiltonian. A range of disorder from 0 to 20 cm^{-1} was used. The delocalized disordered frequencies and transition moments are then determined from diagonalization of 5000 realizations of the Hamiltonian while varying the degree of noise. The transition moments are calculated assuming that the CO local mode transitions are parallel to the CO bond axis. The 1D spectrum is computed by applying a Voigt profile with input homogeneous and inhomogeneous widths and weighting each transition by the square of the transition moment. The modes are labeled from 1 to 12 in increasing frequency, and identified according to their zero disorder transition moments, with modes 6, 7, 8, 10, and 11 being designated IR active and modes 1, 2, 3, 4, 5, 7, and 12 designated as Raman active. It should be noted that modes 1 and 2 are weakly IR active and appear in at least some of the linear spectra, and modes 4 and 5, while Raman active, nearly overlap in frequency with the strongly IR active modes 6 and 7. Raman-active mode 9 also nearly overlaps IR-active modes 10 and 11. This complicates the simulation results and discussion.

Disorder-induced localization is analyzed by calculating the participation ratio at each oscillator. Experiments in J-aggregates and light-harvesting proteins have indicated decreases in the size of excitons correlated with increased disorder.[9,25,26] While these systems and molecules are large with respect to $Ru_3(CO)_{12}$, the vibrations are delocalized over a large portion of the molecule, providing a similar excitonic framework. Given each eigenvector ϕ_n the participation ratio P_n is given by

$$P_n = \left[\sum_{m=1}^{12} \left(\phi_n \right)_m^4 \right]^{-1} \quad (4)$$

The participation ratio indicates the number of oscillators over which a given vibrational mode is delocalized.

5.3: Results

5.3.1 Experimental

Linear, rephasing, and non-rephasing spectra were taken of $Ru_3(CO)_{12}$ in a range of solvents including non-interacting n-hexane and the alcohol chain series. For the 2D spectra, data was recorded for waiting times between 0 and 60 ps to allow all relaxation dynamics to be observed. The three bands of $Ru_3(CO)_{12}$ have frequencies of 2011, 2031, and 2060 cm^{-1} in n-hexane, and deviate little in different solvents. The linear spectra show a trend of increasing inhomogeneous broadening in solution, where the narrowest linewidths of approximately 8 cm^{-1} occur in n-hexane and broaden to over 25 cm^{-1} in ethanol (**Fig. 7b**). This broadening is not uniform, however, with the 2011 and 2060 cm^{-1} bands broadening by almost twice as much as the 2030 cm^{-1} band. Additional bands also appear at lower frequencies in weakly interacting solvents. Specifically, three additional peaks are seen at 1978, 1986, and 2000 cm^{-1}, only one of which is predicted based on modeling and previous results.[11] The 2000 cm^{-1} peak is most likely a weakly IR active degenerate pair of modes as indicated by DFT calculations. The 1978 and 1986 cm^{-1} peaks match neither previous frequency data nor DFT calculations. We ascribe them to either isotopic effects or overtones of the visible IR modes, and will no be discussed further. Additionally, spectra in methanol deviate substantially. The three visible bands present in other solutions are now impossible to discern in the liner spectrum, replaced instead by a single broad band.

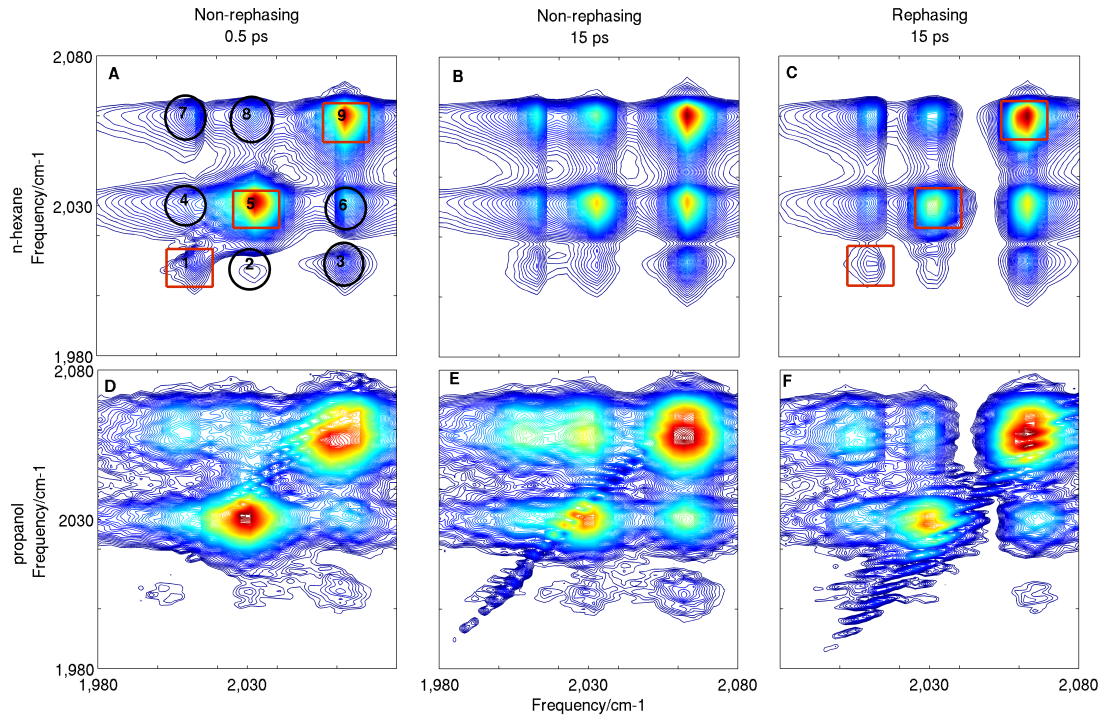

Figure 45: Representative t_2 spectra of $Ru_3(CO)_{12}$. Spectra (a) through (c) are in n-hexane, (d) through (f) are in hexanol, (a), (d) are non-rephasing at 500 fs, (b), (e) are non-rephasing at 15 ps, and (c), (f) are at rephasing at 15 ps. Peaks are labeled 1 through 9 in (a) from low to high frequency—not to be confused with mode numberings used in the calculations. Circled are the crosspeaks used to fit IVR (peaks 2-4, 6-8). In boxes are the diagonal peaks used to calculate the inhomogeneity ratio to fit the spectral diffusion (both (a) and (c)).

This is not inconsistent with model predictions at high disorder, but is also not in line with the broadening trend presented by the remaining alcohol series.

The 2DIR rephasing and non-rephasing spectra show lineshapes broadened by phasing effects (**Fig. 3**). This broadening is eliminated when the fully absorptive 2D spectrum is computed, but this is unnecessary here, as the peak amplitudes contain all the information for this paper. The 2D spectra contain three diagonal peaks corresponding to the three fundamental IR bands of $Ru_3(CO)_{12}$ in solution, as well as the corresponding cross peaks for excitation of one band and detection of another, even at the earliest waiting times (t_2 = 0 ps). This occurs because the three frequencies share a common molecular ground state, so pathways exist in each case for excitation of one mode and detection

of another. This gives nine fundamental peaks in the 2DIR spectra. Additionally, anharmonic peaks indicative of the $\upsilon_{1\rightarrow 2}$ transition are generally present in 2DIR spectra, shifted, usually to lower frequency, by the anharmonic shift of the vibrational potential well. No such anharmonic peaks are seen here, however, indicating one of two possibilities. Firstly, the anharmonic shift could be sufficiently small for $Ru_3(CO)_{12}$ as to hide these peaks under their corresponding fundamentals in the unphased rephasing and non-rephasing spectra. As such, only 9 distinct peaks would be seen in the spectra presented here. Note that this could lead to additional terms in any peak amplitudes calculated by peak volume, as the anharmonic peaks are not distinguishable in finding boundaries to take peak volumes. Amplitudes were therefore also found by taking the single peak point values as well as volumes in order to compare to the values calculated with volumes. It was found that there was no discernible difference in all cases. In the second case the anharmonic shift of $Ru_3(CO)_{12}$ could be sufficiently large as to shift these anharmonic peaks toward significantly lower frequencies and out of the range of detection. This could also explain the additional low frequency peaks observed in low disorder linear spectra. Distinguishing these cases is beyond the scope of this work, in which it is unnecessary to consider the anharmonic components for experimental and modeling purposes. It is sufficient to simply show that no anharmonic portion is being sampled by the peak volume calculations.

Intramolecular vibrational redistribution. Peaks in the rephasing and non-rephasing spectra can oscillate with t_2 if they propagate as a coherence between two (excited) modes during the waiting time.[27,28] Which peaks can oscillate is dictated by the specific pathways available in rephasing versus non-rephasing. A sample of this is shown in Figure 5.2. In rephasing spectra, the off-diagonal crosspeaks oscillate, whereas in non-rephasing spectra, the diagonal peaks oscillate. Thus, using the non-rephasing off-diagonal peaks eliminates coherence lifetime effects from the measured t_2 behavior. Additionally, IVR can be thought of as an exchange between two modes similar to an exchange between two species. Intuitively, two exchanging species would result in a growth of crosspeak amplitude as species one became species two during t_2, and vice versa. IVR produces the same result; there is, however, an additional peak component

present at $t_2 = 0$ due to the shared molecular ground state. Thus, crosspeaks will grow, but from an already present peak. The predicted initial values of these peaks is given by an isotropic distribution function.[29] Deviation from these values can be indicative of

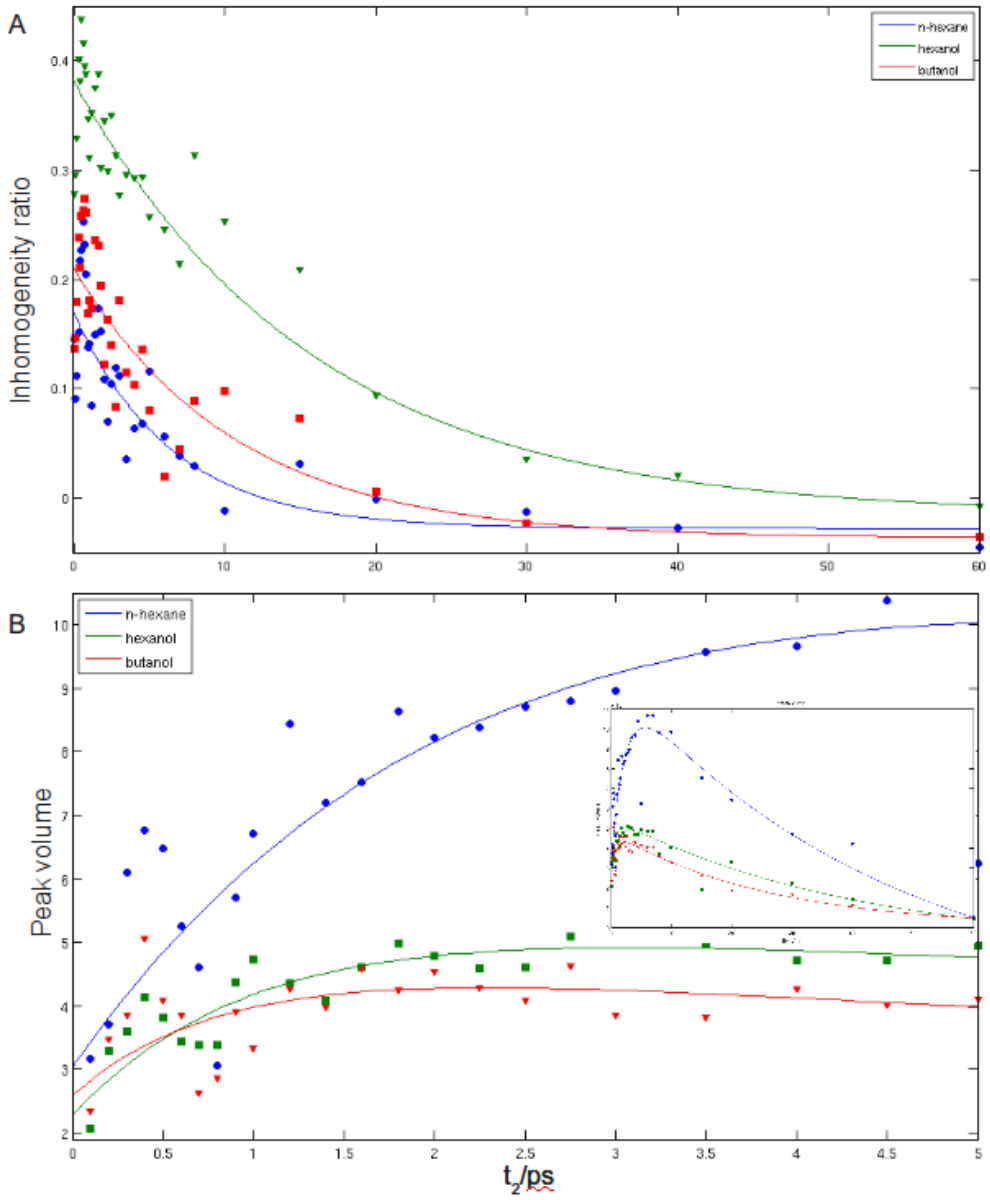

Figure 46: (a) The inhomogeneity ratio of peak 5 as a function of waiting time for three solvents n-hexane, hexanol, and butanol with their corresponding fits. (b) Volume of peak 3 as a function of waiting time for the same solvents with fits. The initial growth within 10 ps is shown in the main figure, while the full growth and decay over 60 ps is shown in inset.

behaviors faster than the timescale of the experiment.

The IVR rates are obtained from double exponential fits of the t_2 amplitude of the non-rephasing cross peaks (**Fig. 4a**). The long time decay component corresponds to vibrational lifetime, and was found to be consistently longer than the 60 ps scanned here. There was some variation but is most likely due to insufficient long time points to outweigh noise on the final few points. The short time component varies by peak, decaying for some cross peaks and growing in others, corresponding to population transfer between modes during t_2. Contrary to previous works, no discernible trend can be seen for the alcohol series.

Spectral diffusion. The spectral diffusion rates are obtained from single exponential fits of the inhomogeneity ratio (**Fig. 4b**). These vary by peak as well, indicating different rates, and possibly different mechanisms, of local sampling for the different modes. Peak 1 in particular shows a markedly longer spectral diffusion time in most solvents than peaks 5 and 9 (**Fig. 5**). Peak 5 shows a longer spectral diffusion time for the alcohol series compared to less interacting solvents, while peak 9 shows more complex behavior,

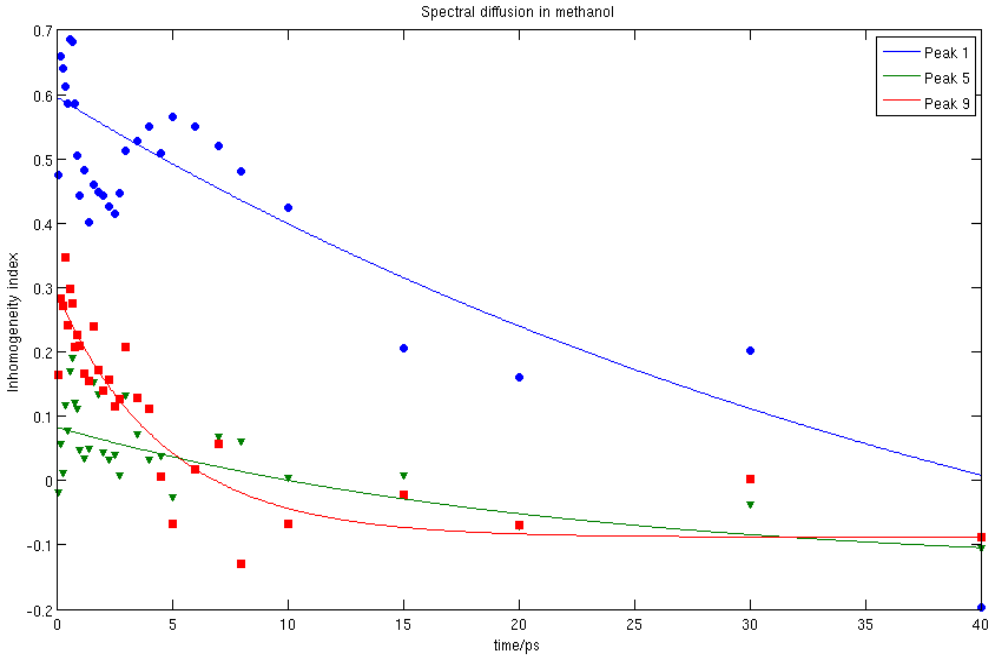

Figure 47: Comparison of the inhomogeneity ratio of peaks 1, 5, and 9 in the same solvent. Peak 1 shows significantly slower spectral diffusion.

with a longer time in n-hexane and cyclohexane, but a shorter time in acetone and THF. Calculating spectral diffusion times was hampered by noise, particularly in weaker peaks, giving fits of the decay of the inhomogeneity index for peak 1 a wider confidence interval.

Table 1: IVR Time Constants (in ps). Growth given negative sign, highlighted in yellow.

Solvent	**Peak Number**					
	2	**3**	**4**	**6**	**7**	**8**
n-hexane	0.52 ± 0.24	-2.17 ± 1.08	1.10 ± 0.47	----	-2.86 ± 0.99	-15.29 ± 0.16
cyclohexane	0.17 ± 0.03	----	0.92 ± 0.21	----	-2.71 ± 0.59	-6.24 ± 0.08
acetone	0.44 ± 0.28	0.44 ± 0.06	0.45 ± 0.21	0.34 ± 0.24	-0.80 ± 0.16	----
THF	0.56 ± 0.32	0.92 ± 0.01	0.74 ± 0.61	0.30 ± 0.29	-0.40 ± 0.06	----
hexanol	0.91 ± 0.45	-1.00 ± 0.37	0.61 ± 0.24	0.19 ± 0.06	-1.62 ± 0.23	----
butanol	0.75 ± 0.66	-0.83 ± 0.18	0.50 ± 0.19	0.28 ± 0.09	-5.62 ± 0.04	0.25 ± 0.03
propanol	0.75 ± 0.53	-0.12 ± 0.03	0.99 ± 0.87	0.54 ± 0.32	-0.17 ± 0.01	0.13 ± 0.03
ethanol	1.62 ± 0.5	----	1.05 ± 0.29	0.30 ± 0.07	----	2.45 ± 0.02
methanol	0.98 ± 0.71	0.60 ± 0.07	0.72 ± 0.42	0.35 ± 0.11	-0.12 ± 0.03	-0.59 ± 0.08

Table 2: Spectral Diffusion Time Constants (in ps)

Solvent	Peak Number		
	1	**5**	**9**
n-hexane	28.15 ± 0.86	6.42 ± 0.81	12.04 ± 1.35
cyclohexane	101.3 ± 1.95	5.67 ± 0.61	10.45 ± 1.08
acetone	4.84 ± 0.59	6.89 ± 0.85	2.51 ± 0.35
THF	2.86 ± 0.38	3.28 ± 0.42	2.22 ± 0.35
hexanol	151.56 ± 22.22	15.83 ± 2.13	5.23 ± 0.71
butanol	17.58 ± 2.12	10.66 ± 1.33	4.89 ± 0.76
propanol	27.61 ± 4.01	10.18 ± 1.41	5.46 ± 0.86
ethanol	11.42 ± 1.62	22.56 ± 3.14	6.58 ± 0.88
methanol	46.65 ± 6.79	21.44 ± 2.75	4.68 ± 0.65

5.3.2 Modeling

The genetic algorithm was allowed to run with and without pre-defined starting points and over numerous repetitions. The algorithm typically converged in less than 100 generations, and repeated runs had little change. The resulting eigenvalues and couplings were constant to within less than 1% of every output value. The result of the measured compound error was less than 4% over every variable, including the eigenvector overlap (**Fig. 6c**). This indicates robust and close agreement with the DFT generated atomic motions (**Fig. 6a,b**). Interestingly, when the eigenvector component of the error function was relaxed, the algorithm had trouble converging both the frequencies and amplitudes to the DFT calculated values. When the generated eigenvectors were then compared to the DFT motions, they were found to deviate substantially. They were thus incorporated into the error function, ensuring correct Hamiltonian prediction for not just this set of frequencies and amplitudes, but these exact vibrations. The calculated Hamiltonian can be recon-

structed from the optimized values given in Table 1. Finally, the dipole ratio of 1.37 was calculated, providing all necessary parameters to calculate the disordered spectra.

From the simulated system, it can be seen that any disorder causes splitting of both IR and Raman degenerate modes, with more splitting in the IR than Raman modes. At low disorders this splitting manifests as simply a broadening of 1D line shapes, but sufficient disorder causes the beginning of two peaks to take shape (**Fig. 7a**). Additional lineshape broadening occurs due to the disorder itself, though this effect is smaller. This can be seen in the high disorder line widths of the low and high frequency IR active bands as compared to the middle frequency band. The high and low frequency bands are composed of degenerate modes whose disorder-induced splitting clearly causes significantly broader line shapes. The low frequency band all but disappears into an undifferentiated shoulder at higher disorders, composed of weak IR and slightly activated Raman modes. In addition to splitting, disorder causes frequency shifts of both IR and Raman modes both to higher and lower frequencies. Specifically, the IR modes 6 and 7 both shift

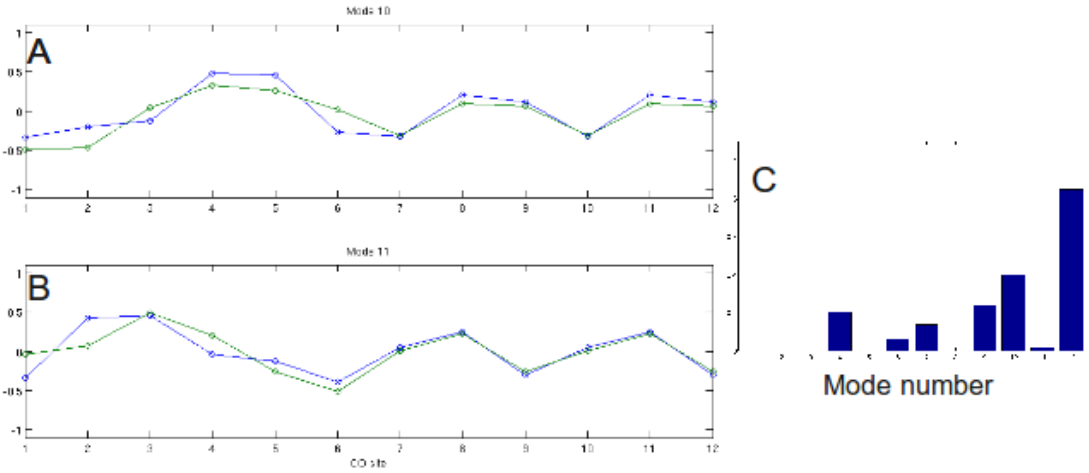

Figure 48: (a), (b) Comparison of the eigenvector found by Hamiltonian generation to the DFT calculated amplitudes of carbonyl motion for modes 10 and 11 respectively. Carbonyls are labeled 1 through 12 from left to right. Note the particularly good agreement for carbonyls 7 through 12 in mode 11. This in part gives rise to the difference between the two modes in (c), the aggregate eigenvector error on each mode (1-12). Error is a simple sum of the square of the residuals of the DFT amplitudes minus the eigenvectors. The sum of these errors is the function used for minimizing eigenvector error by genetic algorithm.

up in frequency, while the weakly IR active modes 1 and 2 both shift down in frequency (**Figure 5.6**). With low disorder modes 10 and 11 split initially with a downward shift in total, but as disorder is increased the splitting increases and shifts upwards in total. The smallest splitting and shifting occurs in degenerate Raman modes 4 and 5, with less than a 2 cm^{-1} split total. These shifts in frequency are not observed in the experimental linear spectra despite being sufficiently large.

Table 3: Optimized Vibrational Exciton Hamiltonian Parameters

Parameter	**Value (cm^{-1})**	**Parameter**	**Value (cm^{-1})**
S_1	2028.1	C_5	4.86
S_2	2034.7	C_6	7.13
C_1	4.34	C_7	3.13
C_2	12.0	C_8	26.4
C_3	11.3	C_9	0.0064
C_4	11.0	C_{10}	4.26

Some Raman mode activity is seen at the highest disorders, though less than in previous works. Modes 8 and 9 nearly overlap in frequency but are not degenerate. At high disorders, however, mode 9 increases in frequency, allowing it to be distinguished from mode 8 (**Fig. 9**). The oscillator strength also increases the most of all the Raman modes, almost three times greater than the next highest oscillator strength. Thus, in the highly disordered spectrum this previously dark mode can be seen to play an important role, forming a clearly distinct peak at 2050 cm^{-1}. Other hints of dark mode activity can be seen at various disorder, but this is the only mode to produce a distinct peak. The splitting stems from changes in the participation ratio for each of the modes. In general, the IR active modes decrease in participation ratio with increasing disorder. There are two exceptions, however, where the mode PR increases. The two degenerate modes 10 and 11 behave in opposite manners. Mode 11 is shifted higher in frequency than the degenerate band with no disorder and shows a steady decrease in IPR with disorder. Mode 10, on

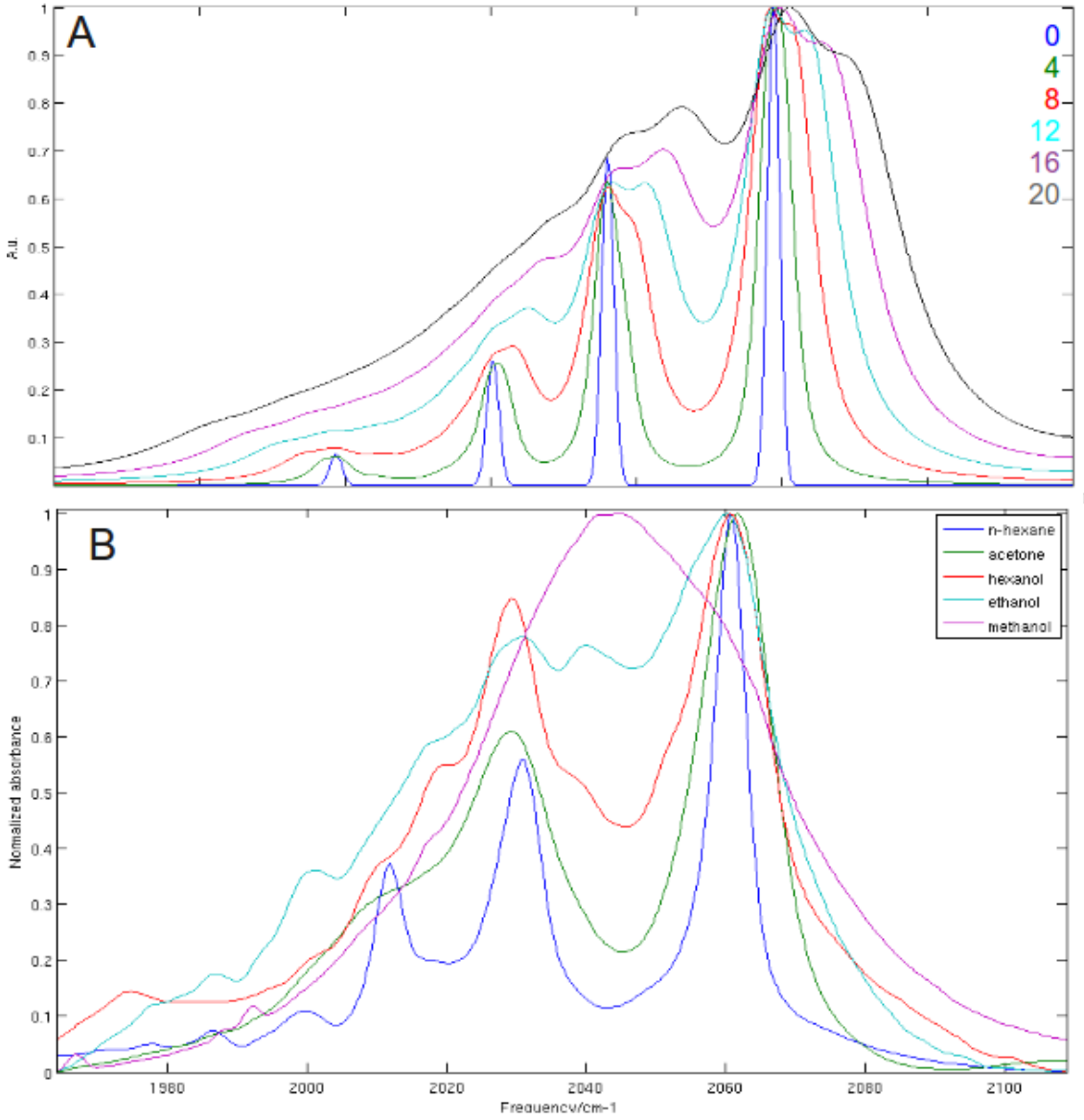

Figure 49: (a) Calculated linear spectrum as a function of disorder as compared to (b) experimental linear spectrum for a range of solvents. Note the clear turn on of a Raman mode near 2045 (mode 9) and the significant splitting of modes 10 and 11 to produce a broadened high frequency band, two distinct mechanisms which produce similar results. The small difference in experimental and calculated peak positions arises from small errors in the DFT frequencies.

the other hand, shifts slightly lower in frequency but shows an increase in IPR from 7.1 at 0 cm^{-1} broadening to 7.8 at 11 cm^{-1} of broadening, before falling below 7 at 25 cm^{-1} of broadening. Mode 2 as well, one of the degenerate pair 1 and 2, does not follow mode 1

in an initial downward trend, instead increasing sharply in IPR from 0 to 2 cm^{-1} of broadening before falling again. The Raman modes show less drastic IPR behavior than the IR. Modes 3, 9, and 12 all fall relatively smoothly with disorder, though the rates of IPR change differ. The degenerate modes 4 and 5, which showed little splitting, also show almost no IPR change, indicating some degree of isolation from solvation effects relative to the other modes, though mode 5 appears to increase slightly at medium disorder. Mode 4, which initially decreases, actually increases again at medium disorders, before decreasing again at high disorder.

The characterization of IR active versus Raman active is borne out by the results of the calculation. IR active modes have been shown to decrease in transition dipole strength as disorder is increased, while the transition dipole strength of Raman transitions

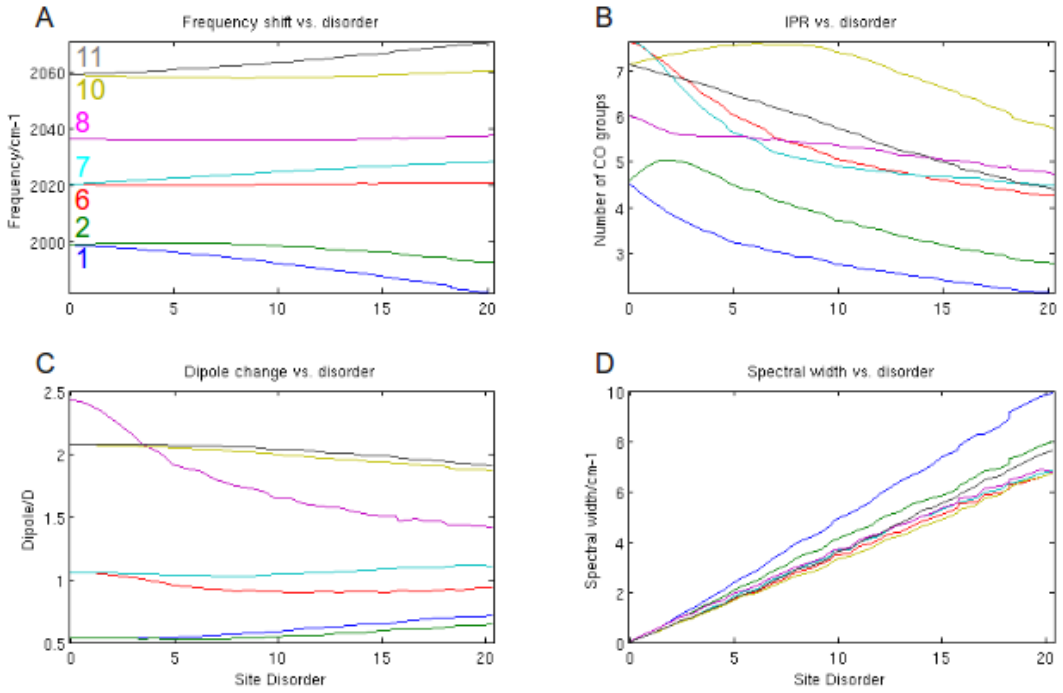

Figure 50: Shift with disorder of IR-active modes. Modes are labeled in (a). Splitting is shown in (a), IPR in (b), dipole change in (c), and spectral width in (d). Note the of IPR in (b) of modes 2 and 10. Also note the relative uniformity of spectral width in (d), which is clearly not the primary mechanism of broadening in the spectra in Figure 5.7. Finally, modes 1 and 2 are probably incorrectly classified as IR-active, as they are the only modes to increase dipole strength with disorder (see Figure 5.9).

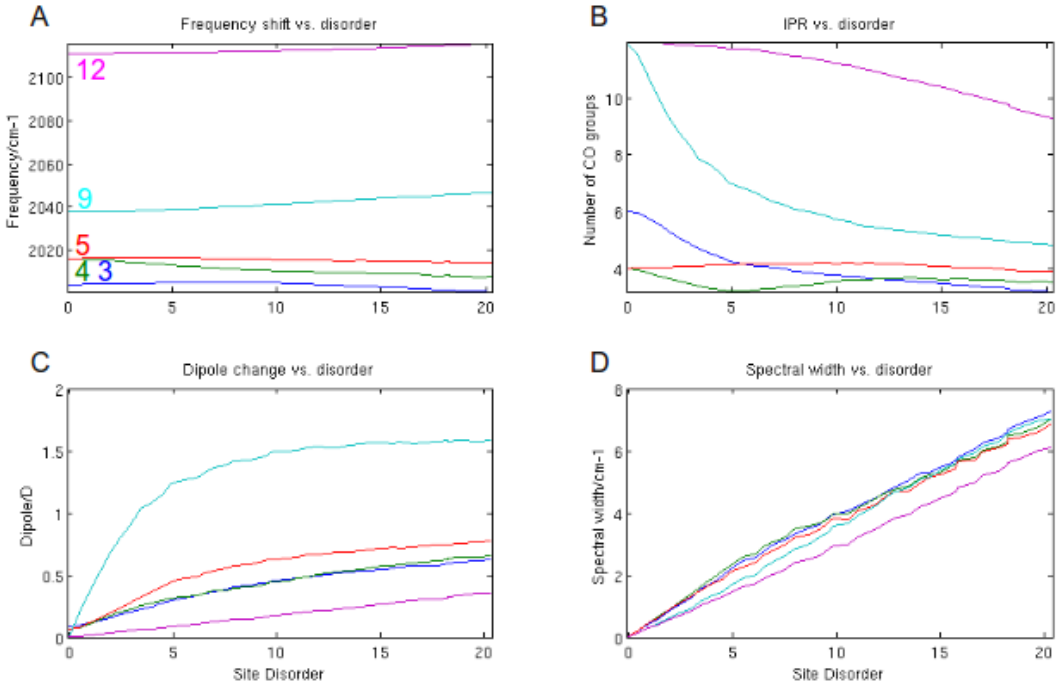

Figure 51: Shift with disorder of Raman modes. Layout is identical to Figure 5.8. Only mode 5 shows a very slight increase in PR in (b). Spectral widths are comparable in (d) to the IR-active modes. Finally, dipole strength increases for Raman modes.

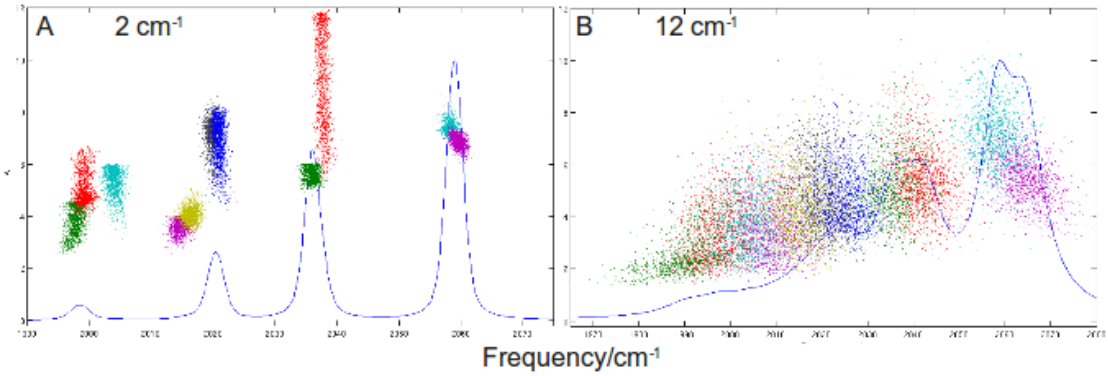

Figure 52: Calculated spectrum for (a) 2 cm^{-1} and (b) 12 cm^{-1} of broadening. The PR values for each mode are shown as separate clustered colors.

increases. IR modes 6, 7, 8, and 10 show a steady decrease in transition dipole moment, though again of differing magnitudes and rates. The transition dipole strength of modes 10 and 11 are almost constant, though they do exhibit a slight decrease at 20 cm^{-1} of broadening. All the Raman modes, however, show an increase with increasing disorder. Modes 3, 4, 5, and 12 all increase little, while mode 9 increases sharply at early disorder, before turning over and decreasing slightly at higher disorders. Of particular note are modes 1 and 2, which are weakly IR active. They increase in oscillator strength with disorder, reinforcing their very weak IR activity as more Raman in character.

5.4: Discussion

Previous work on spectral diffusion rates in a hydrogen bonding environment has indicated the solvent structuring works to preserve the solvent cage, causing a slower rate of interaction with the chromophore as hydrogen bonding character is increased (with increasing "disorder").[9] This lengthens IVR and spectral diffusion times and causes a high degree of localization at hydrogen bonded sites, as local solvent fluctuations are less frequent due to being bound in hydrogen bonds. Enough energy must be imparted in a sufficiently localized region to overcome the order of magnitude higher energy hydrogen bond that acts to freeze out fast solvation site dynamics. The systems under study, however, still formed relatively few hydrogen bonds between solvent and solute, meaning both the solute hydrogen bonds and the solvent hydrogen bonds are of importance. Furthermore, other systems were of even symmetry, whereas $Ru_3(CO)_{12}$ contains a three-membered ring. This feature causes unusual behavior in the vibrational delocalization in the normal modes, manifesting for example as excitons that contain a frustrated CO group whose motion is effectively zero. These frustrated motions arise due to symmetry arguments. IR-active transitions on a highly symmetric molecule must be dominated by asymmetric movements; symmetric movements will result in no net diople change, and hence no IR activity. In a group of three members, however, only two can participate in an antisymmetric movement directly, unless the antisymmetry is spread only partially over two members. The net result in $Ru_3(CO)_{12}$ is not spreading of the antisymmetry movements, however, and thus single COs are calculated to have little to no motion in

certain modes.

When solvent disorder is introduced the symmetry is broken and the excitons split in energy, losing degeneracy. In a local picture this can be thought of as removing the symmetry condition frustrating the CO group motion, allowing for the more standard delocalizations seen in vibrational aggregates. This in turn removes the strict antisymmetric requirements for IR activity, freeing the frustrated CO. This effect opposes that previously seen, causing an increase in spectral diffusion rate as the frustration is removed and small increases in the IVR rate due to larger wavefunction overlap between modes.

In particular, calculations show modes 2, 5, and 10 exhibit increase in PR with increasing disorder, before decreasing at the highest disorders modeled. An increase in PR corresponds to a greater number of carbonyl groups involved in the delocalized motion. In the case of mode 10 almost an entire additional carbonyl is involved. This corresponds to freeing a previously frustrated carbonyl group bound by symmetry conditions. Indeed, modes 2, 5, and 10 contain a frustrated carbonyl, as do their degenerate pairs 1, 4, and 11. While mode 10 increases by nearly a carbonyl in IPR, mode 11 decreases by just over one carbonyl. Together, this splitting helps to alleviate the symmetry-frozen condition that persists without disorder. Modes 1 and 2 show a similar splitting in IPR, though smaller in magnitude, as do modes 3 and 4, smaller again in magnitude.

Experimentally these effects appear as changes in internal energy redistribution as reflected in IVR, as well as changes to solvent couplings as reflected in spectral diffusion rates. Distinctly different IVR rates are seen on the IR active modes monitored by 2DIR. Cross peak 3 at $\omega_1 = 2060$ cm^{-1}, $\omega_3 = 2011$ cm^{-1} shows an increase in volume with waiting time, corresponding to intermolecular relaxation downhill in the energy landscape. The increase in cross peak 7 at $\omega_1 = 2011$ cm^{-1}, $\omega_3 = 2060$ cm^{-1}, however, shows IVR uphill in energy. These types of IVR are rarely seen in electronic exciton systems, as the energy barrier to uphill "relaxation" is many times the available k_BT energy.[30] The vibrational excitons in $Ru_3(CO)_{12}$ are 30 cm^{-1} apart, corresponding to an energy available even at less than 50 K. Only the cross peaks between the 2011 and 2060 cm^{-1} show IVR, which

indicates how well separated the axial only vibrational mode is relative to the other, mixed modes. Only in the highly disordering case of methanol is any additional IVR seen, from $\omega_1 = 2031$ cm^{-1} to $\omega_3 = 2060$ cm^{-1}. Lastly, the uphill IVR either disapears entirely or occurs too fast for our measurements to detect as greater disorder is introduced. Peak volume does not show an increase in ethanol or methanol for peak 3. This is more likely due to a rate too fast to be properly fitted, as already volume increases in other, less disordered solvents were occurring within hundreds of femtoseconds.

The bands at 2011 and 2060 cm^{-1} are also composed of degenerate modes, in contrast to the band at 2031 cm^{-1}. Additionally, the modes of these bands are composed of more highly delocalized vibrations, indicated by their IPR values. Mode 8 is effectively isolated to the 6 axial CO groups, making it less accessible to energy redistribution by symmetry and overlap. This is consistent with the picture of IVR between the high and low frequency bands, as they're composed of groups with more wavefunction overlap. Spectral diffusion, on the other hand, depends on solvent interactions. Here, the low frequency band composed of modes 6 and 7 presents a significantly slower rate. This suggests a slower picture of solvent interaction. Additionally, modes 6, 7, 10, and 11 collectively are composed of every CO group available while 8 is more isolated, indicating that the spectral diffusion solvation effects are not a function of distribution around the molecule; solvation must be similar enough to result in similar rates for the very different modes.

The experimental spectral diffusion rates are difficult to interpret as a function of solvent. More interesting, however, is the distinct difference between the three bands. While the middle and high frequency bands show a relatively fast spectral diffusion rate, around 5 ps for peak 9 and around 10 ps for peak 5, the low frequency band of peak 1 ranges from 20 to 25 ps with a trend towards longer spectral diffusion time. The separation between the spectral diffusion of the low frequency mode and the two higher frequency modes is very prominent. While the modes are separated by 30 cm^{-1} each from low to middle to high frequency, the separation of timescales between them is not at all monotonic. In n-hexane and cyclohexane in particular illustrate a vast disparity. In cyclohexane the spectral diffusion times from low to high frequency are 100, 5.7, and

10.4 ps respectively, and in n-hexane the times are 28, 6.4, and 12.0 ps respectively. Here, the central frequency band shows the fastest spectral diffusion rate, at odds with the previously stated energy interpretation, while the low frequency band is substantially slower relative to the gap between the other two frequencies. The ordering for the alcohols is more consistent, with decreasing times from low to high frequency.

In contrast to previously studied dimanganese decacarbonyl, we also observe spectral diffusion even in the less interactive solvents n-hexane and cyclohexane. Spectral diffusion reflects sampling of different microscopic solvents, yet n-hexane and cyclohexane do not contain sufficient long-term ordering to present multiple solvation environments. The frequency fluctuations cannot stem from the solvent environment because there is only one homogeneous environment. Instead, however, the frequency fluctuations can arise from fluctuations in the molecular structure of $Ru_3(CO)_{12}$. If the molecular structure is sufficiently loose as to allow multiple conformations to be sampled, the result would be a time dependent frequency correlation much like in spectral diffusion.

In fact, previous work contains some evidence that the equilibrium structure of $Ru_3(CO)_{12}$ is not well constrained. DFT calculations by Schaefer et al. show that at least two similar structures are almost identical in energy.[31] Additional calculations by Forni et al. provide evidence of stabilization of the strained fully-symmetric structure by what can only be described as "carbon-bonds" between the axial carbonyls, similar to the more common hydrogen-bond.[32] Together these effects indicate a flatness of the energy landscape near the equilibrium structures, possibly sufficient to produce multiple stable structures.

5.5: Conclusion

We have shown 2DIR to be a powerful method of extraction for both intramolecular and inframolecular dynamics on an ultrafast timescale. Using the rephasing and non-rephasing spectra, without computing the fully absorptive spectrum, spectral diffusion dynamics were isolated by the inhomogeneity index representative of the path imbalance

between the two spectra. IVR rates were extracted from the non-rephasing spectra directly, where cross-peaks do not oscillate, providing a clear picture of peak growth with waiting time.

Using the frequencies and amplitudes of vibrational transitions, as well as DFT calculated vibrational motions, a consistent Hamiltonian was generated that did not vary over multiple generations. As compared to electronic systems, this Hamiltonian is likely more representative of the $Ru_3(CO)_{12}$ system. An excitonic model was then applied using diagonal disorder to model disorder induced dynamics. Participation was calculated to compare molecular motions to their energetic timescales. Increases in participation ratio were seen for two modes, each one of a pair of degenerate modes containing a frustrated carbonyl. This indicates disorder could be inducing a higher participation of carbonyl groups in vibrational motion, allowing energy to be more efficiently transferred and equilibrated between modes and to the solvent.

In contrast to previously studied systems, in $Ru_3(CO)_{12}$ spectral diffusion occurs faster in hydrogen bonded environments and IVR occurs very rapidly. The fast memory loss and energy transfer likely occur due to the unique constraints of $Ru_3(CO)_{12}$: a three-membered ring produces vibrations in which specific carbonyl groups are “frozen” in an isolated environment, while disorder breaks the symmetry sufficiently to free these groups and allow motion. This also mixes the ordinarily isolated vibrational modes, allowing for faster energy transport as the mode wavefunction overlap is non-zero. We also observe spectral diffusion in weakly interacting solvents n-hexane and cyclohexane, indicative of a less rigid equilibrium structure in solution. This causes frequency fluctuations that present in a manner similar to spectral diffusion fluctuations.

References

1. Zewail, A. Femtochemistry: Atomic-scale dynamics of the chemical bond. *JOURNAL OF PHYSICAL CHEMISTRY A* **104**, 5660-5694 (2000).
2. Elsaesser, T. Two-Dimensional Infrared Spectroscopy of Intermolecular Hydrogen Bonds in the Condensed Phase. *Accounts of Chemical Research* **42**, 1220-1228 (2009).
3. Bakker, H.J., Rezus, Y.L.A. & Timmer, R.L.A. Molecular reorientation of liquid water studied with femtosecond midinfrared spectroscopy. *J. Phys. Chem. A* **112**, 11523 - 11534-11523 - 11534 (2008).
4. DeFlores, L.P. & Tokmakoff, A. Water penetration into protein secondary structure revealed by hydrogen-deuterium exchange two-dimensional infrared spectroscopy. *J Am Chem Soc* **128**, 16520-1 (2006).
5. Heyne, K. et al. Coherent low-frequency motions of hydrogen bonded acetic acid dimers in the liquid phase. *J. Chem. Phys.* **121**, 902-902 (2004).
6. Kwak, K., Zheng, J.R., Cang, H. & Fayer, M.D. Ultrafast two-dimensional infrared vibrational echo chemical exchange experiments and theory. *Journal of Physical Chemistry B* **110**, 19998-20013 (2006).
7. Jansen, T.L. & Knoester, J. A transferable electrostatic map for solvation effects on amide I vibrations and its application to linear and two-dimensional spectroscopy. *Journal of Chemical Physics* **124**, 11 (2006).
8. Milota, F., Sperling, J., Nemeth, A., Mančal, T. & Kauffmann, H.F. Two-Dimensional Electronic Spectroscopy of Molecular Excitons. *Accounts of Chemical Research* **42**, 1364-1374 (2009).
9. King, J.T., Baiz, C.R. & Kubarych, K.J. Solvent-Dependent Spectral Diffusion in a Hydrogen Bonded "Vibrational Aggregate". *The Journal of Physical Chemistry A* **114**, 10590-10604 (2010).
10. Cadierno, V. et al. Ruthenium-catalyzed redox isomerization/transfer hydrogenation in organic and aqueous media: A one-pot tandem process for the reduction of allylic alcohols. *GREEN CHEMISTRY* **11**, 1992-2000 (2009).
11. Glascoe, E., Kling, M., Shanoski, J. & Harris, C. Nature and role of bridged carbonyl intermediates in the ultrafast photoinduced rearrangement of Ru-3(CO)(12). *ORGANOMETALLICS* **25**, 775-784 (2006).
12. Kong, Q. et al. Ultrafast X-ray solution scattering reveals an unknown reaction intermediate in the photolysis of [Ru-3(CO)(12)]. *ANGEWANDTE CHEMIE-INTERNATIONAL EDITION* **47**, 5550-5553 (2008).
13. Kong, Q. et al. Ultrafast X-ray Solution Scattering Reveals Different Reaction Pathways in the Photolysis of Triruthenium Dodecacarbonyl (Ru-3(CO)(12)) after Ultraviolet and Visible Excitation. *JOURNAL OF THE AMERICAN CHEMICAL SOCIETY* **132**, 2600-2607 (2010).
14. Keske, J., McWhorter, D. & Pate, B. Molecular rotation in the presence of intramolecular vibrational energy redistribution. *INTERNATIONAL REVIEWS IN PHYSICAL CHEMISTRY* **19**, 363-407 (2000).
15. Zhang, C., Donadio, D. & Galli, G. First-Principle Analysis of the IR Stretching Band of Liquid Water. *JOURNAL OF PHYSICAL CHEMISTRY LETTERS* **1**, 1398-1402 (2010).
16. Khalil, M. & Tokmakoff, A. Signatures of vibrational interactions in coherent two-dimensional infrared spectroscopy. *Chemical Physics* **266**, 213-230 (2001).
17. Mukamel, S. *Principles of nonlinear optical spectroscopy*. (Oxford University Press: New York, 1995).
18. Bakker, H.J. Vibrational relaxation in the condensed phase. *J. Chem. Phys.* **121**, 10088 - 10095-10088 - 10095 (2004).

19. Adelman, S.A. & Stote, R.H. Theory of Vibrational-Energy Relaxation in Liquids - Construction of the Generalized Langevin Equation for Solute Vibrational Dynamics in Monatomic Solvents. *Journal of Chemical Physics* **88**, 4397-4414 (1988).
20. Shi, Q. & Geva, E. Semiclassical theory of vibrational energy relaxation in the condensed phase. *JOURNAL OF PHYSICAL CHEMISTRY A* **107**, 9059-9069 (2003).
21. Woutersen, S. & Bakker, H.J. Resonant intermolecular transfer of vibrational energy in liquid water. *NATURE* **402**, 507-509 (1999).
22. Read, E.L. et al. Visualization of Excitonic Structure in the Fenna-Matthews-Olson Photosynthetic Complex by Polarization-Dependent Two-Dimensional Electronic Spectroscopy. *Biophysical Journal* **95**, 847-856 (2008).
23. Engel, G.S. et al. Evidence for wavelike energy transfer through quantum coherence in photosynthetic systems. *Nature* **446**, 782-786 (2007).
24. Nee, M.J., McCanne, R., Kubarych, K.J. & Joffre, M. Two-dimensional infrared spectroscopy detected by chirped pulse upconversion. *Optics Letters* **32**, 713-5 (2007).
25. Ginsberg, N.S., Cheng, Y.C. & Fleming, G.R. Two-Dimensional Electronic Spectroscopy of Molecular Aggregates. *Accounts of Chemical Research* **42**, 1352-1363 (2009).
26. Myers, J.A. et al. Two-Dimensional Electronic Spectroscopy of the D1-D2-cyt b559 Photosystem II Reaction Center Complex. *The Journal of Physical Chemistry Letters* **1**, 2774-2780 (2010).
27. Khalil, M., Demirdoven, N. & Tokmakoff, A. Vibrational coherence transfer characterized with Fourier-transform 2D IR spectroscopy. *Journal of Chemical Physics* **121**, 362-73 (2004).
28. Nee, M., Baiz, C., Anna, J., McCanne, R. & Kubarych, K. Multilevel vibrational coherence transfer and wavepacket dynamics probed with multidimensional IR spectroscopy. *JOURNAL OF CHEMICAL PHYSICS* **129**, (2008).
29. Golonzka, O., Khalil, M., Demirdöven, N. & Tokmakoff, A. Coupling and orientation between anharmonic vibrations characterized with two-dimensional infrared vibrational echo spectroscopy. *J. Chem. Phys.* **115**, 10814 (2001).
30. Rini, M., Kummrow, A., Dreyer, J., Nibbering, E.T.J. & Elsaesser, T. Femtosecond mid-infrared spectroscopy of condensed phase hydrogen-bonded systems as a probe of structural dynamics. *Faraday Discussions* **122**, 27-40 (2003).
31. Peng, B., Li, Q., Xie, Y., King, R.B. & Schaefer III, H.F. Unsaturated trinuclear ruthenium carbonyls: large structural differences between analogous carbonyl derivatives of the first, second, and third row transition metals. *Dalton Trans.* 6977 (2008).doi:10.1039/b810710f
32. Gervasio, G., Marabello, D., Bianchi, R. & Forni, A. Detection of Weak Intramolecular Interactions in Ru3(CO)12 by Topological Analysis of Charge Density Distributions. *The Journal of Physical Chemistry A* **114**, 9368-9373 (2010).

Chapter 6

Conclusions

6.1: Experimental transient 2DIR

We have shown that transient 2DIR provides valuable information on the product of a photoreaction.[1-5] This extends the benefits of the frequency frequency correlation function to a non-equilibrium system. Analyzing as a function of both waiting time and pump-probe delay allows the study of the evolution of a non-equilibrium correlation function.

Unfortunately, however, transient 2DIR presents a difficult experiment to perform and analyze. There are many experimental difficulties in obtaining the data, including alignment of a complicated optical system spanning the generation of two frequency regimes. The generated visible and infrared must then also be recombined. The sample cannot be static, but must be refreshed, which introduces additional noise. Particularly, difference signals can be difficult to isolate, as with the gravity driven jet, or must be kept relatively small, as with the windowed flowing cell. In both cases, the signal to noise of the difference is significantly lower than the equilibrium 2DIR spectra acquired. This is further hampered by vibrational scrambling in the triggered exchange 2DIR experiment, making the TE-2DIR signals weak and difficult to isolate. Even in PP-2DIR, however, the difference signal amplitudes are two orders of magnitude lower than their component equilibrium spectra. Combined with a 100 cm^{-1} frequency window spanned by a gaussian infrared pulse, the edge transient peaks become noisy and difficult to resolve.

Once the transient signal has been acquired, analysis presents additional challenges. Overlap of bleach and transient spectral features is not only still present in

transient 2D experiments, but is complicated by the addition of overlapped cross peaks. Though the transient can be extricated by careful fitting procedures, this represents substantial additional work in two dimensions. It is thus beneficial to seek systems where the photoproduct has transient behavior that is partially isolated form the parent. Though this is of course true is one dimensional pump-probe experiments, the two dimensional experiments still provide the advantage of correlations mentioned previously.

A second challenge arises in the analysis of transient signals in the form of additional peaks. Excess energy deposited in the molecule by the photoexcitation can result in a vibrationally excited photoproduct. Additional peaks along the diagonal of a 2D spectrum are then seen corresponding to the of each anharmonic transition in each manifold within the bandwidth of the experiment. Cross peaks then appear due to not the shared ground state, but the shared vibrational ladder starting state. For example, cross peaks appear between the $\upsilon_{a\rightarrow 2a}$ and the $\upsilon_{a\rightarrow 0}$ transitions due to starting in the vibrationally excited |a> state. Though this in principle provides additional information, it also presents additional complications in analysis. In many cases, the coupling represents only coupling through the initial state, making the information content of these additional peaks relatively low.

6.2: *Transient $W(CO)_6$ and additional information content*

Transient 2DIR presents additional peaks requiring assignment. Using the transient 2DIR spectrum of an early waiting time and early pump-probe delay time, the transient peaks of $W(CO)_6$ can be assigned to vibrational transitions as in previous 1D pump-probe spectroscopy using the experimental and calculated energy levels of $W(CO)_5$. We have assigned both the diagonal and off-diagonal peaks to transitions arising from both a vibrational ground state photoproduct as well as a vibrationally excited photoproduct. Cross peaks appear between these where two frequencies are coupled by the shared starting state. This is similar to equilibrium spectroscopy, where two frequencies can couple through the common ground state to produce a cross peak.

At least two additional peaks appear in the transient 2DIR spectra of $W(CO)_5$,

however, that do not correspond to coupling through a shared initial state. Cross peaks between the $\upsilon_{b\rightarrow 2b}$ and the $\upsilon_{a\rightarrow 0}$ transitions appear at early waiting times and pump-probe delays. These peaks require intermolecular vibrational energy redistribution during the waiting time, indicating a population transfer from |b> to |a>. This IVR then slows with increased pump-probe delay, which was attributed to decreasing temperature. Calculating the density of states of the bath phonon modes predicts a sevenfold decrease in rate from 2000 °C to room temperature, corresponding to a decrease in IVR rate from 100-200 ps to 1-2 ps, consistent with previous metal carbonyls.

Using the evolution of the peak volumes as a function of waiting time and pump-probe delay, we found that the relaxation of the reorientational rate occurs in at most 60 ps, and is likely faster. Though in the previously studied $Mn_2(CO)_{10}$ system the reorientational rate relaxation did not occur on the same timescale as indicated by peak width narrowing in the 1D spectroscopy, here the 1D cooling and 2D cooling measurements agree very well. This may be a function of the reduced degrees of freedom of the system, or of the single monomer product of $W(CO)_6$ in comparison to the two monomer product of $Mn_2(CO)_{10}$.

Additionally, ladder climbing seems to be unavoidable in $W(CO)_6$. Even at significantly reduced IR excitation powers additional peaks appear corresponding to excitation of multiple anharmonic transition of the parent. This again may be a function of the low number of degrees of freedom in $W(CO)_6$, which, combined with a weakly coupled solvent, may help trap the vibrational energy in the degenerate IR active modes.

6.3: Equilibrium $Ru_3(CO)_{12}$ and disorder-induced delocalization

In general, addition of disorder causes vibrational localization as a single local mode interacts with the disordering element.[6] This causes reduced coupling between the distorted mode and the remaining coupled local modes. Effectively, this (partially) localizes a vibrational mode as the energies no longer couple efficiently, while leaving the remaining modes to be delocalized over one fewer local oscillator. In both ways the disorder induces localization.

$Ru_3(CO)_{12}$, however, is both highly symmetric and composed of an odd-membered ring. Together these cause vibrational delocalization that is highly constrained. In particular, parity dictates that an IR active mode, delocalized over an odd number of elements, must constrain one member to be motionless. This is exactly what we observe in calculations of the vibrational carbonyl stretching modes of $Ru_3(CO)_{12}$. Two of the carbonyl IR bands that appears are due to degenerate vibrational modes. These modes are composed of largely delocalized carbonyl stretching but contain at least two carbonyls, an axial and an equatorial, whose motions are frustrated by the parity of the odd-membered ring.

Using a simplified model and a calculated Hamiltonian, we find that when solvent disorder is introduced an increase in participation ratio is seen.[5] Moreover, the participation ratio of the degenerate modes that contain frustrated carbonyl groups split, with one mode increasing while the other decreases. The corresponds well with a picture in which the induced disorder of the solvent causes localization of the vibration of one carbonyl member, which in turn frees others from the symmetry condition that frustrated them, allowing them to participate in delocalization. The induced disorder actually breaks the symmetry constraint frustrating carbonyl motion, allowing a greater participation in carbonyl delocalization.

Experimentally, 2DIR spectra of $Ru_3(CO)_{12}$ show both very fast IVR and spectral diffusion in a range of solvent environments. Fast IVR could be due to a high degree of coupling between the vibrational modes, particularly in the case where two of the IR active modes have non-perpendicular transition moments. Alternatively, in the previously studied $Mn_2(CO)_{10}$ we saw no spectral diffusion in weakly interacting solvents such as n-hexane and cyclohexane, while in $Ru_3(CO)_{12}$ spectral diffusion occurs to the same degree in the weakly and strongly interacting solvents. Spectral diffusion indicates the sampling of discrete microscopic environments by the sample. In the case of a rigid molecule, this corresponds to sampling discrete solvation environments. In n-hexane and cyclohexane, lack of a hydrogen bonding structure makes the solvent relatively homogeneous. Thus, spectral diffusion in $Ru_3(CO)_{12}$ likely corresponds not to a sampling of solvation environments, but of solute conformations. Spectral diffusion in $Ru_3(CO)_{12}$

is an indication of a lack of rigidity. This is supported by structural calculations of $Ru_3(CO)_{12}$ which indicate several structures of similar energies at the bottom of the potential well.[7] This may be in part due to an unusual "carbon bond" as shown by additional calculations, where the fully symmetric structure is stabilized by partial overlap of the axial carbon wavefunctions.[8]

6.4: Outlook

The metal carbonyl family represents a large group of compounds used in donating CO and promoting reaction catalysis.[9-11] Most catalysis also occurs via a carbonyl removal and rejoining. Such catalysts are being studied to obtain better synthesis pathways for plastic and energy storage compounds. Understanding the carbonyl removal processes may play an important role in carbon-hydrogen and carbon-carbon bond activation, which in turn is an important step in energy generation and storage pathways.

Ideally, understanding the solvation of the non-equilibrium species during and following formation is the key to this process. In order to elucidate the dynamics of this process, however, we must first also understand the equilibrium dynamics. Using the transient techniques previously discussed in Chapter 4 together with the equilibrium 2DIR advantages as shown in Chapter 5 we believe it will be possible to study the non-equilibrium photodissociation process with clarity. In particular, $Ru_3(CO)_{12}$ has been shown to undergo photodissociation similar to the reactions discussed.[12-14] It is currently under some contention, however, as to the number and stability of photoproducts. Studies predict either two or three photoproducts, each with unique structures, and possibly unique dynamics. Initial transient spectra of the photoreaction show a profusion of peaks in the carbonyl stretching region, making analysis almost impossible. Applying the equilibrium analysis as laid out in Chapter 4 with the non-equilibrium techniques of Chapter 5 would allow the non-equilibrium photoproducts to be studied and separated.

Though we have not yet reached the point of being able to isolate and identify the component peaks of such a complex system, we have certainly taken some of the first

steps. Current work on an ultrabroadband IR source to be used as a probe will help in accessing additional spectral regions and features, providing further data with which to

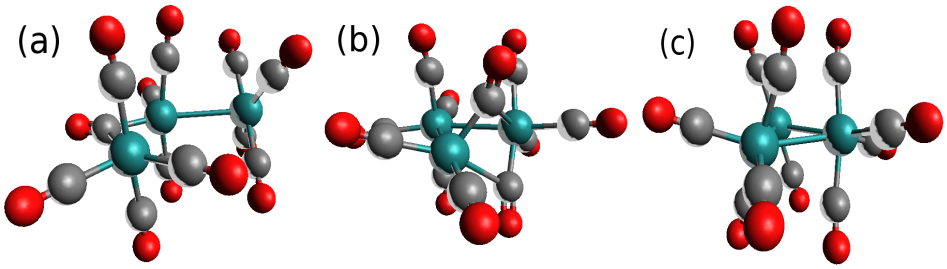

Figure 53: Reported products following photodissociation of $Ru_3(CO)_{12}$. Products (a) and (b) were reported from monitoring the bridging carbonyl region of the IR spectrum. Product (c) has a calculated radial distribution function that was found to match the remainder of a composite radial distribution function found by x-ray experiments. These products differ significantly, with (a) having a cleaved metal-metal bond and a bridging carbonyl but containing all 12 original carbonyl groups, (b) containing two bridging carbonyls and having only 11 carbonyls, and (c) containing no bridging carbonyls and having only 10 carbonyls. Which pathway bears relation to the catalytic process could have a distinct impact in understanding metal carbonyl catalysis, as well as the differences between equilibrium activation and photoactivation.

assign spectral evolution to molecular evolution. New and faster modeling techniques have made comparison of experiment and theory easier and more accessible to all researchers. Though a complete picture of solvation, especially in non-equilibrium systems, may well require ultrafast x-ray experiments to resolve full atomic motion, 2DIR provides an excellent ultrafast, atomically-sensitive current step towards that end. Extending 2DIR to transient systems extends all the benefits of ultrafast frequency correlation, allowing reactions to be watched in almost real time.

References

1. Baiz, C.R., McCanne, R. & Kubarych, K.J. Structurally selective geminate rebinding dynamics of solvent-caged radicals studied with nonequilibrium infrared echo spectroscopy. *J Am Chem Soc* **131**, 13590-1 (2009).
2. Baiz, C.R. & Kubarych, K.J. Ultrafast Vibrational Stark-Effect Spectroscopy: Exploring Charge-Transfer Reactions by Directly Monitoring the Solvation Shell Response. *Journal of the American Chemical Society* **132**, 12784-12785 (2010).
3. Baiz, C.R., Nee, M.J., McCanne, R. & Kubarych, K.J. Ultrafast nonequilibrium Fourier-transform two-dimensional infrared spectroscopy. *Opt. Lett.* **33**, 2533-2535 (2008).
4. Baiz, C.R., McCanne, R., Nee, M.J. & Kubarych, K.J. Orientational Dynamics of Transient Molecules Measured by Nonequilibrium Two-Dimensional Infrared Spectroscopy. *The Journal of Physical Chemistry A* **113**, 8907-8916 (2009).
5. McCanne, R., King, J.T., Baiz, C.R. & Kubarych, K.J. Vibrational Energy Transfer and Spectral Diffusion Dynamics in a Vibrational Aggregate with Disorder-Induced Delocalization. *Forthcoming* (2011).
6. King, J.T., Baiz, C.R. & Kubarych, K.J. Solvent-Dependent Spectral Diffusion in a Hydrogen Bonded "Vibrational Aggregate". *The Journal of Physical Chemistry A* **114**, 10590-10604 (2010).
7. Peng, B., Li, Q., Xie, Y., King, R.B. & Schaefer III, H.F. Unsaturated trinuclear ruthenium carbonyls: large structural differences between analogous carbonyl derivatives of the first, second, and third row transition metals. *Dalton Trans.* 6977 (2008).doi:10.1039/b810710f
8. Gervasio, G., Marabello, D., Bianchi, R. & Forni, A. Detection of Weak Intramolecular Interactions in Ru3(CO)12 by Topological Analysis of Charge Density Distributions. *The Journal of Physical Chemistry A* **114**, 9368-9373 (2010).
9. Hebrard, F. & Kalck, P. Cobalt-Catalyzed Hydroformylation of Alkenes: Generation and Recycling of the Carbonyl Species, and Catalytic Cycle. *CHEMICAL REVIEWS* **109**, 4272-4282 (2009).
10. Ito, K., Hara, Y., Mori, S., Kusama, H. & Iwasawa, N. Theoretical Study of the Cycloaddition Reaction of a Tungsten-Containing Carbonyl Ylide. *CHEMISTRY-A EUROPEAN JOURNAL* **15**, 12408-12416 (2009).
11. Cadierno, V. et al. Ruthenium-catalyzed redox isomerization/transfer hydrogenation in organic and aqueous media: A one-pot tandem process for the reduction of allylic alcohols. *GREEN CHEMISTRY* **11**, 1992-2000 (2009).
12. Glascoe, E., Kling, M., Shanoski, J. & Harris, C. Nature and role of bridged carbonyl intermediates in the ultrafast photoinduced rearrangement of Ru-3(CO)(12). *ORGANOMETALLICS* **25**, 775-784 (2006).
13. Kong, Q. et al. Ultrafast X-ray solution scattering reveals an unknown reaction intermediate in the photolysis of [Ru-3(CO)(12)]. *ANGEWANDTE CHEMIE-INTERNATIONAL EDITION* **47**, 5550-5553 (2008).
14. Kong, Q. et al. Ultrafast X-ray Solution Scattering Reveals Different Reaction Pathways in the Photolysis of Triruthenium Dodecacarbonyl (Ru-3(CO)(12)) after Ultraviolet and Visible Excitation. *JOURNAL OF THE AMERICAN CHEMICAL SOCIETY* **132**, 2600-2607 (2010).